UNIVERSITY OF CALIFORNIA SAN DIEGO

Ringing Tones of Stones, Bones, and Coastal Zones

A dissertation submitted in partial satisfaction of the
requirements for the degree Doctor of Philosophy

in

Earth Sciences

by

Margaret Morris

Committee in charge:

Professor John Hildebrand, Co-Chair
Professor Petr Krysl, Co-Chair
Professor Isabel Rivera-Collazo, Co-Chair
Professor Falko Keuster
Professor Ross Parnell-Turner

2023

The Dissertation of Margaret Morris is approved, and it is acceptable in quality and form for publication on microfilm and electronically.

University of California San Diego

2023

DEDICATION

I dedicate this to my future cat and all the cool cats I've had the pleasure to know and love.

EPIGRAPH

This here's a re-search laboratory. Re-search means look again, don't it? Means they're looking for something they found once and it got away somehow, and now they got to re-search for it? How come they got to build a building like this, with mayonnaise elevators and all, and fill it with all these crazy people? What is it they're trying to find again? Who lost what?

Kurt Vonnegut

TABLE OF CONTENTS

LIST OF FIGURES

LIST OF TABLES

LIST OF SUPPLEMENTARY FILES

Morris_CH2-TPC-Animations-Modes-1-3-9-11.zip

PREFACE

We know that the ocean needs protection, so we have laws regulating this protection. To ensure protection of ocean resources, it is tempting to think that we must either (a) make laws so broad as to ensure that there is no possibility of humans inflicting further damage or (b) give up on regulation, believing that anything truly enforceable will be ineffective to the point that we may damage our economy for nothing. What we need is to make laws and their implementation both efficient and effective. By understanding the nuances of specific issues, like how whales react to sound and how cultural materials may be preserved, we can begin to tune our preservation practices for maximum result with minimal effort. In this way we can support the goals of those who wish to use the oceans' contents and those who wish to protect them.

The ocean's a dwelling we need to conserve
for whales and for people who do not deserve
the climate destruction we soon may observe
The ocean holds memories we long to preserve

ACKNOWLEDGEMENTS

I would like to acknowledge Professors Isabel Rivera-Collazo, John Hildebrand, and Petr Krysl as the chairs of my committee.

I would like to acknowledge the Human Ecology lab, the Whale Acoustics lab, and my friends in the Institute of Geophysics and Planetary Physics.

Chapter 1, in full, is a reprint of the material as it appears in The resonant acoustic signatures of lithic debitage 2022. Morris, Margaret; Krysl, Petr; Hildebrand, John; Rivera-Collazo, Isabel, Journal of Archaeological Science: Reports 2022. The dissertation author was the primary investigator and author of this paper.

Chapter 2, in full, has been submitted for publication of the material as it may appear in Resonance of the tympanoperiotic complex of fin whales with implications for their low frequency hearing 2023. Morris, Margaret; Krysl, Petr; Hildebrand, John; Cranford, Ted, PLOS ONE, 2023. The dissertation author was the primary investigator and author of this paper.

Chapter 3, in part is currently being prepared for submission for publication of the material. Morris, Margaret; Rivera-Collazo, Isabel; Hildebrand, John. The dissertation author was the primary investigator and author of this material.

VITA

2017 Bachelor of Science, Brandeis University

2023 Doctor of Philosophy, University of California San Diego

PUBLICATIONS

"The Resonant Acoustic Signatures of Lithic Debitage" Journal of Archaeological Sciences: Reports, vol. 41, February 2022

FIELDS OF STUDY

Major Field: Oceanography (Acoustics)

Studies in Archaeology
Professors John Hildebrand and Isabel Rivera-Collazo

Studies in Acoustics
Professors John Hildebrand and Petr Krysl

ABSTRACT OF THE DISSERTATION

Ringing Tones of Stones, Bones, and Coastal Zones

by

Margaret Morris

Doctor of Philosophy in Earth Sciences

University of California San Diego, 2023

Professor John Hildebrand, Co-Chair
Professor Petr Krysl, Co-Chair
Professor Isabel Rivera-Collazo, Co-Chair

Archaeological sites related to the first humans on North America's Pacific Coast may be preserved offshore, but finding those sites remains a challenge. Rising sea levels threaten to destroy near-shore sites, adding urgency to the question of how to find and preserve vulnerable cultural heritage resources. Current best-practices include reconstructing drowned landscapes as they were during possible human occupation. In chapter 3, we investigate the submerged San Dieguito river valley. Humans were nearby, on the Northern Channel Islands, by the time of the Younger Dryas, a thousand-year period of stable sea level and relatively cool temperatures. We use sub-bottom sonar and sediment cores to map the offshore extent of the river valley, and to

gain insight into the local landscape during the Younger Dryas period. While our interpretations can be used to make predictions about human landscape use, it would be better to locate verifiable archaeological material. Chapter 1 lays some needed foundation for developing a reliable method to detect lithic (stone) artifacts during sub-bottom sonar surveys using their resonance properties. This method could augment surveys, like that of chapter 3, to include potential artifact deposits in the mapped landscapes. As we make efforts to use sound to preserve human heritage, we acknowledge that marine mammals have been using sound in the ocean for much longer. The noise humans add to the underwater soundscape could interfere with their daily activities. In chapter 2, we study the hearing mechanisms of whales, and use methods adapted from those in chapter 1 to measure the resonance properties of fin whale ear bones. Understanding how marine mammals hear can help us mitigate negative impacts from our methods, and learning how they use sound could even help us design more effective sonar instruments. In the three chapters combined, we study the ringing tones of stones, bones, and coastal zones to tune the protection of marine mammals and cultural heritage.

Introduction

For decades, humans have been using the properties of underwater sound to explore the ocean. We send out sounds and listen for the landscape to ring it back to us, revealing the seafloor's structure. I continue this practice in a coastal zone, using multibeam and sub-bottom sonar to map an underwater portion of the San Dieguito river valley to investigate the potential attractiveness of the San Dieguito River landscape when humans may have encountered the area and to determine whether archaeological materials could have survived inundation. The onshore portion of the river valley exists today as a lagoon that has been drastically altered by human development, but 40 years ago existed as an expansive wetland and salt marsh [Beller et al., 2014]. The shore has been at its present location for about 5000 years, but it was further seaward for millennia before [Lambeck et al., 2014, Reynolds and Simms, 2015]. Sea level was over 120m lower during the last glacial maximum, which places the San Diego area's coast out to the edge of the continental shelf about 20,000 years ago. As sea level rose, the coastline moved landward, and the landscape changed [Reeder et al., 2011, Reeder-Myers et al., 2015]. Much of the coast was eroded by strong waves as higher seas rolled in, but some remnants from the former landscape remain preserved beneath sediment cover [Flemming et al., 2017]. Some remnants of particular interest include ancient shorelines, channels, and sediments [McLaren et al., 2020].

Ancient shorelines may be preserved under certain conditions. If the sea level is stable for long enough, and wave energy is high enough, the waves may erode the land creating a cliff. This eroded feature may be visible in sub-bottom sonar as a notch in the subsurface, and is often filled in with later sediment deposited after sea level rose again [Laws et al., 2020]. Preservation of these notches, paleoshoreline angles, depends on a number of conditions including duration of

the sea level standstill, wave energy during inundation, and erodibility of the land. While sea level has risen almost continuously since the last glacial maximum, there have been a few occasions where the rate of sea level rise slowed, the most significant of which is known as the Younger Dryas period [Cheng et al., 2020, Lambeck et al., 2014, Fairbanks, 1989]. During the Younger Dryas, about 12,000 years ago, sea level was relatively stable for over 1,000 years, enough time for the waves to significantly erode the coastline. Global sea level during the Younger Dryas period was around 60m lower than at present. As we explore offshore the San Dieguito lagoon, we identify the paleoshoreline angle from the Younger Dryas in multiple sub-bottom profiles and trace the former shoreline parallel to the present coast.

This Younger Dryas is more than a period of stable sea level. During this period, the earth's warming trend temporarily reversed, plunging the global climate back into near-glacial temperatures [Cheng et al., 2020]. Mass extinctions occurred over North America around the same time. North America also saw the relatively new presence of humans. Human presence was established on the Channel Islands by 13,000 years ago, placing humans in southern California during the Younger Dryas [Erlandson et al., 1996, Erlandson et al., 2011]. Because the Younger Dryas shoreline is identifiable, and humans were nearby during that time, our primary goal in mapping the offshore extension of the San Dieguito river valley is to reconstruct the paleolandscape from the Younger Dryas period.

Sediment preservation potential is relatively high near rivers, wetlands, and low-energy or high-sedimentation environments. We look at the underwater portion of the San Dieguito river valley for clues that reveal the nature of its ancient existence. We 'look' first by listening to this coastal zone ring. Using sub-bottom profiling sonar, we record cross-sections of the valley that show sound-reflecting layers beneath the seafloor. From these profiles, we can map the extent of the river valley and can trace deeper paleochannels (ancient waterways) within the river valley [Hildebrand and York, 2022]. We can also observe layers of sediment, where the sediment properties change enough to reflect the sound waves from the sonar. To detect subtle changes in sediment layers with high resolution, we extract columns of sediment from

the seafloor as sediment cores. Using a vibracorer, we pulled out 4" diameter tubes of sediment, which we examined back in the lab.

Maps derived from sonar and sediment data can be used to predict where humans may have lived, to aid archaeological investigations into the earliest human presence in southern California [Reeder et al., 2011, McLaren et al., 2020]. This is the goal of chapter 3. While archaeological probability maps are useful, they are predictions, not reality. To test whether humans were indeed in the area, we must find direct evidence of humans. Chapter 1 supports a developing methodology to detect human-made artifacts using the same sub-bottom sonar used to map the underwater landscape.

Acoustic methods to search for submerged archaeological sites have shown that concentrations of knapped flint produce a visible acoustic response in sub-bottom sonar profiles in a variety of geographical settings [Grøn et al., 2018a, Grøn et al., 2021]. Knapped flint and other stone is found all around in human sites, and is identifiably human-made. Field tests, experiments, and models indicate that this acoustic signal results from resonance of the flint or other stone tools (lithics) and knapping byproducts (lithic debitage) [Blake and Cross, 2008, Grøn et al., 2018b, Grøn et al., 2021, Hermand et al., 2011, Hermand and Tayong, 2013]. By lithic resonance, I mean that the stone pieces vibrations are especially strong and easily excitable at specific frequencies. By understanding how the lithic tools and debitage vibrate, we can better understand the associated signals that appear in the sub-bottom profiling data, allowing us to use it to detect the human-made artifacts.

We model and measure the acoustic resonance of a variety of lithic shapes and materials. Struck lithics produce multiple resonant peaks under 30 kHz, and the quality of the resonance decreases with material coarseness, meaning that lithic debitage made of materials like flint will have a stronger signal than more granitic materials. We use a combination of finite element and boundary element methods to model the natural vibrations of lithic debitage in both air and water. We model the acoustic backscatter of individual lithics in water as a function of frequency and incidence angle. We find the strongest resonant signal between 8-16 kHz for a collection of lithic

debitage. Sub-bottom profilers tend to work in the 2-24kHz range, meaning they could detect lithics with a wide range of shapes and sizes.

Results indicate that the lithic resonance signal is highly directional, with target strength up to -20 dB when excited at optimal angles. For a flat-laying lithic, target strength at normal incidence is, on average, 10 dB lower than the strongest signal, typically found $55\circ \pm 18\circ$ from normal incidence. We suggest that the best way to detect submerged lithics may not be through standard sub-bottom profiling with a co-located source and receiver using direct downward pulse, but instead with a chirp pulse sent and received at an angle with respect to the sea bottom. This would allow us to excite and receive stronger resonance signals and to avoid large seafloor reflections that could obscure the lithic signal. However, changing the configuration of the sub-bottom profiler would make it less suitable for landscape mapping, as it is used in chapter 3.

Chapter 2 uses similar techniques to chapter 1, but deals with resonance of the ear bones of a fin whale. The ear bones are a more complicated structure than the lithics of chapter 1. We study the tympanoperiotic complex (TPC) bones (ear bones) of the fin whale skull using experimental measurements and finite element modeling to provide insight into the low frequency hearing of these animals. Knowledge of baleen whale low frequency hearing sensitivity is needed to assess the potential impact of anthropogenic noise on their anatomy and behavior [Southall et al., 2019]. This is increasingly important due to the presence of noise from shipping traffic, seismic exploration, and offshore development in whale habitat [Hildebrand, 2009]. Particularly helpful would be knowing the frequency sensitivity of hearing for a variety of different whale species. A modelling approach enables studies of the effect of exposure to specific frequencies without the extra noise and extraneous effects that may be present in experiments with live animals [Cranford and Krysl, 2015]. In chapter 3, we conduct measurements and modeling that give insight into how the TPC may play a role in low frequency hearing.

The study focused on measuring the sounds emitted by the left and right TPC bones when the bones were tapped at designated locations. Radiated sound was recorded by eight

microphones arranged around the tympanic bulla. A finite element model was also created to simulate the natural mode vibrations of the TPC and ossicular chain, using a 3D mesh generated from a CT scan. The simulations produced mode shapes and frequencies for various material properties. The recorded sound amplitudes were compared with the the simulated displacement, and we identified twelve resonance modes that appeared in both model and measurement. The first twelve modes of vibration of the TPC had resonance frequencies between 100Hz and 6kHz. Many vibrational modes focused energy at the sigmoidal process, and therefore the ossicular chain. The resonance frequencies of the left and right TPC were offset, suggesting a mechanism for the animals to have improved hearing at a range of frequencies as well as a mechanism for directionality in their perception of sounds. This gives us insights into how fin whales hear, and which frequencies they hear best.

All three chapters are broadly motivated by a desire to preserve what the ocean holds. The ocean holds information about the first humans to live in North America. Climate change is threatening to destroy archaeological sites and cultural heritage resources near shore. We aim to protect this cultural heritage by locating it and studying what we can while it remains preserved in situ. In chapter 3 we map a landscape, the San Dieguito river valley, that may have been attractive to humans and that has potential for preservation of archaeological materials. We work on a method to directly detect human-made artifacts in chapter 2. This method could be used in surveys like the one we conducted in chapter 3, to locate artifact deposits in the mapped landscapes. All of this surveying and ocean-studying with sound leads us and other humans to pump more noise into the ocean. To understand how this extra sound affects marine mammals, we must study the hearing mechanisms of the animals. By knowing how they hear, and which sounds they hear best, we can avoid confusing or disturbing them or worse, permanently damaging their hearing, and learning how they use sound could even help us use sound more effectively. So, in this dissertation, we study the ringing tones of stones, bones, and coastal zones to tune the protection of marine mammals and cultural heritage.

Chapter 1

The Resonant Acoustic Signatures of Lithic Debitage

Abstract

Acoustic methods to search for submerged archaeological sites have shown that concentrations of knapped flint produce a visible acoustic response in chirp sonar profiles in a variety of geographical settings. Field tests and simulations have suggested that the submerged lithic signal is due to acoustic resonances of the flaked stone. We model and measure the resonant acoustic signatures of chert, obsidian, metavolcanic, and granitic lithic debitage. Struck lithics produce multiple resonant peaks under 30 kHz, with high quality factors that decrease with material coarseness. We use a combination of the finite element and boundary element methods to model the natural vibrations of lithic debitage in both air and water. Direct measurement of lithic material density and adjustment of the Young's modulus and Poisson's ratio provide excellent correspondence between measured and modeled resonances. Using a coupled finite element and boundary integral method, we model the acoustic scattering return of individual lithics in water as a function of frequency and incidence angle. We find the strongest resonant signal between 8-16 kHz for a collection of lithic debitage. Results indicate that the lithic resonance signal is highly directional, with target strength up to -20 dB when excited at optimal angles. For a flat-laying lithic, target strength at normal incidence is, on average, 10 dB lower than the strongest signal, typically found $55^\circ \pm 18^\circ$ from normal incidence. We suggest that the best way

to detect submerged lithics may not be through standard mono-static sub-bottom profiling with a direct downward pulse, but with a chirp pulse sent and received at an angle with respect to the sea bottom.

1.1 Introduction

Coastal lands that were inundated since the last glacial maximum hold key information about human migration, trade, land use, and climate change adaptations [Bailey and King, 2011, Bailey and Flemming, 2008, Braje et al., 2019a, Erlandson, 2001]. Advances in paleolandscape reconstruction and modeled site prediction have demonstrated that archaeological information can be preserved in submerged sites [Benjamin, 2010, Watts et al., 2011, Westley et al., 2011, Flemming et al., 2017, McLaren et al., 2020]; however, relatively few submerged sites have been directly detected [Sturt et al., 2018]. Site detection is necessary to test site occurrence prediction models and generate new data in the form of cultural materials and associated landscape characteristics.

The predominant means of submerged site detection are through diver surveys and chance finds, with chance accounting for the majority of reported sites [Flemming, 2020]. Divers are only able to see what is visible on the seafloor, so entirely buried sites are missed. Chance finds are unreliable, and many occur through destructive means, such as dredging and trawling, which alter the underwater landscape and remove artifacts from their associated context. Other chance finds are costly and inconvenient, as offshore development projects can be delayed by an accidental site discovery. With international emphasis on developing a blue economy [Centre et al., 2020], in which marine resources are optimally exploited while still being preserved, it becomes increasingly important to develop reliable, non-destructive methods for site detection and study. While offshore developments plan and budget for mitigation needs, revealing archaeological material early in the planning process would add time to re-think project proposals to avoid large scale impact and reduce the need for costly mitigation. Further, the importance of underwater

cultural heritage is formally recognized in the UNESCO 2001 convention [UNESCO, 2001], which promotes *in situ* preservation of underwater sites. The goal is to avoid impact, rather than settle for mitigation after impact occurs. Effective remote-sensing methods would prevent costly delays to development projects in marine environments, decrease destruction of benthic habitats, and preserve underwater archaeological information *in situ*, satisfying multiple internationally recognized objectives.

A primary difficulty in detecting prehistoric sites is that objects left behind are often buried and too small to be readily detected by standard marine survey methods [Flemming et al., 2014, Plets et al., 2013, Astrup et al., 2019, McCarthy et al., 2019]. Ole Grøn and colleagues propose a sub-bottom acoustic profiling method to search specifically for knapped stone, which is a clear indicator of human presence and is widely ubiquitous in prehistoric archaeological sites [Grøn et al., 2018a, Grøn et al., 2021]. The proposed method has already facilitated submerged site discovery in varied geographical settings, with concentrations of knapped stone producing a visible acoustic response in minimally processed chirp sub-bottom profiles. They suggest that the method's success is due to the lithics' strong resonance properties, which have been demonstrated in both experiments [Blake and Cross, 2008, Grøn et al., 2018b, Grøn et al., 2021] and preliminary models [Hermand et al., 2011, Hermand and Tayong, 2013].

While this method has led to site discoveries, its potential is just beginning to be understood. The method recommends looking for a diffuse 'haystack' signal in the water column portion of sub-bottom profiles. Why the signal appears in the water column remains a mystery, since the lithics are located within the sediment. As it stands, the signal cannot be used to infer the depth and extent of buried lithics, nor any properties of the lithics themselves; however, the success of the method gives confidence that acoustic remote sensing can provide such information. To retrieve this data, it is necessary to (1) learn more about lithics' acoustic properties and (2) use more advanced data processing methods to detect and interpret the lithic signatures. This paper begins to address the first of these necessities, which is a prerequisite to the second.

We present the modelled and measured acoustic response of an assortment of lithic deb-

itage. The lithics' acoustic resonance frequencies are modelled in both air and water using a combined finite element and boundary element method and tested against measured data for object resonance in air. We characterize strength and directionality of the acoustic response of flat-laying lithics by simulating the acoustic return of individual lithics insonified by a plane wave using a coupled finite element and boundary integral method [Abawi, 2017, Abawi and Krysl, 2017]. We explore relationships between lithic properties (material and dimensional) and resonance frequencies using a thin-plate vibration approximation. By understanding what frequency range and signal strength to expect for different types of lithics, we can use expected lithic types to help guide sonar searches for sites. Directionality in the acoustic response is presented, and results are used to suggest modifications to currently proposed detection methods.

1.2 Materials & Methods

1.2.1 Lithic Assortment

Source and Material Properties

We analyzed 40 specimens of lithic debitage, comprised of 37 pieces knapped by G. Timothy Gross (pers. comm.), and 3 granitic artifacts from the archaeological site of Angostura in Barceloneta, Puerto Rico (obtained by I. C. Rivera-Collazo). Four lithic materials were chosen to represent a range of knapping material: glass - obsidian ($n = 9$), cryptocrystalline - pink chert ($n = 19$), fine-grained crystalline - Santiago Peak metavolcanic rock ($n = 9$), and coarser-grained crystalline - granitic rock ($n = 3$). The lithic materials were characterized in the model by their density, ρ, Young's modulus, E, and Poisson's ratio, ν. Density was measured by a water-displacement buoyancy method employing Archimedes' principle. Young's modulus and Poisson's ratio were chosen to match modeled resonant frequencies (sec. 1.2.3) with measured lithic spectrum peaks (sec. 1.2.2) for a subset of the examples for each material. Initial values of E_0, ν_0 chosen from literature (obsidian: $E_0 = 70$ GPa, $\nu_0 = 0.08$ [Klein and Carmichael, 2021], chert: $E_0 = 80$ GPa, $\nu_0 = 0.125$ [Aliyu et al., 2017], metavolcanic: $E_0 = 88$ GPa, $nu_0 = 0.2$

Table 1.1. Material properties used in the models.

Material Properties	Pink Chert	Santiago Peak Metavol-canic	Obsidian	Granitic
Density, ρ [kg/m^3]	2560	2720	2360	2650
Young's Modulus, E [GPa]	91	89	70	54
Poisson's ratio, ν	0.125	0.3	0.08	0.25

[Lógó and Vásárhelyi, 2019], granitic: $E_0 = 50$ GPa, $\nu_0 = 0.2$ [Klein and Carmichael, 2021]) were used to model resonant frequencies in air. E was fit to the first and second resonant frequencies of a selection of lithics, using $E = E_0 \times (f_{measured}/f_{modeled})^2$. To determine ν, we modeled the air resonant frequencies, using the new E, for $\nu = 0.6\nu_0,\ 0.8\nu_0,\ \nu_0,\ 1.2\nu_0,\ 1.4\nu_0$, and chose ν to minimize error between the measured and modeled frequncies below 20 kHz. Chosen values are shown in table 1.1, and are consistent with those in existing literature.

Digital Reconstruction of Lithics

Digital reconstructions of lithics were created by photogrammetry, using the software *Agisoft Metashape Standard*. The mesh generated by metashape was scaled and coarsened in *Autodesk Fusion 360*. Mesh size was chosen to balance the trade-off between model accuracy and computation time, keeping modeled resonances within 5% of those measured in air for frequencies up to 50 kHz. A tetrahedral mesh in the *Abaqus* file format was generated using *gmsh* for input into the acoustic models.

1.2.2 Recorded Resonance

The resonant frequencies of a selection of lithics were excited in air through direct percussion. Individual lithics rested atop a rubber band, allowing them to vibrate freely. Each lithic was struck by small metal spheres (BBs) about 20 times successively, with enough time between impacts for the lithic vibration to cease. The lithic was re-positioned multiple times to ensure that all resonant frequencies would be excited. Resulting acoustic vibrations were

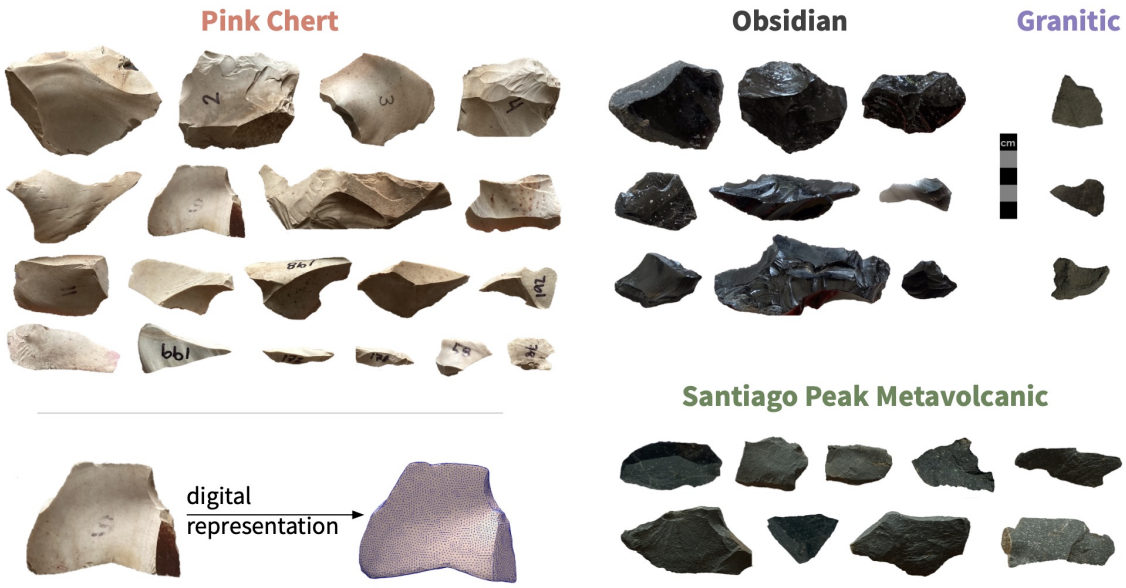

Figure 1.1. Lithics used in the analysis were of four materials: obsidian ($n = 9$), pink chert ($n = 19$), Santiago Peak metavolcanic rock ($n = 9$), and granitic rock ($n = 3$). Bottom Left: example of a typical digital representation - Pink Chert 6 is shown here. Multiple photographs were combined by photogrammetry to make a 3D mesh representation of the lithic.

measured with an ultrasonic microphone (*Song Meter SM4BAT FS*), positioned 1m from the lithic (fig. 1.2). Open-source audio software, *Audacity*, was used to edit the sound recordings and calculate an FFT of the vibrations recorded for each BB impact. The resulting ~ 20 spectra were averaged to increase signal-to-noise ratio and ensure that all resonant frequencies were apparent. Resonance quality factor, Q, was determined from the averaged spectra by the formula $Q = f_{max}/BW$ where f_{max} is the resonance frequency and BW the bandwidth.

In water, the resonant frequencies of the same lithics were again excited by direct percussion. Lithics sat atop a rubber band, suspended in a large cooler filled with fresh water ($\sim 0.8\text{m} \times 0.35\text{m} \times 0.3\text{m}$ interior dimensions). Each lithic was struck by a washer tied to a string, either dropped from above or jerked up from below by the experimenter. The washer hit different positions around the lithic to excite all resonance modes. Sound was recorded using the same system as before, but with an ITC-1042 hydrophone connected to the *Song Meter* recorder. Multiple spectra were obtained from the recordings and averaged as with the air measurements.

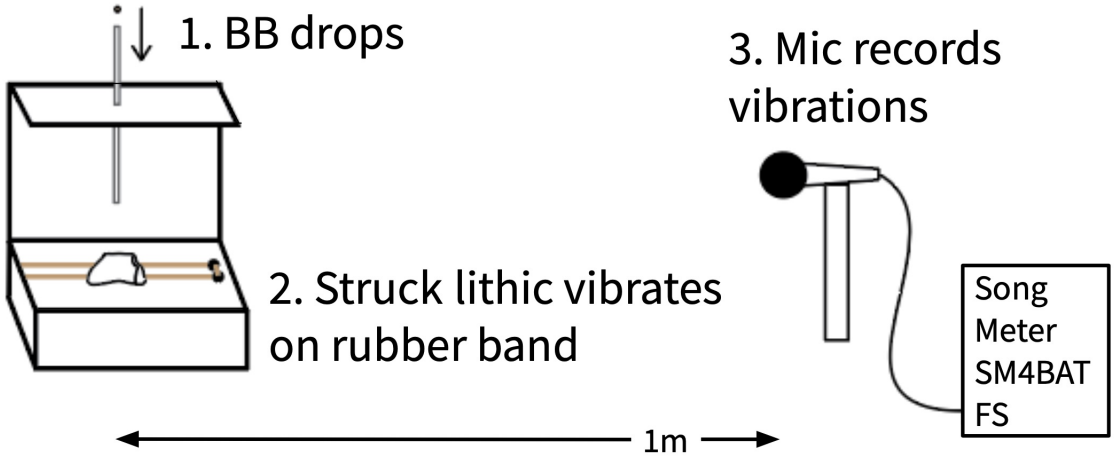

Figure 1.2. Schematic for recording lithic resonance in air. Specimen rests on a rubber band and is struck by a BB dropped from above. Vibrations are recorded using an ultrasonic microphone positioned at 1m range.

1.2.3 Modelling Free Vibration in Fluids

We used the package *FinEtoolsVibInFluids.jl* [Krysl, 2023] in the *Julia* programming language [Bezanson et al., 2017] to model the natural vibrations of individual lithics in air and water. The ESNICE energy-sampling stabilized nodal-integration method based on tetrahedral meshes was employed [Sivapuram and Krysl, 2019]. Lithics are described in the model by their shape (tetrahedral mesh as in fig. 1.1) and material properties (ρ, E, ν given in table 1.1). The surrounding acoustic fluid is described by density ($\rho_{air} = 1.2$ kg/m^3, $\rho_{water} = 1000$ kg/m^3). From this modelling, we obtained the natural bending shapes for each lithic and the corresponding resonant frequencies (fig. 1.3).

1.2.4 Acoustic Color Simulation

The acoustic color simulation uses coupled finite element and boundary element models to compute the scattered pressure field produced by an acoustic target, in this case a lithic, in a fluid medium (fig. 1.4); this technique is described for axially symmetric targets in [Abawi and Krysl, 2017]. As in the free vibration models, lithics are described by their shape (tetrahedral mesh) and material properties (ρ, E, ν (table 1.1)). The surrounding acoustic fluid

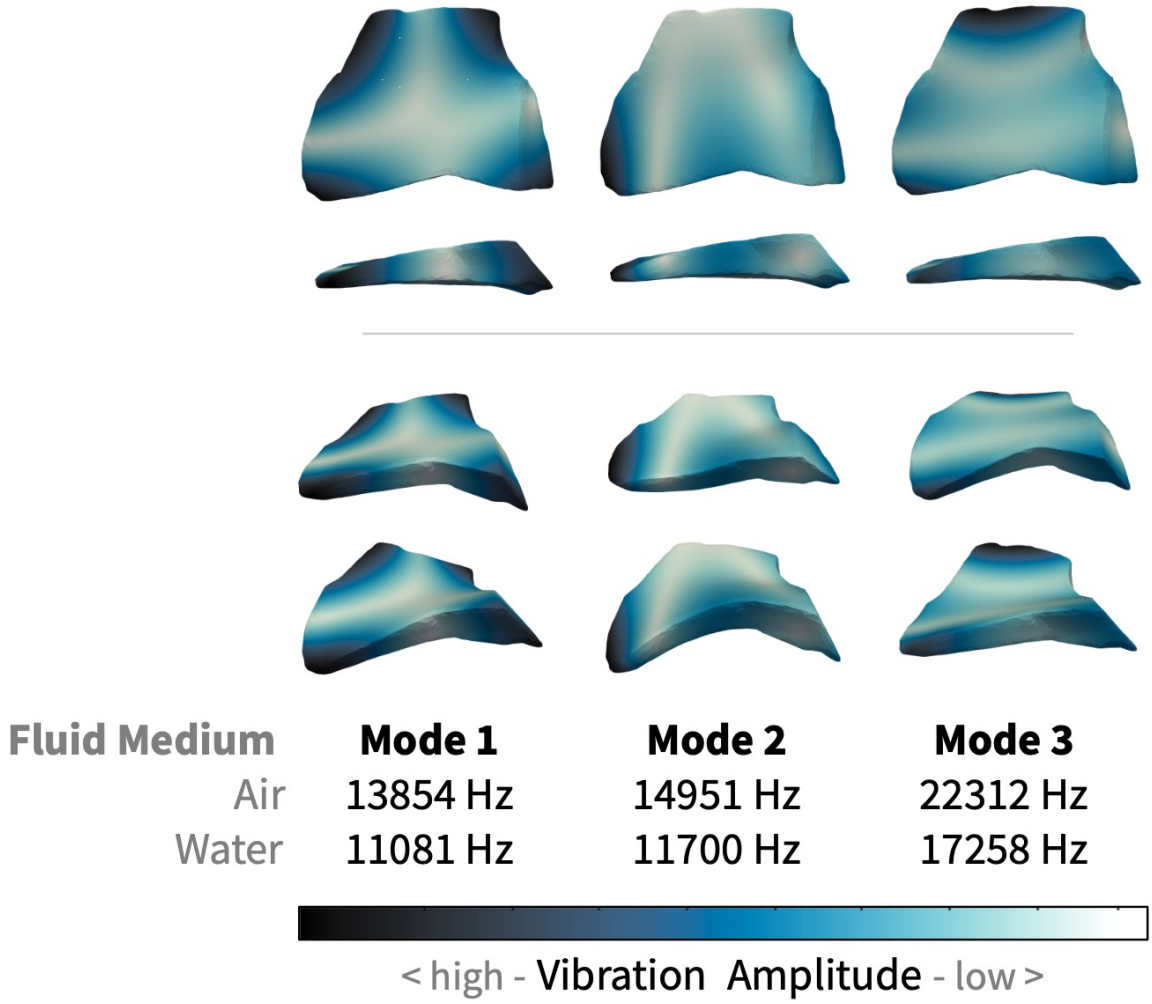

Figure 1.3. Vibration bending shapes for first three modes of specimen Pink Chert 6, with corresponding resonance frequencies in air and water. Darker shading corresponds to maximum vibration amplitude, while white corresponds to displacement nulls. Both undeformed (top) and deformed (bottom) lithic shape is shown for each mode.

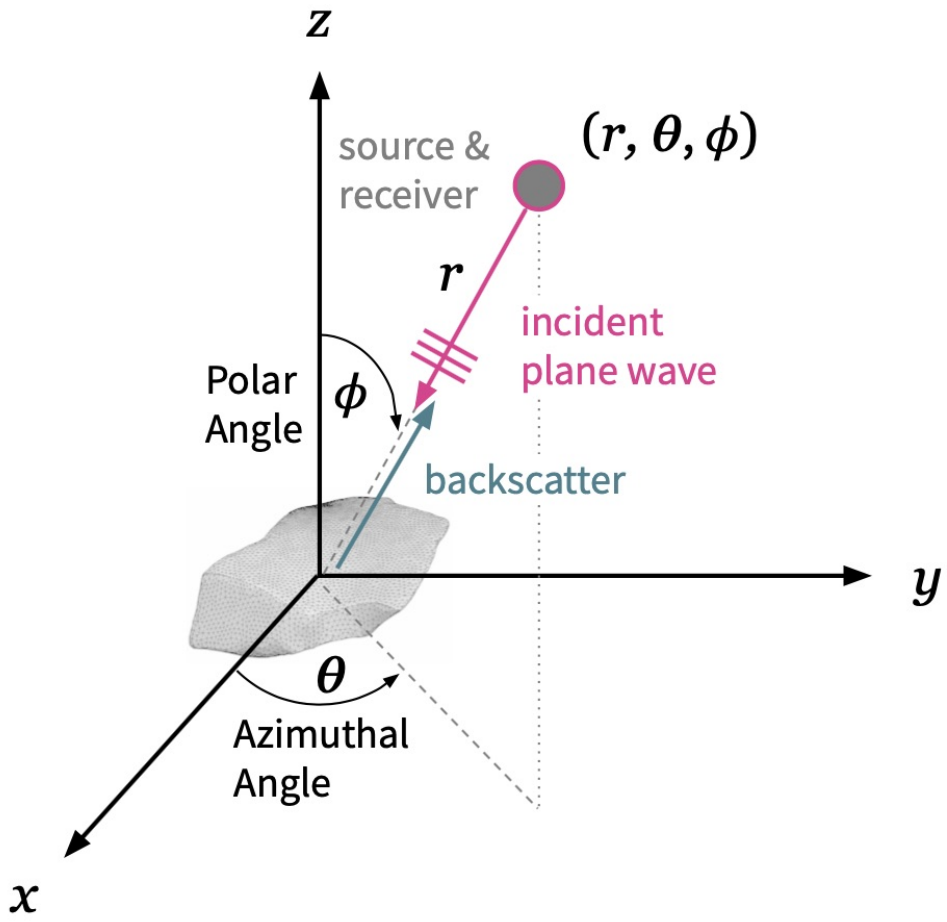

Figure 1.4. Acoustic color calculation geometry and coordinate system. The target lithic is positioned with it's first two principal axes in the x, y plane (the Pink Chert 6 mesh is shown as an example). Co-located source/receiver location is specified by distance, r, from the lithic center, azimuthal angle θ, and polar angle ϕ. The source emits a plane wave at a chosen frequency and the receiver records the backscatter.

is here described by both density ($\rho_{air} = 1.2$ kg/m^3, $\rho_{water} = 1000$ kg/m^3) and sound speed ($c_{air} = 344$ m/s^2, $c_{water} = 1500$ m/s^2) through the medium. An acoustic source and receiver are co-located at a location specified by distance from the lithic center (r), azimuthal angle (θ), and polar angle (ϕ, measured from the lithic normal). The source emits a plane wave at a chosen frequency and the receiver records the resulting scattered pressure, providing the lithic target strength as a function of frequency and incidence angle.

1.2.5 Thin Plate Vibration Approximation for Lithics

The first two lithic resonance frequencies can be approximated using the free-vibrations of a thin plate. Resonance frequencies for a freely vibrating thin plate depend on the plate's length, width, and thickness (l, w, t) and material properties (ρ, E, ν). For plates vibrating in a fluid medium, the frequency depends on the density of the surrounding medium as well. The first two dry resonance frequencies, as well as the ratio of wet/dry frequencies, are given for pink chert and obsidian in figure 1.5. Santiago Peak metavolcanic frequencies are similar to the pink chert frequencies (within 0.5%). For a more complete treatment of vibrating plates, see [Blevins, 2016].

To use the thin plate approximation for lithics, we chose plate dimensions $l =$ maximum lithic length, $w =$ maximum lithic width, and $t =$ average lithic thickness, where length, width, and thickness are measured along the first three principal axes of the lithics. Measurement examples are given in figure 1.6.

1.3 Results

1.3.1 Measured Lithic Resonance in Air and Water

Modelled resonance frequencies for lithics freely vibrating in air were compared to measured resonance frequencies; one example for each material is shown in fig. 1.7. The measured vibration spectra for each specimen show a series of distinct peaks between 5 - 50 kHz. The free vibration model results are overlaid as vertical lines, and the differences between modelled and measured frequencies under 50 kHz were less than 5% for all lithics, with the exception of one resonance of Granitic 4 which differed by 5.4%. The number of resonant lines and the resonant frequencies of the lines varied for each specimen, owing to the specifics of the specimen shape and material properties. This supports the validity of the model, confirming that the lithics have acoustic peaks at free vibration resonance frequencies. The in-air measured vibration spectra for the metavolcanic and granitic specimens were noticeably noisier than the

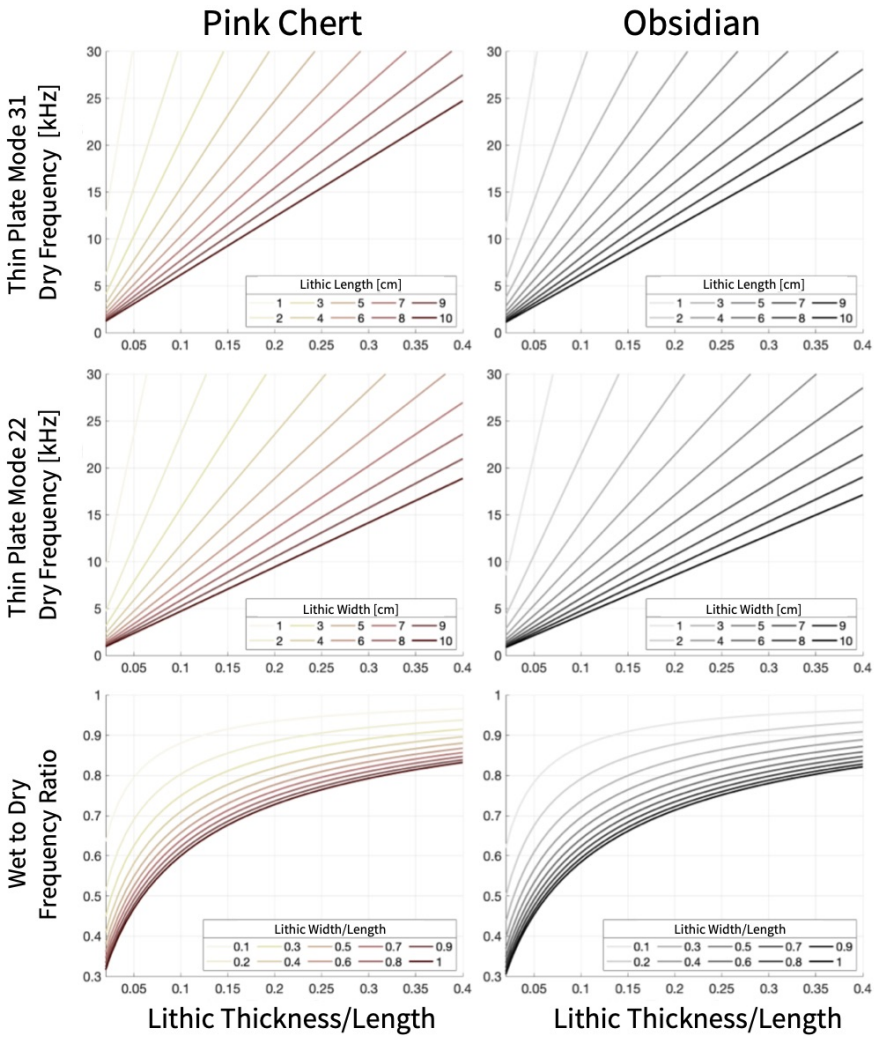

Figure 1.5. Plots to estimate the first and second resonance frequencies of a thin plate freely vibrating in air and water based on its dimensions (length, width, thickness) and material (as similar to chert or obsidian). Top, Middle: Frequencies for the first and second dry resonance modes as a function of lithic dimensions. The top plot describes a mode dependent only on length and thickness, while the middle is dependent on width as well. Which frequency is lower depends on the lithic's width to length ratio, so if using this figure to estimate the fundamental frequency, we suggest estimating both and choosing the lower one. To estimate resonance frequencies, divide thickness by length and find this value on the x-axis, then go up to the line that corresponds to the plate length or width, and observe the frequency on the y-axis. Bottom: Ratio of wet/dry resonance frequencies as a function of lithic dimensions. The resonance frequencies in water will be the resonance frequencies in air multiplied by this ratio. To estimate the wet/dry ratio, divide thickness by length and find this value on the x-axis, then go up to the line that corresponds to the plate width divided by its length, and observe the ratio on the y-axis.

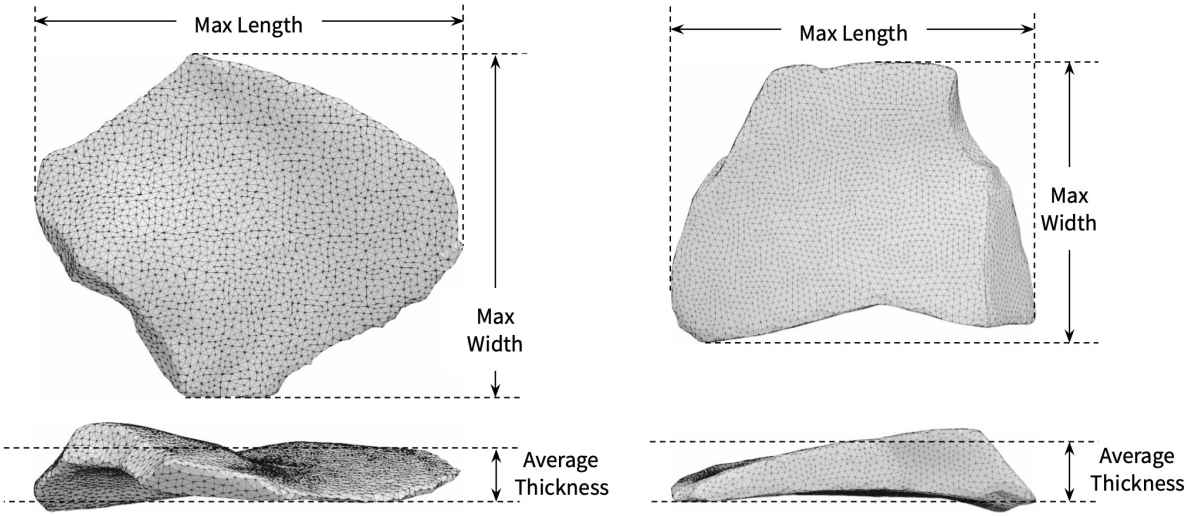

Figure 1.6. Lithic dimensions used in thin plate approximation. We measured dimensions using the 3D meshes, where length, width, and thickness are measured along the first three principal axes of the lithic. We chose plate dimensions $l =$ maximum lithic length, $w =$ maximum lithic width, $t =$ average lithic thickness.

other material types, with wider and shallower resonance peaks. This is reflected in the resonance quality factors which, for frequencies under 30 kHz, range from $Q \sim 100-670$ for Pink Chert, $Q \sim 120-860$ for Obsidian, $Q \sim 40-200$ for Santiago Peak Metavolcanic, and $Q \sim 30-70$ for Granitic lithics.

Modelled and measured resonance frequencies for underwater lithics are compared in figure 1.8. As with the in-air measurements, spectrum peaks occur near frequencies predicted by the free-vibration model, with the granitic lithic showing the least agreement. Some noise and erroneous lower frequencies are present due to acoustic waves bouncing around in the cooler used for measurement.

1.3.2 Submerged Lithic Acoustic Response

We computed backscattered target strength from a plane wave source at a co-located receiver 5m from the lithic. The target strength for frequencies 2-30 kHz and angles $\theta = 0$, $\phi = 0^\circ - 180^\circ$ is shown in fig. 1.9 for a single lithic, oriented as shown in fig. 1.4. Strong responses appear as vertical lines in fig. 1.9, at frequencies consistent with predicted resonance frequencies.

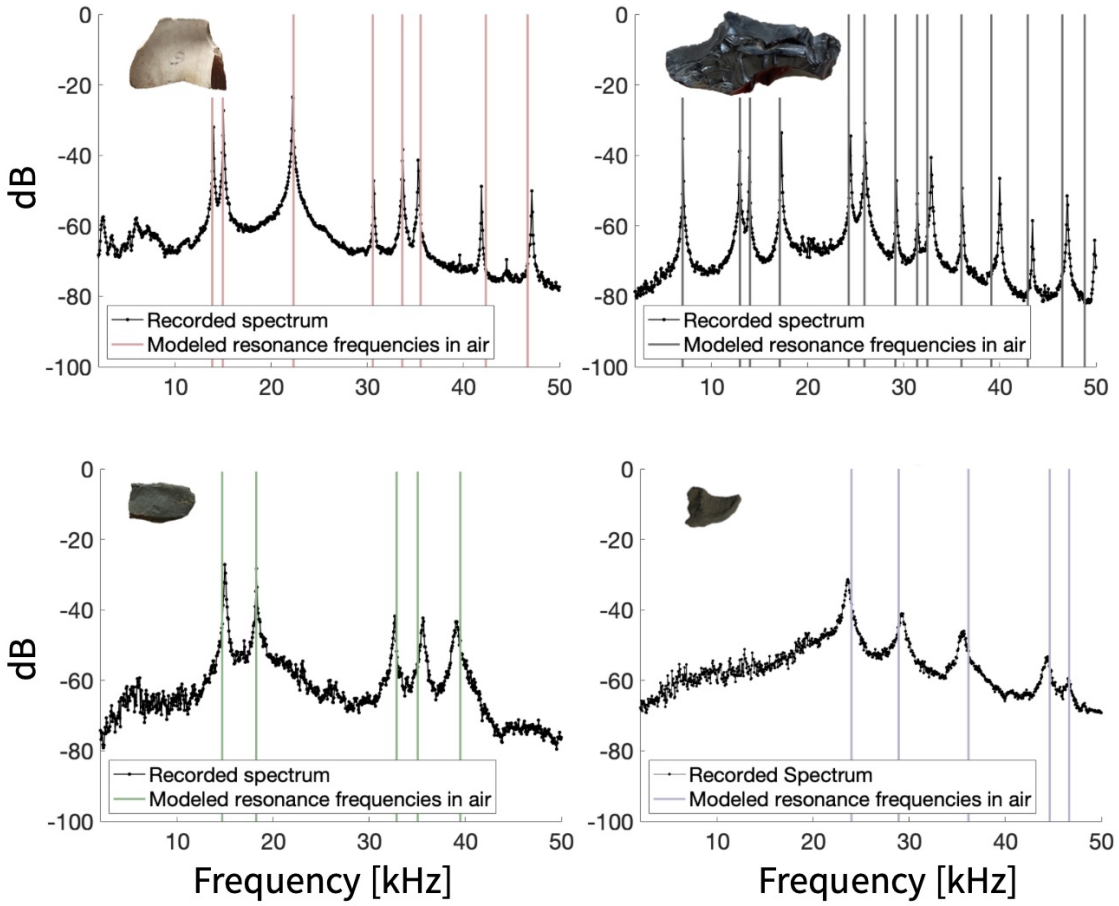

Figure 1.7. Resonance spectrum measured for four lithic examples (one for each material type - Pink Chert 6, Obsidian 13, Metavolcanic 2, and Granitic 10) with free vibration model results overlaid as vertical lines. Differences between modelled and measured frequencies under 50 kHz were less than 5% for all lithics, with the exception of one resonance of the lithic named Granitic 4 which differed by 5.4%.

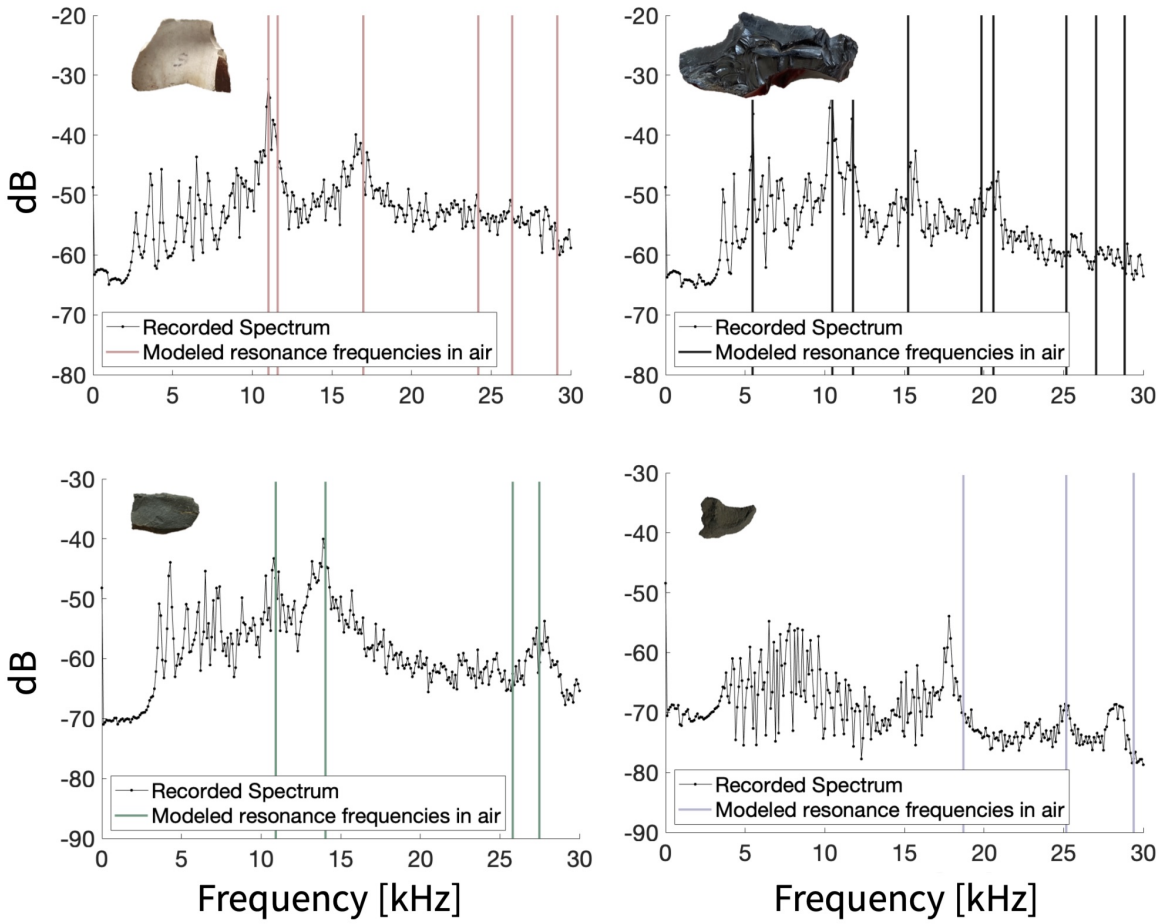

Figure 1.8. Resonance spectrum measured in water for four lithic examples (one for each material type - Pink Chert 6, Obsidian 13, Metavolcanic 2, and Granitic 10) with wet free vibration model results overlaid as vertical lines. Non-modelled peaks below 10 kHz are common to all lithic spectra and are likely due to standing waves in the cooler used for measurement.

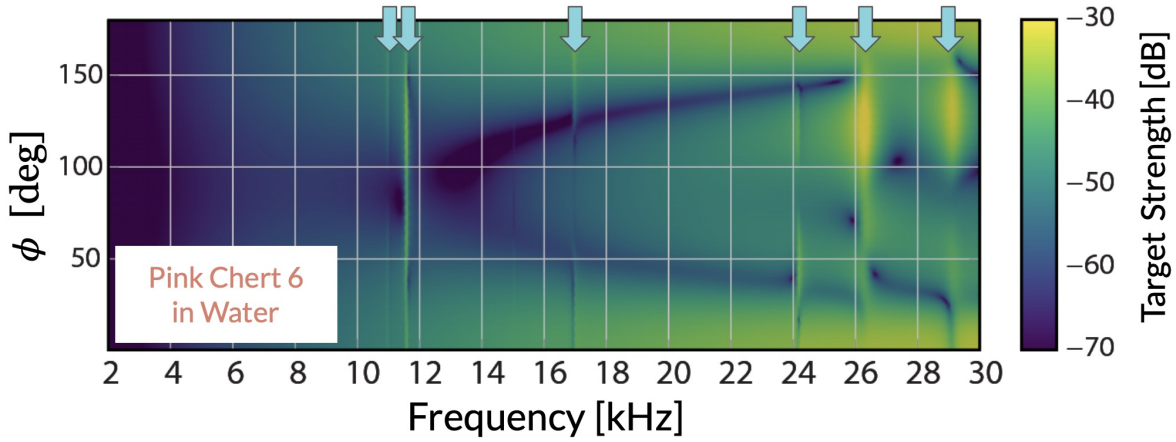

Figure 1.9. Target strength plotted with respect to incident polar angle, ϕ, and frequency for the Pink Chert 6 specimen, oriented as shown in fig. 1.4. Frequencies with distinctly high target strength, indicated with blue arrows, correspond to predicted free vibration frequencies in water. Color bar for target strength at right.

For non-resonance frequencies, maximum backscatter is observed at normal incidence ($\phi = 0°$ and $180°$ in fig. 1.9), however, at resonance frequencies the signal does not follow this pattern and maximum backscatter is typically not at normal incidence. Further, different resonant modes for the same lithic can be optimally excited at differing angles. The polar angle, ϕ_{max}, of maximum target strength is shown for every resonance of all specimens from 2-30 kHz in fig. 1.10. Most resonances are maximally excited at a range of angles $42° - 66°$ from normal incidence. Maximum target strength appears highest at frequencies 8-16 kHz. Fig. 1.11 shows resonance response for polar incidence angles up to $90°$ averaged over the 37 modern specimens and resonance frequencies. Maximum target strength is excited at $\phi_{max} = 55°$ for the average of each of the three modern-lithic materials. Averaged over these 37 lithics, over half the peak signal is excited/received between $37° - 73°$ from normal incidence. The average maximum target strength for the analyzed lithics is -27.83 dB, which is about 10 dB stronger than the average normal incidence response of -38.95 dB. Modelling of the three granitic lithics produced qualitatively similar results, with an average target strength of -27.45 dB at $\phi_{max} \sim 50°$ and -48.33 dB at normal incidence.

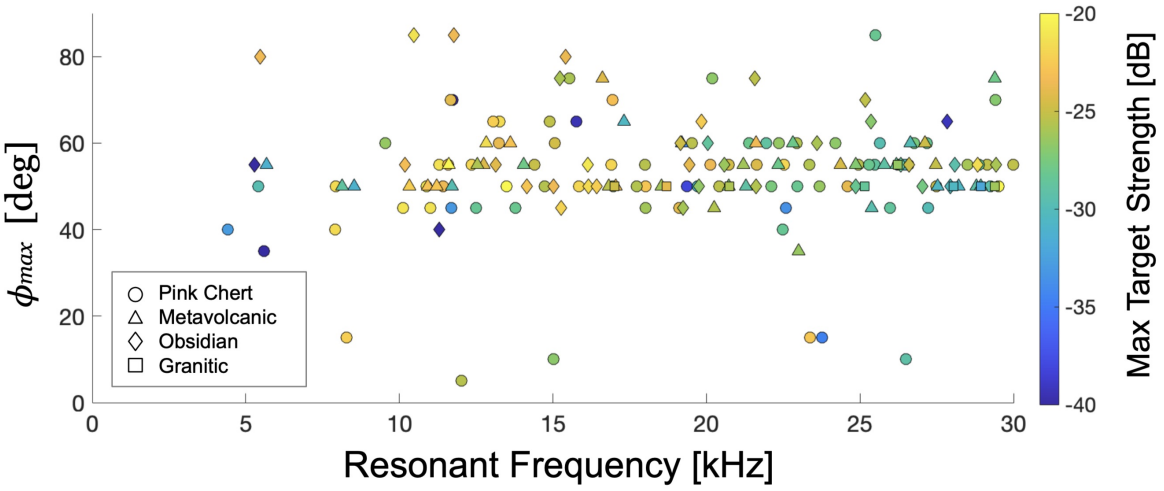

Figure 1.10. Polar angle of maximum target strength, ϕ_{max}, versus resonant frequency for all modes of all specimens. ϕ_{max} is clustered around $54^\circ \pm 12^\circ$ for all materials (see symbol shape). Maximum target strength appears highest at frequencies 8-16 kHz. Color bar at right shows target strength.

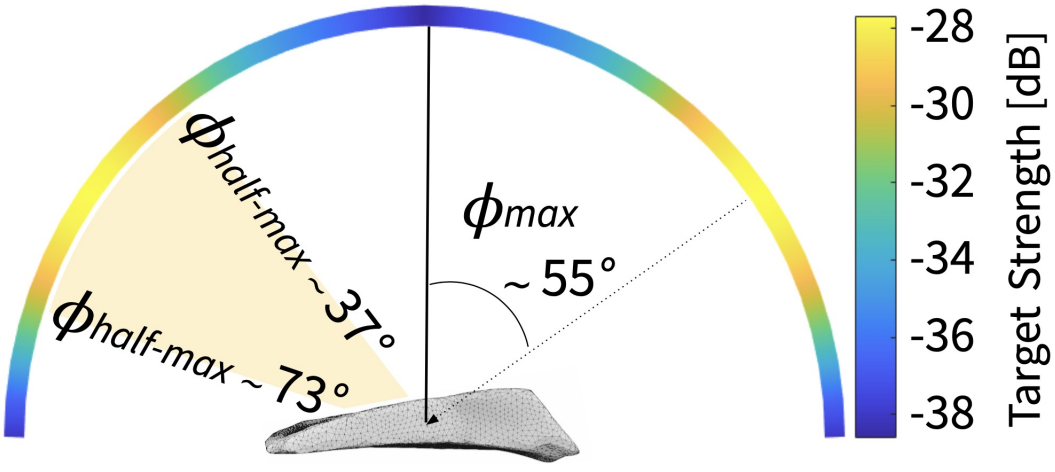

Figure 1.11. Maximum target strength occurs at angles between $37^\circ - 73^\circ$ from the normal, averaged over the 37 modern specimens. The angle with maximum return is $\phi_{max} = 55^\circ$ for each material type, both separately and combined.

1.4 Discussion

Lithics of varied shapes, sizes and materials have multiple resonances between 2-30 kHz in air and under water, which can be both observed by measurement and predicted by finite element free vibration models. In all cases, the lithics have visible resonance peaks in the 2-30 kHz range (examples in fig. 1.7). Obsidian and chert produce distinct resonant peaks, and while the metavolcanic and granitic specimens produce noisier vibration spectra, their resonance peaks are still pronounced. This indicates that the resonance phenomenon is strong for a range of lithic materials, but the resonance quality factor, Q, decreases as the material becomes more rough and crystalline. Modeled resonance frequencies line up remarkably well with the measured spectral peaks, even for complex shapes with many resonant modes (e.g. Obsidian 13), leading to increased confidence in the model results. The coarser crystalline structure of the granitic material may decrease the model's validity for these lithics, as it approximates the lithics as homogeneous and isotropic elastic bodies. The model did, however, reasonably correspond with measured resonance frequencies, so we include model results for the granitic lithics, but keep their results separate when presenting averaged values.

Modeling of the lithics in water still results in strong resonances, with the strongest resonance response at frequencies between $\sim 8-16$ kHz (fig 1.10). These models also reveal that the maximum acoustic backscatter occurs at the resonance frequencies and is highly directional. A cross section of the results from a single lithic simulation are shown in fig. 1.9. Polar angles of $\phi = 0^\circ$ and 180° correspond to the acoustic wave being normally incident on the flat face of the lithic, while $\phi = 90^\circ$ corresponds to a wave coming in from the side, directed at the sharp edge of the lithic. For most frequencies, the strongest backscattered signals are achieved near normal incidence, which have the largest scattering cross-section, while waves incident on the sharp edge of the lithic are not strongly scattered. However, at a narrow set of frequencies, which correspond to the predicted underwater resonance frequencies, a stronger acoustic response is observed. Two important aspects of the resonant response are: (1) some resonant frequencies

have a stronger signal than others, with the fundamental resonance not necessarily returning the highest amplitude; and (2) the resonance signal is strongest at angles off from the normal incidence. Excitation and reception of the resonance signal is highly directional, leading to the highest backscattered amplitude at angles $\phi_{max} = 37^\circ - 73^\circ$. While fig. 1.9 is for a single lithic, the characteristics described are consistent for other specimens. The maximum resonance response is consistently recorded off normal incidence, regardless of lithic material or dimensions (fig. 1.10). Resonance return does vary with azimuthal angle around the lithic, θ, but the pattern is individual to each lithic and θ_{max} can even differ for different resonant modes of the same lithic. In practice, this means that, depending on the sonar path over the lithic, some resonance frequencies will be more detectable than others. Additionally, because maximum resonance is received at a consistent polar angle, lithics are likely more detectable laterally offset from the sonar instrument rather than directly below. The signal from an offset sonar path will pass through a range of azimuthal angles, increasing likelihood of hitting the lithic at its optimal angle for more frequencies.

The target strength excited at the optimal angle is significantly higher ($\sim$10 dB) than at normal incidence. On average, the maximum response is elicited at $\phi \sim 55^\circ$, likely because at these incidence angles, the acoustic wave can better align with the lithic shape in a way that excites resonance. For example, a plane wave angled off normal incidence would cause the lithic to bend into the deformed lithic resonance shapes in fig. 1.3 better than would a normally incident source. The optimal polar angle is similar for all lithic materials examined. This result has practical implications, and leads to the suggestion that detection of lithics by chirped sonar may be optimized using acoustic pulses with incidence angles $\sim 55^\circ$ toward the seabed.

This analysis focuses on individual lithics suspended in water, although lithics are not found floating in the water column and may not be alone. The next steps are to consider how burial in sediment will affect the acoustic signal and to explore the response of lithic concentrations. Burial in sediment will lower the resonance frequencies, because the sediment's density is greater than that of water. It may dampen the acoustic response, but since lithics buried

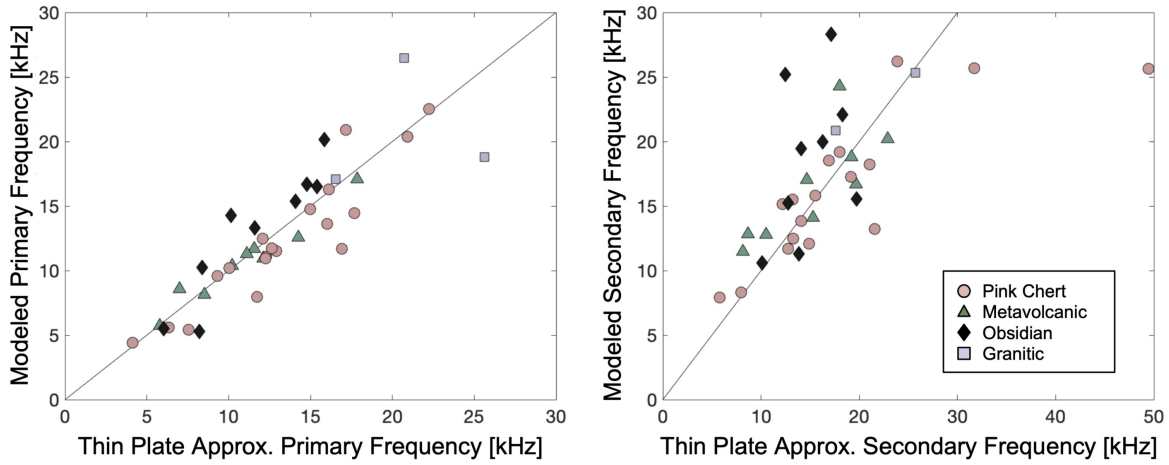

Figure 1.12. Modelled lithic resonance frequencies (left primary, right secondary) in water vs. predicted resonance frequencies from a freely vibrating thin plate approximation for debitage made of pink chert (pink circles), Santiago Peak metavolcanic (green triangles), obsidian (black diamonds), and granitic rock (purple squares).

up to 2m have been detected using chirp sonar in the field [Grøn et al., 2021], burial may not be a determining factor. Substrate material may have an effect on the optimal beam angle, since the acoustic wave will change direction at the water-seafloor interface in accordance with Snell's law ($c_{water}/\sin\phi_{water} = c_{sand}/\sin\phi_{sand}$). For example, if the substrate is sand in which the speed of sound is $c_{sand} = 1650$ m/s, a 55° pulse hitting a flat water-sand interface will become 64° traveling through the sand. It may then be advisable to use a shallower beam angle to find buried lithics, so that the wave interacting with the lithics is incident near 55°.

In the case of many lithics together, we would expect to see a broad range of frequencies producing strong responses. Given enough lithics, each with multiple resonance frequencies, the received signal may appear less like distinct, resonant peaks, and more like a consistently strong signal across many frequencies. The overall signal would depend on lithic assemblage characteristics and spatial distribution. In areas of long-term use for instance, with lithics densely deposited with depth, the lithics near the surface may shield the signal from those below. Additionally, the absence of a correlation between maximum signal and azimuthal response (θ) indicates that, even if all the lithics are aligned with their long axis in the same direction, as

may be the case when lithics are re-positioned by flowing water, the maximum signal would not predictably depend on the transect path over the collection. Another way to think of this is that, for a collection of flat-laying lithics, we expect the signature of the lithic concentration to be detectable in a cone-shaped region above the lithics whether they have random or aligned orientations. Further modelling, experiments, and field tests are needed in this area.

Our analysis shows that the first and second resonant frequencies of each lithic can be estimated using a thin plate approximation (fig. 1.12), in which the plate is described by the lithic's maximum length, maximum width, average thickness (l, w, t), and material properties (E, ν, ρ). This approximation can be used to identify the expected range of resonance frequencies in archaeological contexts where there is an broad idea of what lithic dimensions and material properties should be present. For example, larger debitage could be found at areas of initial reduction or on sites of cultures with lithic traditions that include macrolithics, whereas residential or resource exploitation sites are likely to contain relatively smaller lithic tools [Joy, 2020]. It may be possible to calibrate sonar parameters to focus on the expected relevant frequencies for these or other known contexts. Conversely, the thin plate approximation may be useful to gain information about lithic properties from the resonance frequencies measured in the field. As this is a rough approximation, we hope that further modelling and field work will lead to more advanced data processing methods to both detect and interpret the lithic signatures.

1.5 Conclusion

In this study, we simulate the acoustic response of lithic debitage in water as a step towards understanding the acoustic response of lithics in submerged sites. Strong resonance is exhibited in all lithics, with most having multiple resonances under 30 kHz. However, resonance quality appears to decrease with coarser granular structure of the lithic material, potentially making them more difficult to detect. The highest resonance signal strengths appear in the 8-16 kHz range. Models show that lithic detection based on resonance is highly directional.

For flat-laying lithics, target strength at normal incidence is on average 10 dB lower than the strongest signal, found about 55° from normal incidence. We suggest that the best way to detect submerged lithics may not be through standard mono-static sub-bottom profiling with a direct downward pulse, but instead with a beam angled $\sim 55°$ toward the sea bottom. If the lithics are buried, we suggest adjusting the beam angle so that the acoustic pulse travels through the substrate at $\sim 55°$.

The results presented here are for a co-located source and receiver. Since many chirp systems have a co-located source and receiver, our current results should be applicable to these existing systems. It should also be possible to design a bi-static sonar to exploit the directionality of the lithic response.

1.6 Acknowledgements

Thanks to G. Timothy Gross for sharing debitage with us. Thanks also to Ole Grøn, for his suggestions and groundbreaking research.

This research did not receive any specific grant from funding agencies in the public, commercial, or not-for-profit sectors. Funding for MAM provided by UCSD and the SIO Graduate Department.

Chapter 1, in full, is a reprint of the material as it appears in The resonant acoustic signatures of lithic debitage 2022. Morris, Margaret; Krysl, Petr; Hildebrand, John; Rivera-Collazo, Isabel, Journal of Archaeological Science: Reports 2022. The dissertation author was the primary investigator and author of this paper.

Chapter 2

Resonance of the tympanoperiotic complex of fin whales with implications for their low frequency hearing

Abstract

The tympanoperiotic complex (TPC) bones of the fin whale skull were studied using experimental measurements and simulation modeling to provide insight into the low frequency hearing of these animals. The study focused on measuring the sounds emitted by the left and right TPC bones when the bones were tapped at designated locations. Radiated sound was recorded by eight microphones arranged around the tympanic bulla. A finite element model was also created to simulate the natural mode vibrations of the TPC and ossicular chain, using a 3D mesh generated from a CT scan. The simulations produced mode shapes and frequencies for various Young's modulus and density values. The recorded sound amplitudes were compared with the normal component of the simulated displacement and it was found that the modes identified in the experiment most closely resembled those found with Young's modulus for stiff and flexible bone set to 25 and 5 GPa, respectively. The first twelve modes of vibration of the TPC had resonance frequencies between 100Hz and 6kHz. Many vibrational modes focused energy at the sigmoidal process, and therefore the ossicular chain. The resonance frequencies of the left and right TPC were offset, suggesting a mechanism for the animals to have improved hearing at a

range of frequencies as well as a mechanism for directionality in their perception of sounds.

2.1 Introduction

Knowledge of mysticete low frequency hearing sensitivity is needed to assess the potential impact of anthropogenic noise on their anatomy and behavior [Southall et al., 2019]. This is increasingly important due to the presence of noise from shipping traffic, seismic exploration, and offshore development in whale habitat [Hildebrand, 2009]. Particularly helpful would be knowing the frequency sensitivity of hearing for a variety of different whale species.

Studies of mysticeti hearing are sparse, particularly owing to the difficulty of conducting behavioral or electrophysiological studies. An alternative approach is to numerically model whale hearing capabilities, allowing simulated sound exposure without impacting live animals [Cranford and Krysl, 2015]. A modelling approach also enables studies of the effect of exposure to specific frequencies without the extra noise and extraneous effects that may be present in experiments with live animals.

The tympanoperiotic complex (TPC) plays a crucial role in whale hearing, serving as a functional unit composed of three major bony structures attached to the skull: the periotic, the tympanic bulla (including pedicles), and the ossicular chain [Mead and Fordyce, 2009]. In a pioneering study, Quiralte and Dell used elastic solid vibrations theory to explore whale hearing mechanisms, and focused on a specific component of the TPC, the tympanic bulla detached from the pedicles and the periotic bone [Quiralte and Dell, 2013]. Their finite element analysis revealed low-frequency (LF) mode shapes that displayed the greatest response near the malleus. As a result they concluded that the tympanic bone collects sound vibrations over its surface and concentrates energy at the malleus. However, the natural vibrations of the TPC in a living whale may be influenced by the attachments of the tympanic bulla to the skull through the pedicles and periotic bone. Our research examines the entire TPC and lays the foundation for more comprehensive models.

Our previous work [Cranford and Krysl, 2015] generated synthetic audiograms for a fin whale by applying finite element modeling tools to X-ray computed tomography (CT) scans. The simulations revealed two mechanisms that could excite the bony ear complexes: (1) the skull-vibration enabled bone conduction mechanism, and (2) a pressure mechanism transmitted through soft tissues. Bone conduction was determined to be the more effective mechanism. The mass density of the bony ear complexes and their firmly embedded attachments to the skull were found to be universal across the Mysticeti. Hence, the work hypothesized that sound reception mechanisms were similar in all baleen whales. The interactions between incident sound waves and the skull were thought to induce motion of the bony ear complex relative to the skull, subsequently transmitted through the ossicular chain, resulting in best hearing sensitivity for low-frequency sounds.

In this work, we combine direct measurements of the vibrations of the fin whale bulla with a vibroacoustic finite element model that has been previously used to successfully simulate sound production and sound beam formation produced by odontocetes [Cranford et al., 2013]. We include in the model the entire TPC, with the base of the periotic bone fixed in place to represent rigid attachment to the skull, and we simulate the natural modes of vibration. Direct measurements, which consisted of exciting vibration by tapping different spots across the TPC and recording the sound radiated in different directions, were performed on left and right TPCs still attached to the skull.

The vibrational measurements and modeling conducted in this study give insight into how the TPC may play a role in low frequency hearing. We can point to the pedicles and their characteristics and the material properties that affect their function, noting that the bulla can swing on them as if they were "door hinges" at the first few natural frequency modes (for example, in the lowest resonance mode, supplementary files). For higher frequency modes the displacement patterns tend to be more complex, with many modes concentrating energy at the sigmoidal process and therefore the malleus and the ossicular chain. The model results were found to be consistent with the experimental results, validating the modelling technique for fin

whales. This result suggests that these modelling techniques could also work for other mysticetes which are morphologically similar. Since we are dealing with a particularly complicated and integral component of the mysticete hearing mechanism, our work can put in place pieces of the validation to support models that incorporate the entire skull.

2.2 Materials and methods

2.2.1 Fin Whale Skull

The skull used for this study is from an adult male fin whale (*Balaenoptera physalus*) with a straight length of 17.25 m, as recorded in the Marine Mammal Stranding Report Level A Data (Field Number :SWFSC-KXD0249, National Database Number :SW-2014-1157143) of May 19, 2014. The whale was first spotted floating, freshly deceased, by the Wastewater Treatment Plant at Point Loma in San Diego County, CA. The head was collected by Ted Cranford (SDSU) and transported to Camp Elliot Field Station. The head rested on the surface of the ground, covered with a black plastic tarp allowing dermestid beetles, also known as "skin beetles," to clean the soft tissues from the skeletal elements. Following this, the skull was kept at Camp Elliot covered by a tarp. The skull was wrapped in chain-link fencing to hold the bones together during and after transport.

Both left and right TPC were attached to the fin whale skull. At the time of the experiment, the skull rested atop foam padding, ventral-side up so both TPC were exposed (Fig 2.1). The incus and malleus were present on both sides, but the ligament connecting them was absent. We were unable to determine whether the stapes was in place.

2.2.2 TPC Vibration Measurement

We measured the left and right TPC separately, using the following process. Eight *Pyle PDMIC58* microphones were positioned around the tympanic bulla, arranged on a frame as shown in Fig 2.1. The microphones were separated and held in place by a slab of foam to prevent

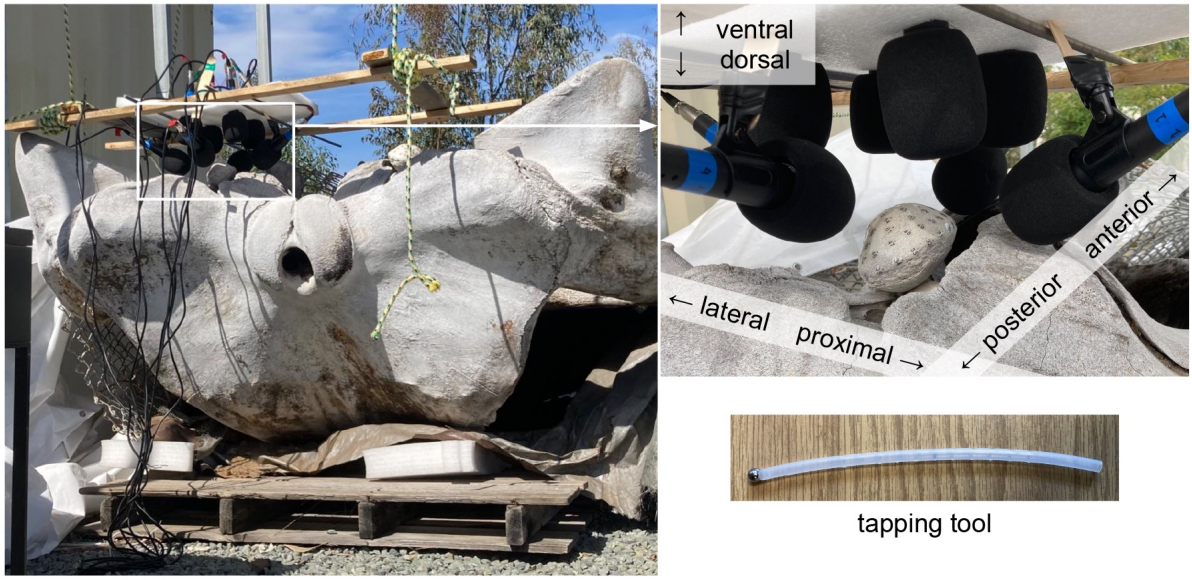

Figure 2.1. Recording arrangement. The fin whale skull rests ventral-side up with both left and right TPC exposed (left). Each TPC is covered in stickers numbered 1-89 with like numbers in comparable places on both TPCs. An arrangement of 8 microphones, labelled 1-8, is suspended over one TPC at a time (top right). Microphones are connected to a *MOTU 8pre* (out of frame) to facilitate simultaneous recording using the *Audacity* app for macOS. The tapping tool used was a 6mm diameter steel sphere adhered by silicone onto the end of a polyurethane tube (bottom right).

noise caused by resonance of a rigid frame. The microphone setup was suspended above the ventral-side-up skull to prevent any interaction between the frame and the vibrations of the TPC bones. Four microphones were positioned to face the anterior, posterior, lateral, and proximal sides of the TPC, while the remaining four were arranged in a plane directed towards the ventral side of the TPC. All eight microphones were connected to a *MOTU 8pre* for simultaneous recording using the *Audacity* app for macOS.

Numbered stickers were used to designate tap locations in visually comparable places on both left and right TPCs, with a higher concentration on and near the sigmoid process. A total of 89 tap locations were designated: Eighty-five on the tympanic bulla, one on the anterior pedicle, and three on the periotic bone (Fig 2.2). The posterior pedicle was excluded from tapping because it was too difficult to reach. At each tap location, we initiated a new recording, then used the tapping tool (Fig 2.1) to strike the bone at least 20 times with a short pause between each tap. Recordings from each tap location were exported as wav format files to be processed in *MATLAB*. We computed the power spectrum of the coherent sum of 20 taps from each tap location, and normalized the spectra at 15kHz.

The tapping-tool used was a 6mm steel sphere affixed to the end of a short polyurethane tube by silicone gel. To alleviate any concern about the effect of the tapping tool itself on the experimental results, we repeated taps at 3 tap locations with a variety of potential tapping tools: (1) a straight metal pick, (2) a steel nut jammed on the end of a short polyurethane tube, (3) a metal BB affixed to a thin, pliable plastic rod by silicone gel, and (4) a 3mm diameter sphere affixed to a medical lancet device by silicone gel. Each chosen location was tapped with each device 20 times: 10 times with light force, and 10 times with moderate-high force, with the exception of the modified lancet with which 10 taps total were performed. While the strength of force is subjective, the same human did all of these taps and judged that the ‘light’ and ‘heavy’ force taps would be at the extreme ends of the taps performed during the full experiment. We found that the nut (2) gave the most consistent result, likely due to its mass. Due to concerns about the geometry of the nut, it was replaced by a solid steel sphere of comparable mass in the

Figure 2.2. TPC tap locations. Tap locations denoted by stickers numbered 1-89 placed with like numbers in visually-comparable places on both TPCs. Tap locations are on the bone, just beyond the gray dot at the top of each sticker. Top Left: Right TPC posterior and lateral views. Top Right: Left TPC lateral and posterior views. Bottom Left: Left TPC anterior and proximal views. Bottom Right: Right TPC proximal and anterior views. All views are shown ventral-side-up, as this was the skull orientation during the experiment. The authors note that the stickers may not be in perfectly homologous locations; however, coverage over each TPC is comparable and TPC-scale vibration patterns are captured by both arrangements.

final tapping tool.

2.2.3 TPC Vibroacoustic Model

We modeled the natural mode vibrations of the tympanic bone and ossicular chain with a finite element model developed using the programming language *Julia* [Bezanson et al., 2017, Krysl, 2021]. A 3D mesh of the fin whale TPCs were generated from a CT scan. The fin whale CT scan was from a calf (NMNH 571562) discovered at the Smithsonian Institution without further stranding data. The CT images of the left TPC showed that the stapes was out of place. The stapes was consequently not included in the simulation mesh of the left TPC. The right TPC simulation included the entire ossicular chain. However, we were able to remove elements of the ossicular chain in some of the simulated meshes to compare differences between the left and right sides having the same anatomical elements in place.

Because the mesh included just the TPC, the base of the periotic bone was fixed with zero displacement, since it is embedded in the skull, and the rest of the model was allowed to move relative to the periotic bone's attachment to the skull. Output of the models included the frequencies of natural vibration, and the relative displacements across the bone occurring for each vibrational mode. Physical properties of the bone are shown in Table 2.1 and were chosen based on the literature [Lees et al., 1996, Tubelli et al., 2014, Tubelli et al., 2018, Zhang and Gan, 2011, Tsukrov et al., 2009].

2.3 Results

Tapping the TPC resulted in the excitation of a set of well-defined resonance peaks within the frequency range of 100Hz to 6kHz. The overall pattern of resonant peaks was similar for all the microphones, although there were differences in the strength of the recorded sound related to the position of the microphone and the tap location. We present the average spectra over all tap locations for each microphone, as well as the average over all microphones (Fig 2.3). From the spectra, we identified resonance frequencies corresponding to the first 12 simulation modes

Table 2.1. Material properties used in the models. Hard bone includes the periotic and tympanic bone, malleus, incus, and stapes. Soft bone describes the anterior and posterior pedicles. The malleolar incudal ligament and incudostapedial ligament are set to stiff, and the annular ligament is flexible. Where multiple values are included, separate simulations were run with each of those values.

Material Property	Stiff Bone	Flexible Bone	Stiff Ligament	Flexible Ligament
Density, ρ [kg/m^3]	2300, 2400, 2500	2000	1200	1200
Young's Modulus, E [GPa]	10, 15, 20, 25	5, 7, 9	0.001	0.001
Poisson's ratio, ν	0.3	0.3	0.3	0.45

(described below). Peaks that were identified as resonance modes appeared to some extent on all microphones for both TPC. For all modes, the left TPC produced a higher-frequency peak than the right TPC.

Our simulations yielded the mode shapes and corresponding frequencies for the TPCs at various Young's Modulus and density values. To establish a correlation between our experiment and these simulations, we compared the recorded sound amplitudes with the normal component of the simulated displacement. The strength of the resonant motion normal to the bone surface should correspond with how well a particular resonant mode is excited by tapping along the normal to the surface at that specific location. We identified the normal component of the simulated displacement to determine how each mode responds to tapping, and compared it with the recorded amplitudes.

The simulations revealed resonance modes involving the whole TPC and others exhibiting more localized vibration in the ossicular chain, with the tympanic bulla remaining stationary. In the physical experiment, the malleolar-incudal ligament was absent, so we would not expect the latter of those modes to be excited. When the simulation was run with the incus and stapes removed, these resonances disappeared as expected, while the others persisted. For these modes, the vibrations across the tympanic bulla and pedicles remained relatively unchanged with or without the ossicular chain present in the simulation, yet they still resulted in movements of the

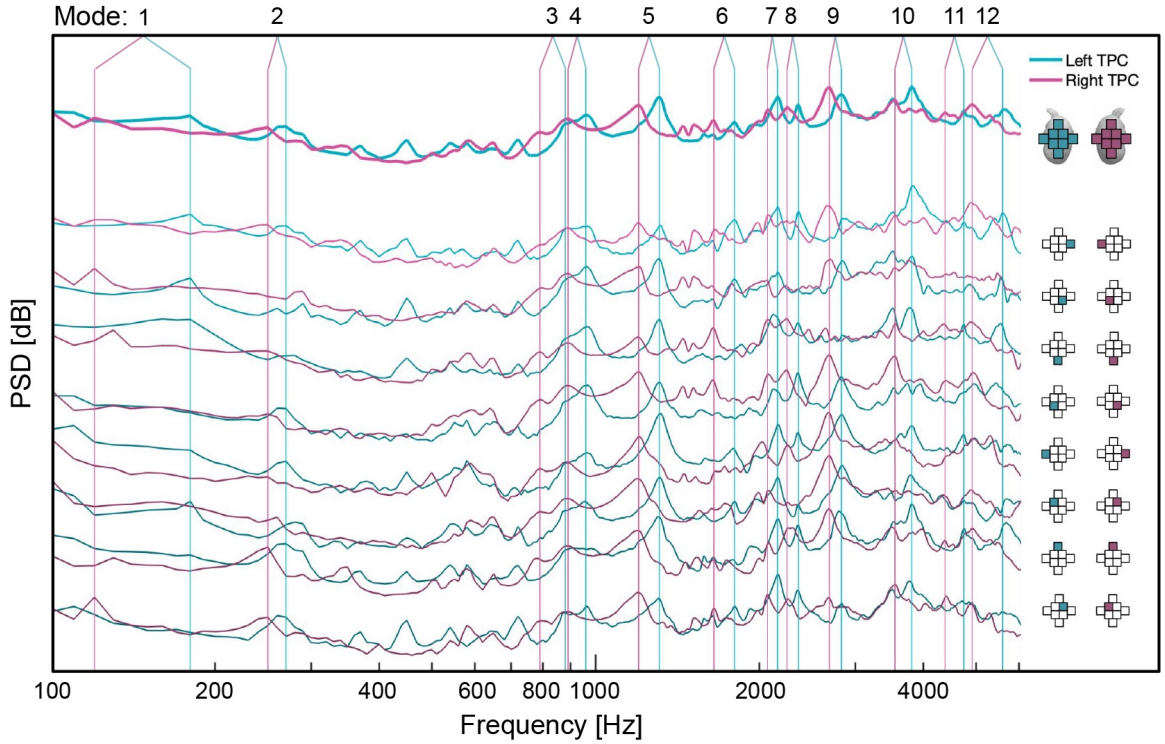

Figure 2.3. Spectra averaged across all tap locations. Spectra for the left and right sides are shown in blue and red respectively. The average across all microphones is shown at the top in bold. Spectra are displayed offset below for each microphone. The right panel indicates the position of the microphone relative to the TPC shown at the top of the panel. Vertical lines indicate the peaks identified as the first 12 resonance modes present in all simulations with or without the incus and stapes included.

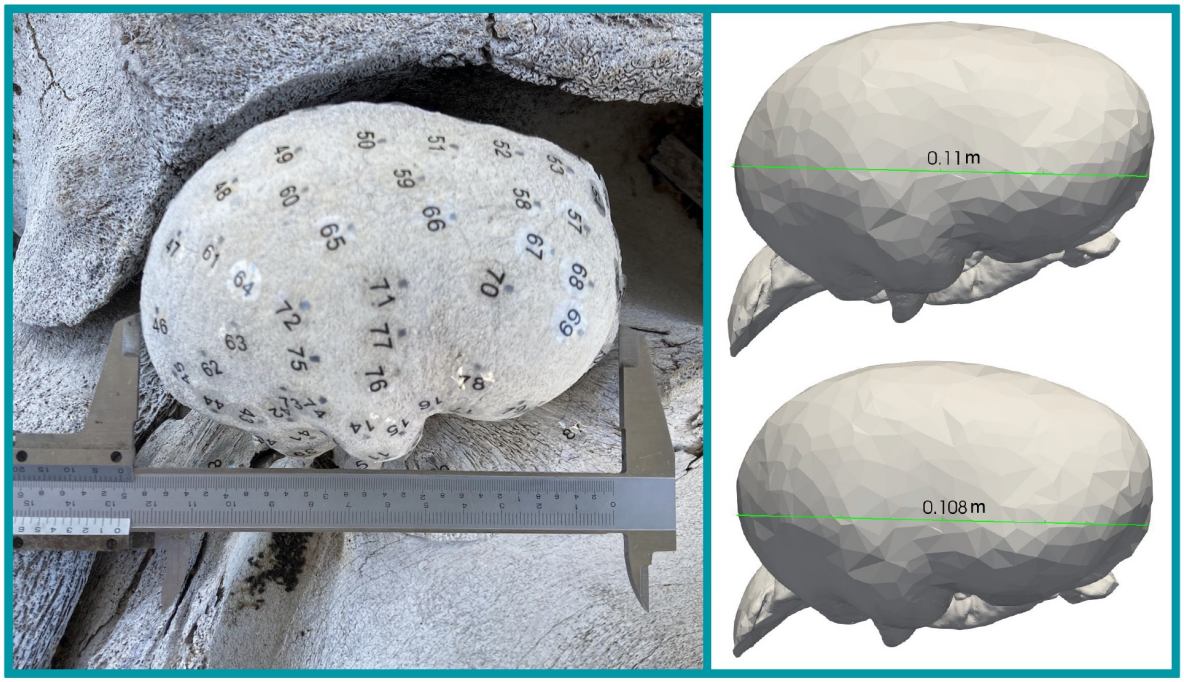

Figure 2.4. Size comparison between left TPC of the experiment and the simulation. Left: Left TPC of the experiment with calipers measuring 12.8cm TPC 'length'. Right: Left TPC mesh with two alternate 'length' measurements. The top and bottom measurements are the longest and shortest reasonable 'length' measurement that could correspond to the dimension measured in the left panel. Although it is imprecise to compare sizes based on a single measurement, the comparison is meant to demonstrate that the TPCs in the experiment are larger than those in the simulation.

malleus, which, in turn drives motions through the ossicular chain. The resonance frequencies and mode shapes were only slightly altered. We focused on the first 12 vibration modes present with and without the ossicular chain included in the simulation, referring to them as frequency modes 1-12.

We also ran the simulation with the TPC mesh uniformly scaled up because the tapped TPCs have larger dimension than the simulated TPCs (Fig 2.4). Measurements of the ratio between the tapped TPCs and the simulated TPCs varied from 1.16 to 1.19. We scaled the mesh by a factor of 1.2, which we chose as an upper-bound for the size difference. The simulated mode shapes were nearly identical between the scaled and original meshes. Frequencies were lower by a factor of about 1.2 for the scaled mesh.

The simulations varied the density for the stiff bone and the Young's moduli for both stiff and flexible bone (Table 2.1). Increasing the Young's modulus generally resulted in a higher resonance frequency, while increasing the density led to a lower resonance frequency. Modes 1-3 and 7-10 exhibited consistent modes shapes, but the order of modes 4-6 changed when Young's modulus was altered. Specifically, modes 4, 5, 6 with Young's modulus for stiff and flexible bone set to 25 and 5 GPa respectively, correspond to modes 6, 4, 5 when Young's modulus for stiff and flexible bone were set to 10 and 9 GPa. We found that the modes identified in the experiment most closely resembled the order found with Young's modulus for stiff and flexible bone set to 25 and 5 GPa.

The modeled resonance frequencies are in good agreement with the measured frequencies when the modeled TPC is uniformly scaled by a factor up to 1.2, the approximate size difference between the modeled and measured TPCs (Fig 2.5). We also show the amplitude of the received sound at each microphone for select frequencies, displayed for each tap location on an image of the tapped-TPC (Fig 2.6). Specifically, Figures 2.7, 2.8, 2.9 show modes 3, 9, and 11 respectively. All mode comparisons are included in the supporting material (Fig 2.10 to Fig 2.33). Our analysis revealed that the pattern of tap locations resulting in the highest amplitude of radiated sound correspond to regions of the model with high amplitude of vibration normal to the bone. In those high-amplitude regions, sound is radiated with a pattern that results from the motion across the bulla.

2.4 Discussion

We observed remarkable similarities between the experiment and simulated mode shapes and corresponding frequencies, despite some notable differences between the modeled and measured TPCs, including the attachment to the skull, ligament condition, and bone geometry. We first discuss these differences in more detail. Subsequently, we consider our findings related to fin whale hearing, based on the results obtained from our experiments and simulations.

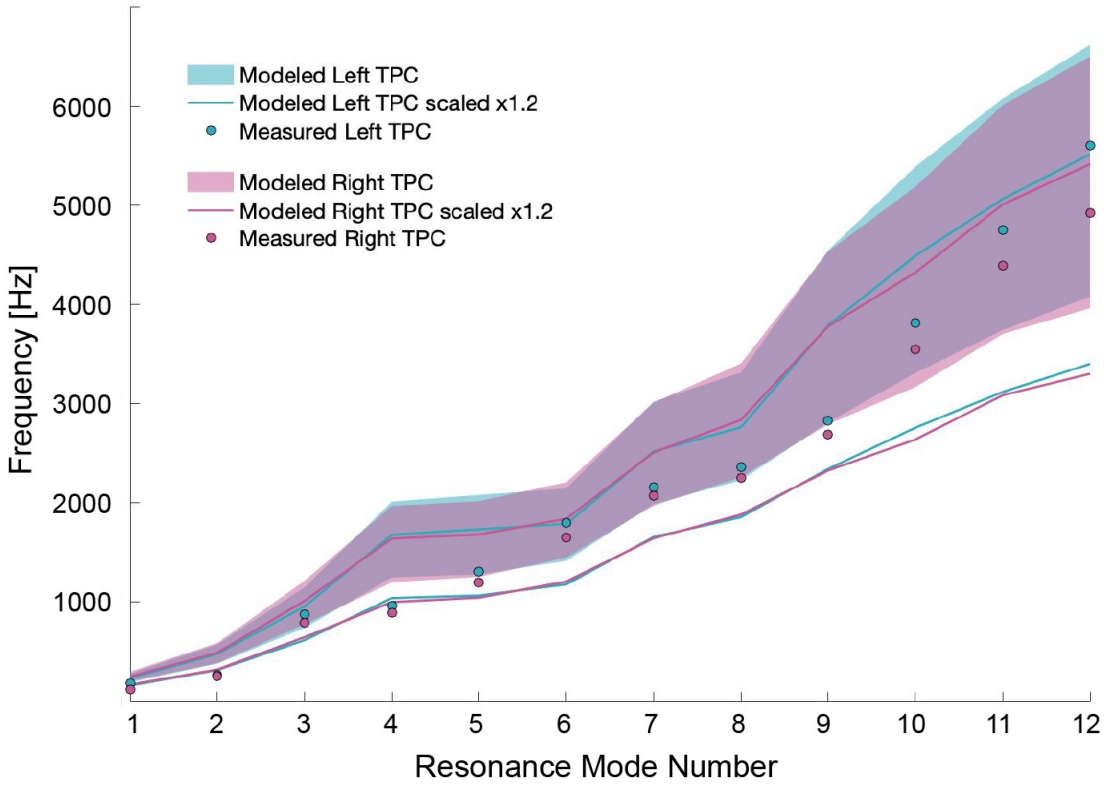

Figure 2.5. Modeled and measured resonance frequencies for modes 1-12. Resonance frequencies identified in the measured spectra are shown as blue and red dots for the left and right TPC respectively. The shaded region shows the range of resonance frequencies obtained through the model over all material properties used. The outlined region shows the range of resonance frequencies over all material parameters with the TPC uniformly scaled by a factor of 1.2 (approximate size difference between the modeled and measured TPC).

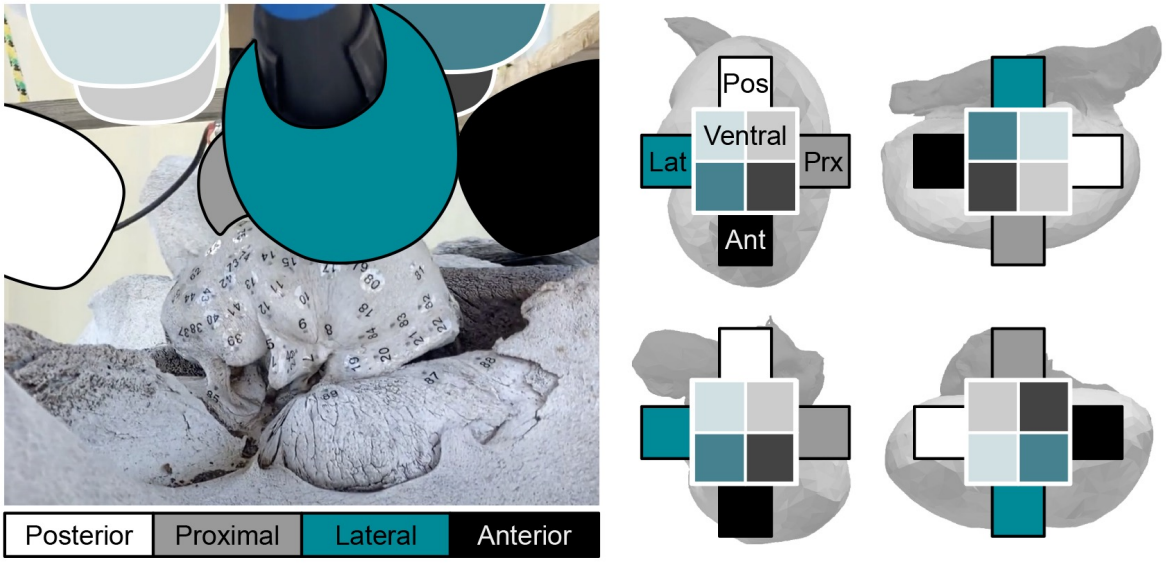

Figure 2.6. Microphone arrangement key for mode comparison plots. In the mode comparison figures (Figs 2.7, 2.8, 2.9, and supplemental), received amplitude from each microphone is shown in a 'plus' formation that mimics the arrangement of the eight microphones over each panel. This figure describes which the squares in the 'plus' correspond to which microphone for each orientation, using the Left TPC as the example. On the right, the 'plus' shape is enlarged over each TPC orientation for clarity. Boxes representing each microphone are colored to match the corresponding microphone color in the left image. In the upper left panel of the left TPC, for example: the top, right, bottom, and left of the 'plus' represents the posterior, proximal, anterior, and lateral microphones respectively. The interior squares on the 'plus' represent the ventral microphones.

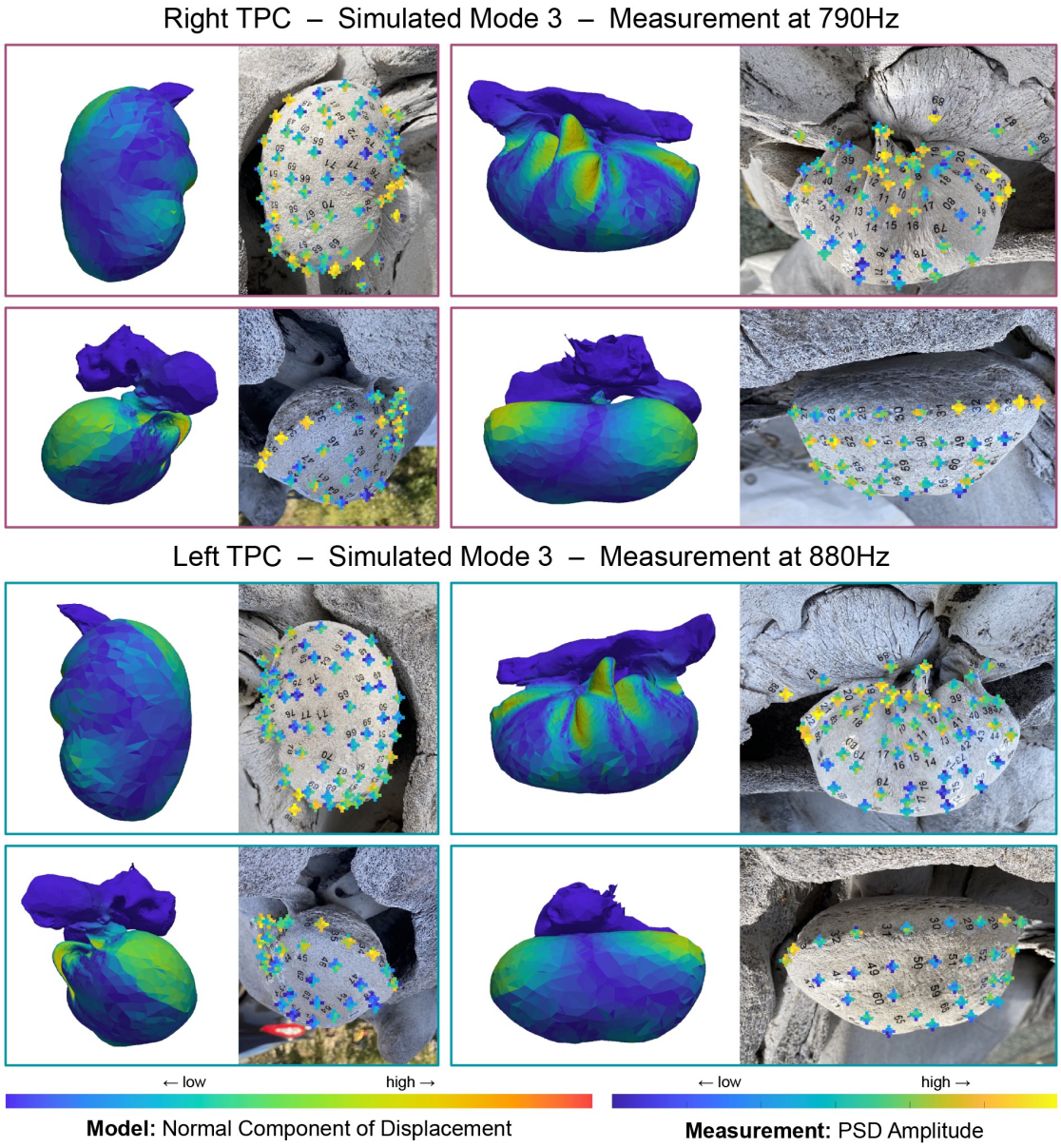

Figure 2.7. Comparison of simulated mode 3 with measurements of the left TPC at 880Hz and the right at 790Hz. Left on each panel shows the amplitude of the normal component of displacement for the simulated TPC mode 3 (stiff bone: $\rho = 2400\text{kg/m}^3, E = 25\text{GPa}$, flexible bone: $\rho = 2000\text{kg/m}^3, E = 5\text{GPa}$). Right on each panel shows an image of the TPC with received amplitudes at 880Hz or 790Hz overlaid as color. At each tap location, the received amplitude from each microphone is shown in a 'plus' formation (Fig 2.6). Both model and simulation show highest amplitudes on the posterior side of the sigmoid process, on the anterior and posterior edges of the proximal surface, and on the anterior lip. Relatively high amplitudes are registered by the anterior and posterior microphones on most tap locations. Note that the left and right TPC exhibit this pattern at different frequencies.

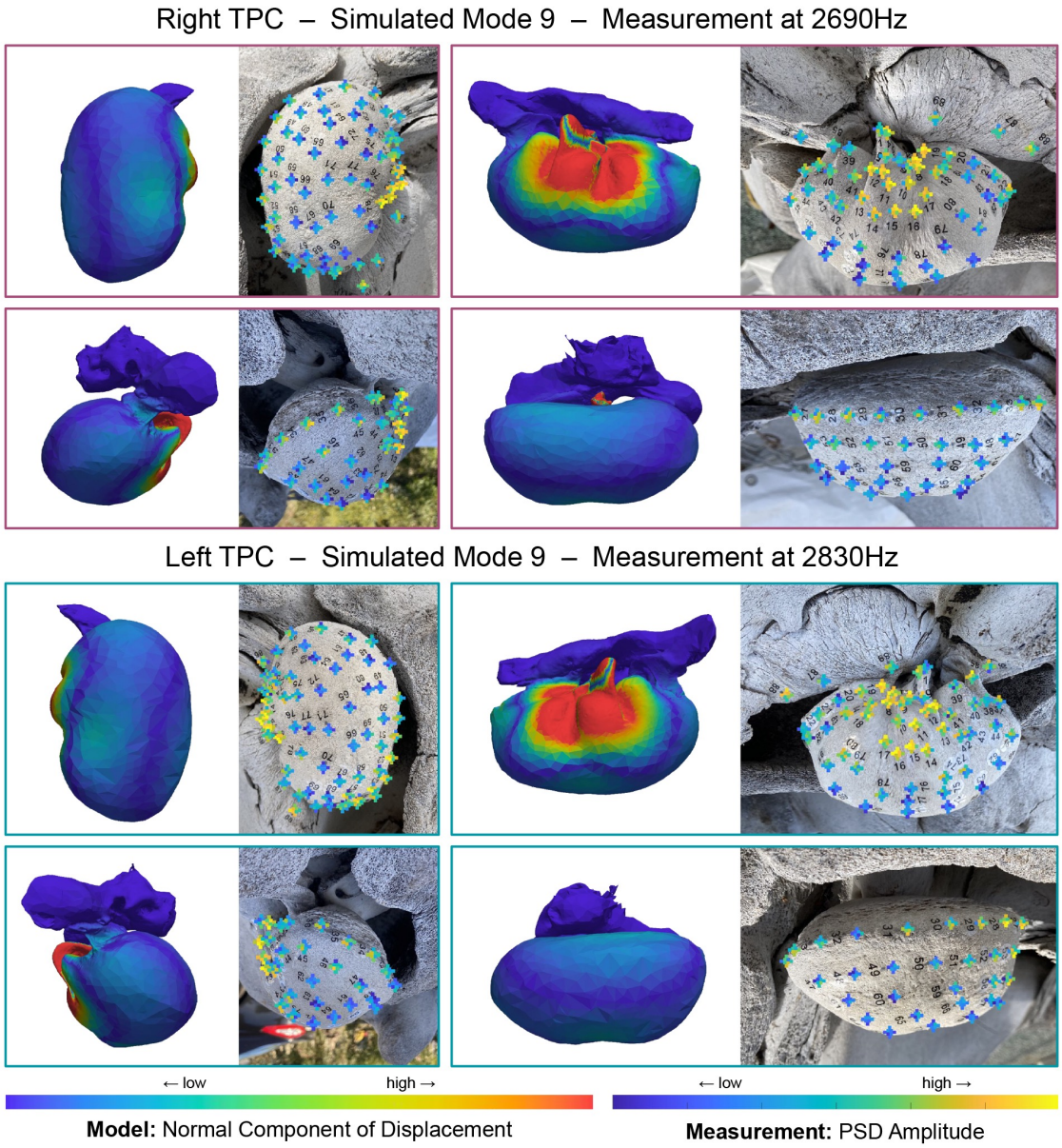

Figure 2.8. Comparison of simulated mode 9 with measurements of the left TPC at 2830Hz and the right at 2690Hz. Left on each panel shows the amplitude of the normal component of displacement for the simulated TPC mode 9 (stiff bone: $\rho = 2400\text{kg/m}^3, E = 25\text{GPa}$, flexible bone: $\rho = 2000\text{kg/m}^3, E = 5\text{GPa}$). Right on each panel shows an image of the TPC with received amplitudes at 2830Hz or 2690Hz overlaid as color. At each tap location, the received amplitude from each microphone is shown in a 'plus' formation (Fig 2.6). For this mode, taps on and very near the sigmoid process generate the highest amplitudes. Additionally, higher amplitudes are received by the lateral and anterior microphones for most tapped locations. Simulated mode 9 shows higher displacement also concentrated on the lateral side of the TPC. Both simulated and measured modes show a node along the sigmoid process. Note that the left and right TPC exhibit this pattern at different frequencies.

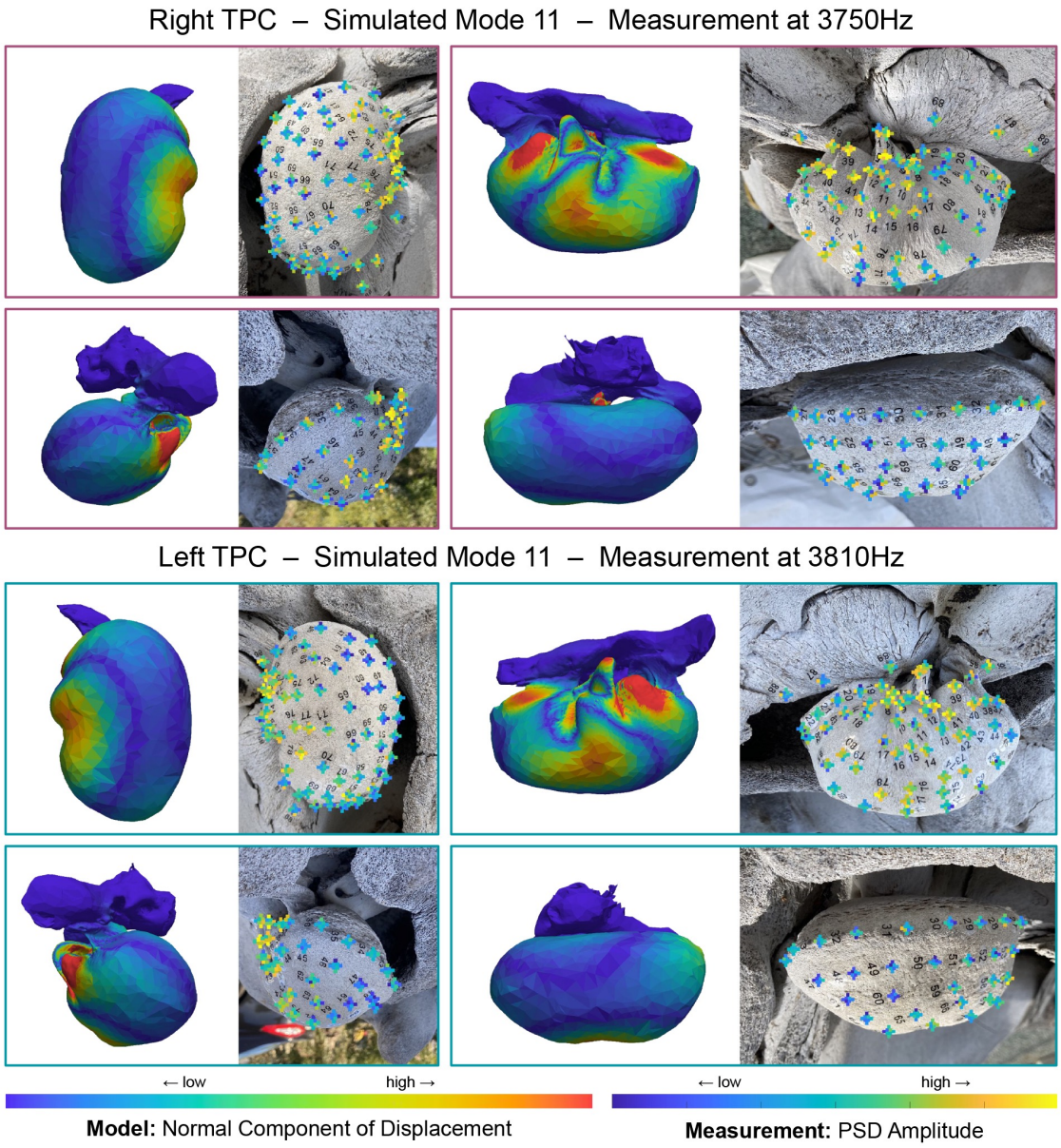

Figure 2.9. Comparison of simulated mode 11 with measurements of the left TPC at 3810Hz and the right at 3750Hz. Left on each panel shows the amplitude of the normal component of displacement for the simulated TPC mode 11 (stiff bone: $\rho = 2400\text{kg/m}^3, E = 25\text{GPa}$, flexible bone: $\rho = 2000\text{kg/m}^3, E = 5\text{GPa}$). Right on each panel shows an image of the TPC with received amplitudes at 3810Hz or 3750Hz overlaid as color. At each tap location, the received amplitude from each microphone is shown in a 'plus' formation (Fig 2.6). Measured modes show high amplitudes received from the conical process and lateral-ventral tap locations, which also show high normal-displacement in the simulations. Arching nodes can be seen on the proximal side in all cases. Note that the left and right TPC exhibit this pattern at different frequencies.

The first major difference between the modeled and measured TPC is that the latter is attached to the skull, while the model contains only the TPC. To account for this, we simulated resonance modes of the TPC with the base of the periotic bone fixed in place, as it would be attached to the skull. This simulates a firm attachment to the skull, resulting in modes of resonance relative to the skull.

Another notable difference between the modeled and the measured TPC is the inclusion of the ligaments in the ossicular chain in the former. In the experiment, the malleolar-incudal ligament was absent, so the ossicular chain was not well-connected. Consequently, we would not expect modes primarily involving the ossicular chain to be excited. Nevertheless, we found that modes involving vibration across the entire TPC were present in the simulation, regardless of whether the ossicular chain was included or not. Therefore, despite the absence of the ossicular chain's ligaments in the experiment, modes that should be present when everything is connected were still excited, providing insight into the mechanisms underlying fin whale hearing.

Another consideration is that since the TPC in the experiment was not the same one scanned for the model, there are bound to be some discrepancies between model and experiment resulting from true differences in geometry. One clear difference is in size: the length of the physical adult tympanic bulla in the experiment is at most 1.2 times that of the calf TPC in the model (Fig 2.4). Scaling-up the mesh resulted in lower resonance frequencies for the same vibration pattern, which could explain why the resonance frequencies identified in the experiment were lower than those in the model. However, a uniform scaling of the mesh cannot resolve any morphological discrepancies, and that it may overestimate bone thickness, leading to a further overestimation in frequency. It is important to consider these limitations when comparing the measured and modeled frequencies, yet Fig 2.5 shows that the measured frequencies are fairly consistent with the range of modeled frequencies obtained by varying material parameters, whether the TPC is scaled or not.

The model results depended upon the material parameters, including density and Young's modulus, as well as the mesh geometry. We examined sensitivity of the model to changes in

the Young's modulus of both hard and soft bone, as well as the density of the hard bone. The model classified the pedicles as soft bone, while the rest of the TPC, including the ossicles, was classified as hard bone.

Our results show that density changes within the range reported in the literature have little effect on the mode shape. However, increasing the density of the hard bone leads to a proportional decrease in resonant frequency for each mode, with a 4% increase in density corresponding to a 4% decrease in frequency for each mode. On the other hand, changing the Young's modulus has a larger affect on the mode shapes. As the true Young's modulus of the bone is uncertain, the range of values that we considered reasonable for the model inputs led to a wider range of possible frequencies and possible modes. The elastic moduli measured by Tubelli et al 2004 [Tubelli et al., 2014] for fin whale ossicles are broad, and may be considered an upper bound, given that bone is porous, and the nanoindentation method they used was by definition applied to the solid framework of the bone. Additionally, the skull used in the experiment had been dried for some time, and studies have shown that Young's modulus may increase for dried bone [Sedlin, 1965]. However, since the TPC bone is dense, the effect of drying is expected to be less pronounced than in other types of bone. Nonetheless, the wide range of potentially appropriate Young's moduli leads to some variation in mode shapes and frequencies.

Several modes are clearly identifiable in both the simulation and experiment, such as mode 9, shown in Fig 2.8, where higher amplitudes are concentrated in a region around the sigmoidal process and lateral furrow of the tympanic bulla. In the simulation, a "node" on the sigmoidal process (the blue strip where the normal component of displacement is almost zero) corresponds to tap locations that produce lower amplitudes. Additionally, higher amplitudes are received by the lateral and anterior microphones for most tap locations in the high-amplitude region. Simulated mode 9 exhibits more deformation on the lateral and anterior sides of the bulla. This can be seen in the displacement pattern, and is made clear in an animation of this mode, see supplementary files mode 9).

However, some modes are more difficult to distinguish, which may be due to the nature

of the experiment. The simulation shows each mode as distinct from one another, displaying how the bone would vibrate if driven at each resonance frequency alone, moving solely in its mode. In reality, the motion of the TPC is often a combination of multiple modes. Mathematically, the vibration of any object can be described as a sum of that object's normal modes of vibration. During the experiment, multiple modes are excited simultaneously, and by taking the FFT and producing the power spectrum, we are decomposing the recording into its frequency components to isolate the motion at specific frequencies. This has the effect that when we measure the recorded amplitude at frequencies between resonance modes, the spatial pattern will likely show a combination of elements from adjacent (and possibly more) resonant modes.

Notably, if two modes are close enough in frequency, it will be difficult to separate them in the data. This can be seen in the recorded spectra most clearly for frequencies between 800-1000Hz (Fig 2.3), where the left (and to a lesser degree the right) TPC produces two peaks, identified as modes 3 and 4, that nearly appear as one. If the resonance frequencies were closer, it would be challenging to resolve the difference in the experimental data, while in the simulation both modes would be shown as separate and distinct. These factors may explain some of the discrepancies between the modeled and measured modal patterns.

For instance, mode 3 (Fig 2.7) shows fairly good agreement between high-amplitude tap locations and simulated regions with high normal displacement, but one discrepancy is that the node on the proximal side of the bulla is not as pronounced in the experiment as it is in the simulation. That node is not present in simulated mode 4 (Fig 2.13, Fig 2.25), which may be contributing to the displacement pattern resolved in the experiment. This can also be seen in the radiated sound pattern recorded by the microphones. The bulla in the simulated mode is swishing anterior to posterior with a slight pivot along the aforementioned proximal node (supplementary files mode 3), so we would expect sound to radiate in the anterior and posterior directions with relatively little sound radiated proximally. The anterior and posterior microphones record high amplitudes as expected, but the proximal microphone also records relatively high amplitudes for many tap-locations. Again, this unexpected sound may be from mode 4, whose frequency peak

broadly overlaps with mode 3.

As frequency increases, vibration patterns become more complex and the modes become difficult to resolve. Mode 11 (Fig 2.9) provides an example where it is possible to identify correlations between the simulation and experiment, but the match is not as clear as that in mode 9 (Fig 2.8). Mode 11 shows high amplitudes on the conical process and lateral-ventral tap locations in both simulation and experiment, and exhibits an arching node across the proximal side. However, the high amplitudes simulated on the anterior lip are absent from the experiment. Vibrations across the bulla are complex (supplementary files mode 11), so it is more difficult to imagine what its radiation pattern should look like. Some tap locations anterior to the sigmoid process on the left TPC produce low amplitudes for the ventral microphones as may be expected by the node along the ventral side of the bulla. The radiation pattern seen by the microphones is less consistent across tap locations on the right TPC. This may in part be because modes 11 and 12 are closer in frequency for the right TPC than they are for the left.

While the modeled and measured TPCs were from different specimens, both were from fin whales with fully-developed TPCs, as the whale in the physical experiment was an adult and the CT scan was of a calf whose TPCs would have been developed precocially [Lancaster et al., 2015]. While there is natural variation between whales of the same species, we would expect substantial overlap in the frequency range that all can hear. Further, while resonances of the TPC itself may not be the same in all specimens, they should cover a similar range of frequencies to allow for communication. We identified multiple resonances between 100Hz and 6kHz in the experiment as well as in all modeled cases, with Young's modulus of the bone ranging from 5-25GPa and density ranging from 2300-2500 kg/m^3. Although higher resonances were recorded, the mode shapes became more difficult to identify in the measurements, so we do not present them here. Nevertheless, the consistency between modeled and measured mode shapes for modes under 6kHz gives us confidence in using the models to investigate the full range of fin whale hearing sensitivity. Most of the identified resonances concentrate the vibration near the sigmoidal process, driving vibrations in the ossicular chain,

and thus playing a significant role in the whale's hearing capabilities.

Moreover, the model highlights that lower frequency modes particularly involve considerable movement of the bulla swinging relative to the skull, with the pedicles acting as hinges (See mode 1 as an example, supplementary files) or exhibiting a twisting movement. Our previous work has also shown the TPC dancing on its pedicles in both mysticetes and odontocetes [Cranford et al., 2010, Cranford and Krysl, 2015]. This implies that the pedicles are a significant component of these motions that drive oscillations in the ossicular chain and are best kept intact in models of whale hearing.

One further observation that can be made from both model and measurement is that, for each mode, the resonance frequencies of the left and right TPCs are offset (Fig 2.3). Interestingly, in the measurements, the left TPC modes were found to have higher frequencies, whereas in the model, they were sometimes higher and sometimes lower. It is likely that it is not possible to build a perfectly symmetric bilateral organism, so this offset is inevitable. Asymmetry may play a role in the directionality of hearing, with both ears being sensitive to different frequencies. Structural asymmetry proves useful in resolving ambiguities in a symmetrical sound field in a number of bioacoustic examples including dolphins [Au and Moore, 1984, Ryabov, 2023], owls [Knudsen and Konishi, 1979, Schillberg et al., 2020], and some insects [Römer, 2020]. Moreover, this characteristic asymmetry likely contributes to improving hearing sensitivity across the range of frequencies that the whales can hear, as each TPC will be more sensitive to frequencies near its resonance modes, so it will be more sensitive at frequencies for which the other is less sensitive.

2.5 Conclusion

We demonstrate that the natural modes of vibration of the fin whale tympanoperiotic complex (TPC) involve swinging or twisting on the suspensory pedicles, with many vibration modes concentrating energy at the sigmoidal process and therefore the malleus and the ossicular

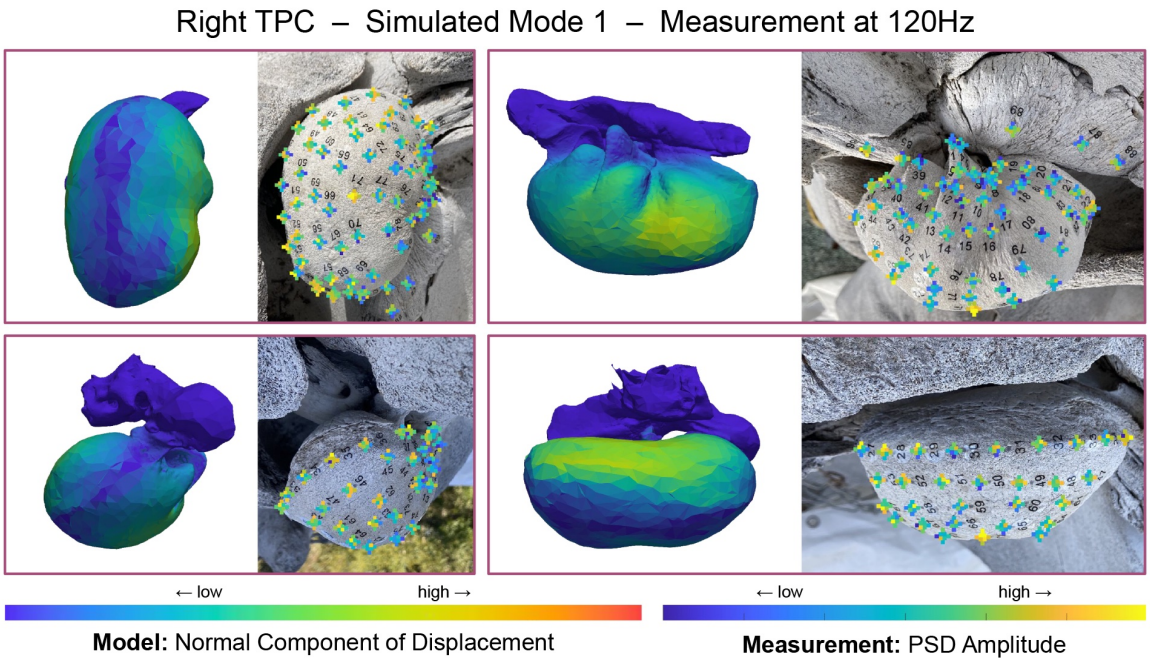

Figure 2.10. Comparison of simulated mode 1 with measurements of the right TPC at 120Hz. Left on each panel shows the amplitude of the normal component of displacement for the simulated TPC mode (stiff bone: $\rho = 2400\text{kg/m}^3, E = 25\text{GPa}$, flexible bone: $\rho = 2000\text{kg/m}^3, E = 5\text{GPa}$). Right on each panel shows an image of the TPC with received amplitudes overlaid as color

chain. Resonance frequencies range from 100Hz to beyond 6kHz, indicating that TPC resonance contributes to hearing sensitivity in that range. Our findings reveal that the resonance frequencies of the left and right TPC are offset, providing a potential mechanism for improved hearing at a range of frequencies as well as a mechanism for directionality in sound perception. Furthermore, our model results are in agreement with the experimental results, validating the modeling techniques that have been successfully employed for odontocetes and suggesting their applicability for mysticetes. Since we are dealing with a complex and integral part of the mysticete hearing mechanism, this should build confidence in future work using the models of entire skull vibrations.

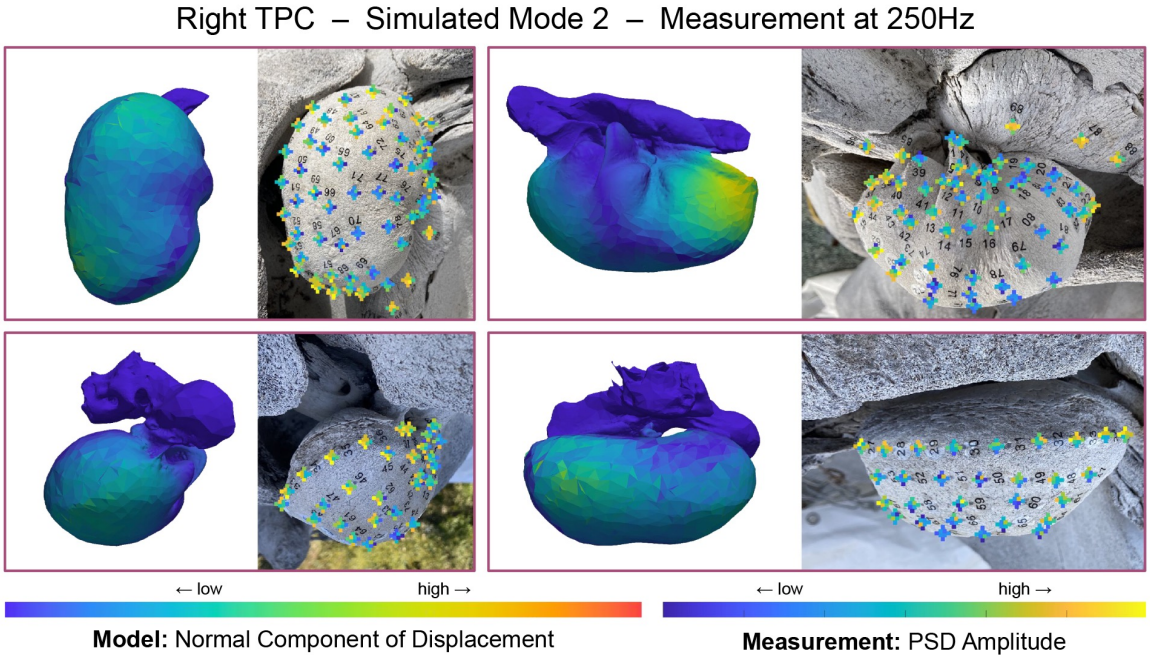

Figure 2.11. Comparison of simulated mode 2 with measurements of the right TPC at 250Hz. Left on each panel shows the amplitude of the normal component of displacement for the simulated TPC mode (stiff bone: $\rho = 2400\text{kg/m}^3, E = 25\text{GPa}$, flexible bone: $\rho = 2000\text{kg/m}^3, E = 5\text{GPa}$). Right on each panel shows an image of the TPC with received amplitudes overlaid as color

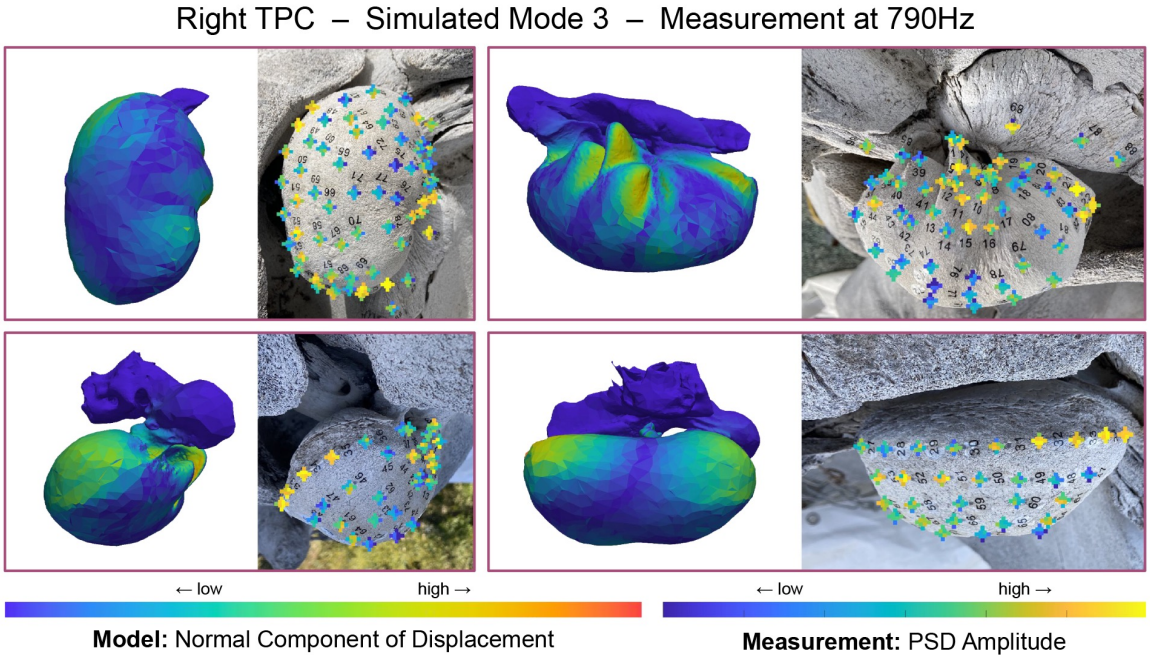

Figure 2.12. Comparison of simulated mode 3 with measurements of the right TPC at 790Hz. Left on each panel shows the amplitude of the normal component of displacement for the simulated TPC mode (stiff bone: $\rho = 2400\text{kg/m}^3, E = 25\text{GPa}$, flexible bone: $\rho = 2000\text{kg/m}^3, E = 5\text{GPa}$). Right on each panel shows an image of the TPC with received amplitudes overlaid as color

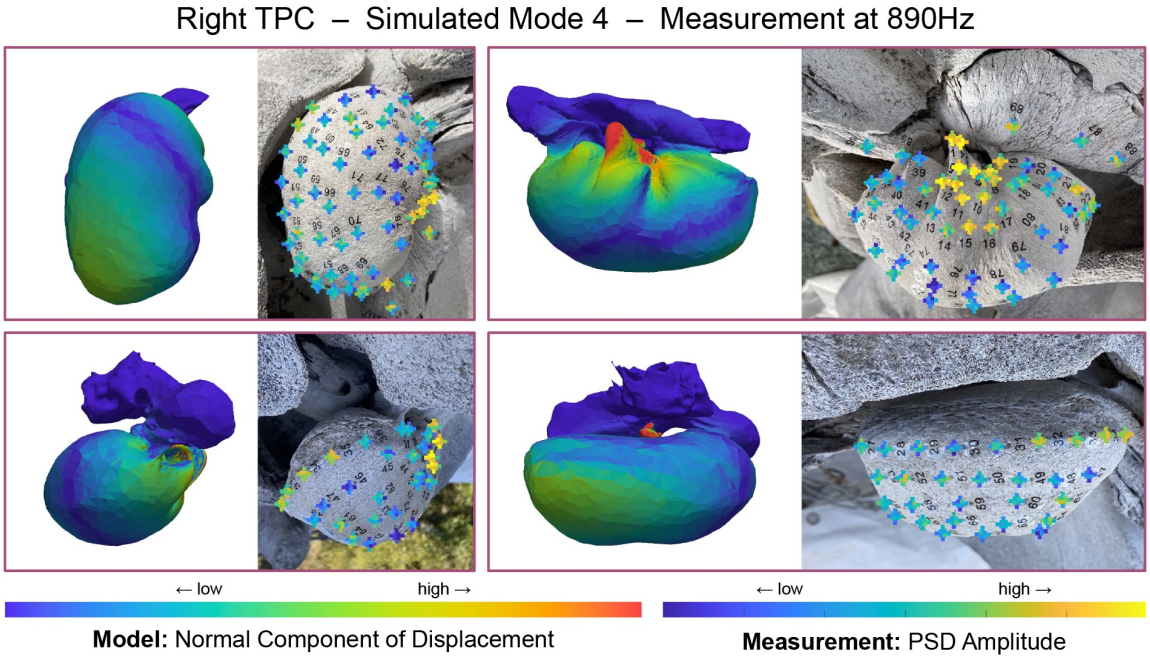

Figure 2.13. Comparison of simulated mode 4 with measurements of the right TPC at 890Hz. Left on each panel shows the amplitude of the normal component of displacement for the simulated TPC mode (stiff bone: $\rho = 2400\text{kg/m}^3, E = 25\text{GPa}$, flexible bone: $\rho = 2000\text{kg/m}^3, E = 5\text{GPa}$). Right on each panel shows an image of the TPC with received amplitudes overlaid as color

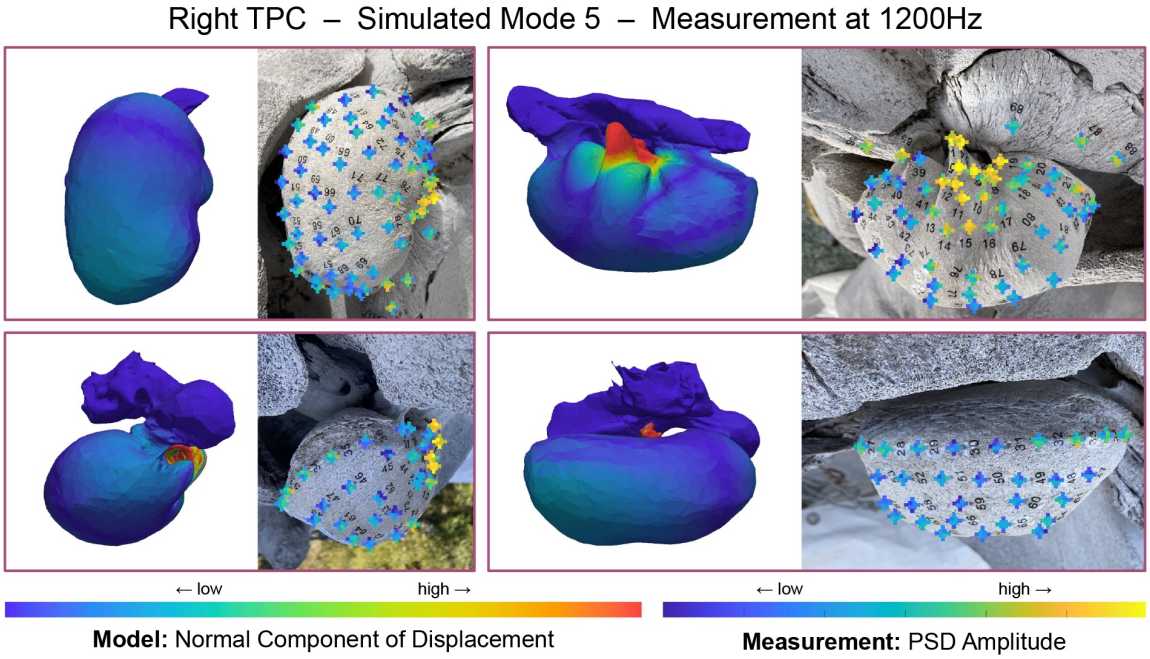

Figure 2.14. Comparison of simulated mode 5 with measurements of the right TPC at 1200Hz. Left on each panel shows the amplitude of the normal component of displacement for the simulated TPC mode (stiff bone: $\rho = 2400\text{kg/m}^3, E = 25\text{GPa}$, flexible bone: $\rho = 2000\text{kg/m}^3, E = 5\text{GPa}$). Right on each panel shows an image of the TPC with received amplitudes overlaid as color

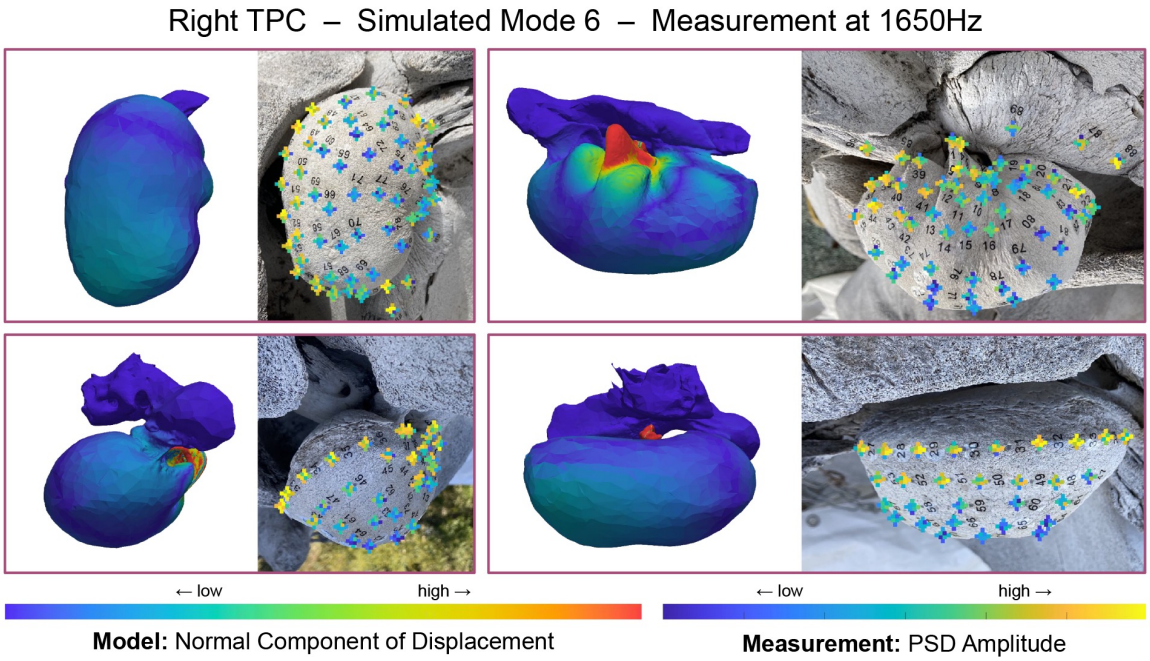

Figure 2.15. Comparison of simulated mode 6 with measurements of the right TPC at 1650Hz. Left on each panel shows the amplitude of the normal component of displacement for the simulated TPC mode (stiff bone: $\rho = 2400\text{kg/m}^3, E = 25\text{GPa}$, flexible bone: $\rho = 2000\text{kg/m}^3, E = 5\text{GPa}$). Right on each panel shows an image of the TPC with received amplitudes overlaid as color

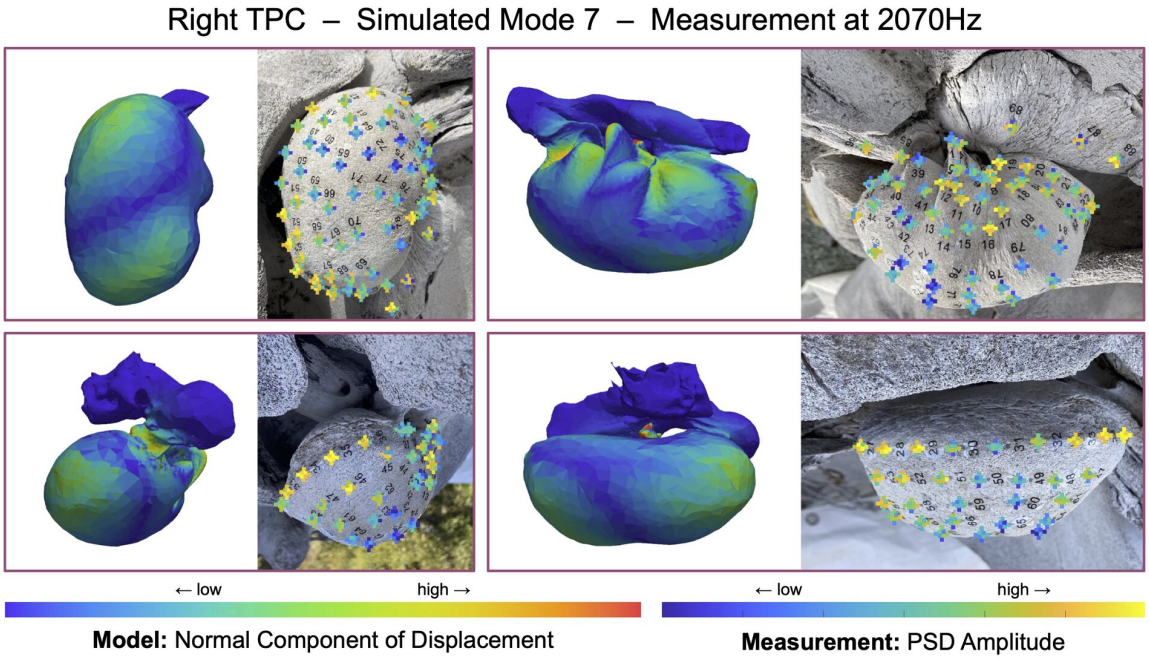

Figure 2.16. Comparison of simulated mode 7 with measurements of the right TPC at 2070Hz. Left on each panel shows the amplitude of the normal component of displacement for the simulated TPC mode (stiff bone: $\rho = 2400\text{kg/m}^3, E = 25\text{GPa}$, flexible bone: $\rho = 2000\text{kg/m}^3, E = 5\text{GPa}$). Right on each panel shows an image of the TPC with received amplitudes overlaid as color

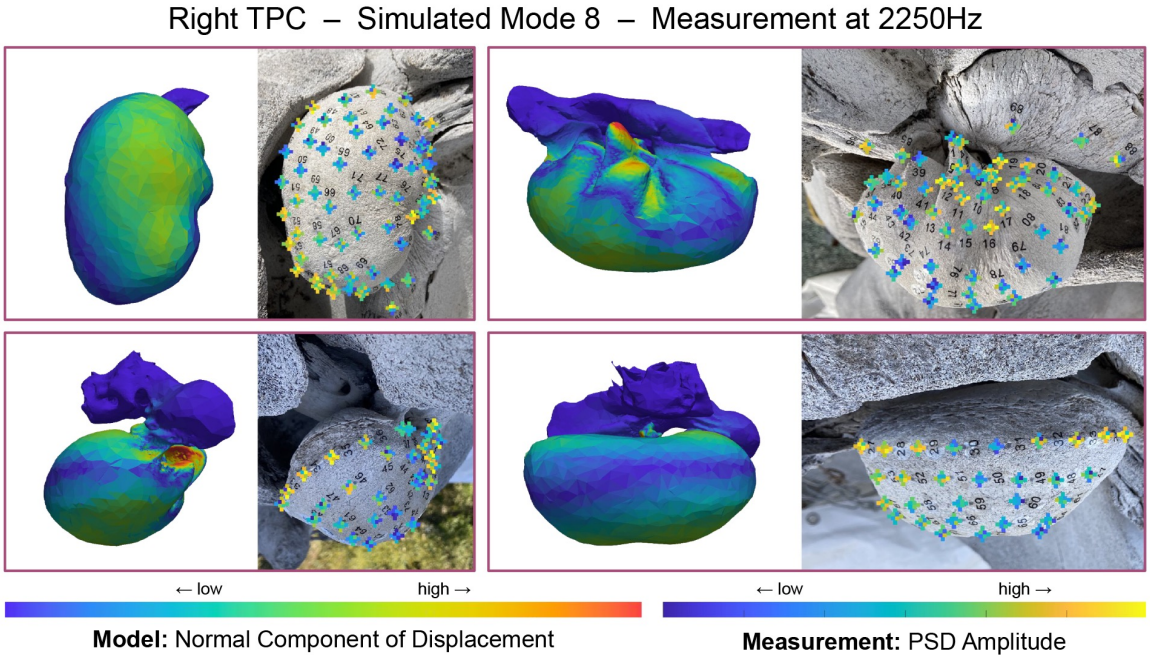

Figure 2.17. Comparison of simulated mode 8 with measurements of the right TPC at 2250Hz. Left on each panel shows the amplitude of the normal component of displacement for the simulated TPC mode (stiff bone: $\rho = 2400\text{kg/m}^3, E = 25\text{GPa}$, flexible bone: $\rho = 2000\text{kg/m}^3, E = 5\text{GPa}$). Right on each panel shows an image of the TPC with received amplitudes overlaid as color

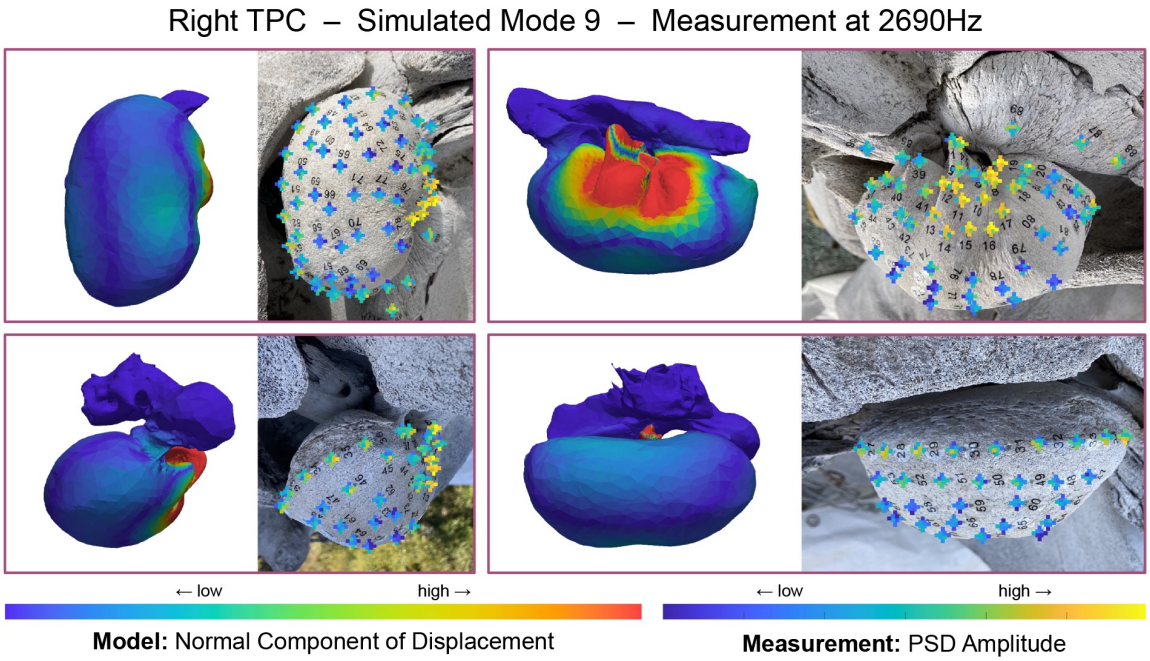

Figure 2.18. Comparison of simulated mode 9 with measurements of the right TPC at 2690Hz. Left on each panel shows the amplitude of the normal component of displacement for the simulated TPC mode (stiff bone: $\rho = 2400\text{kg/m}^3, E = 25\text{GPa}$, flexible bone: $\rho = 2000\text{kg/m}^3, E = 5\text{GPa}$). Right on each panel shows an image of the TPC with received amplitudes overlaid as color

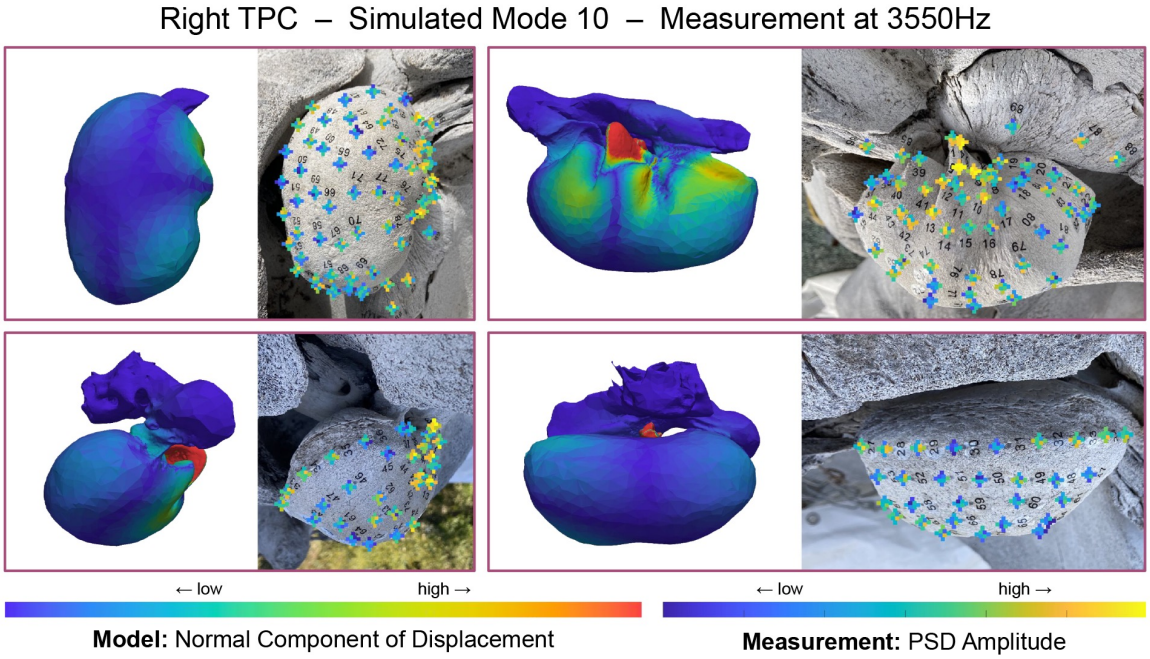

Figure 2.19. Comparison of simulated mode 10 with measurements of the right TPC at 3550Hz. Left on each panel shows the amplitude of the normal component of displacement for the simulated TPC mode (stiff bone: $\rho = 2400\text{kg/m}^3, E = 25\text{GPa}$, flexible bone: $\rho = 2000\text{kg/m}^3, E = 5\text{GPa}$). Right on each panel shows an image of the TPC with received amplitudes overlaid as color

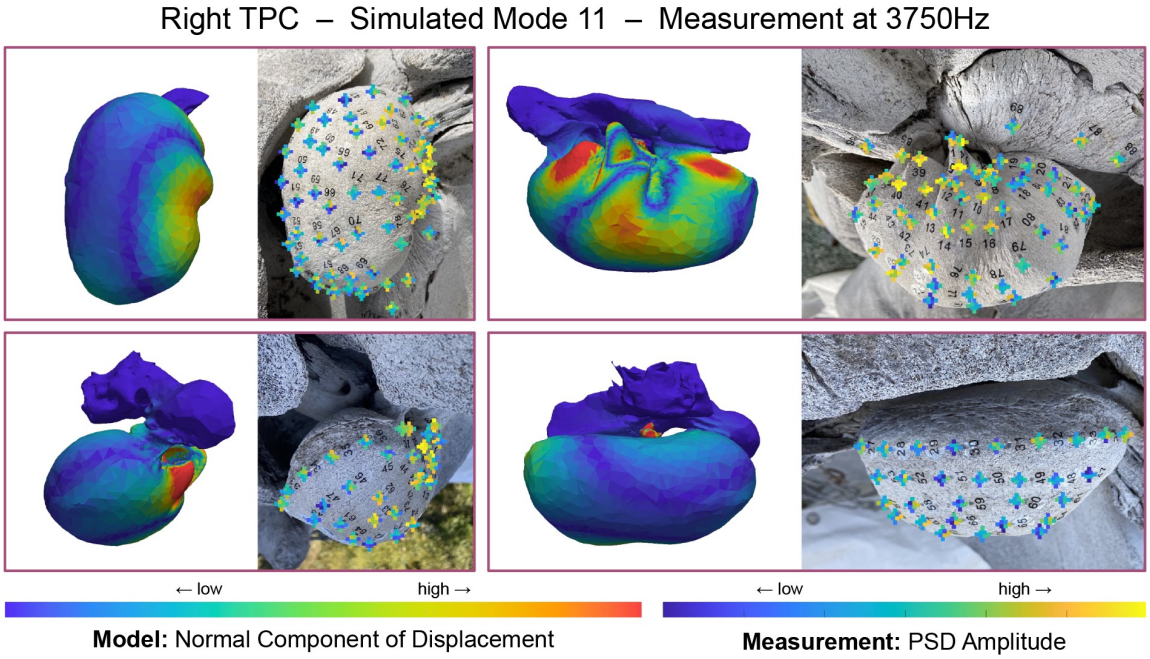

Figure 2.20. Comparison of simulated mode 11 with measurements of the right TPC at 3750Hz. Left on each panel shows the amplitude of the normal component of displacement for the simulated TPC mode (stiff bone: $\rho = 2400\text{kg/m}^3, E = 25\text{GPa}$, flexible bone: $\rho = 2000\text{kg/m}^3, E = 5\text{GPa}$). Right on each panel shows an image of the TPC with received amplitudes overlaid as color

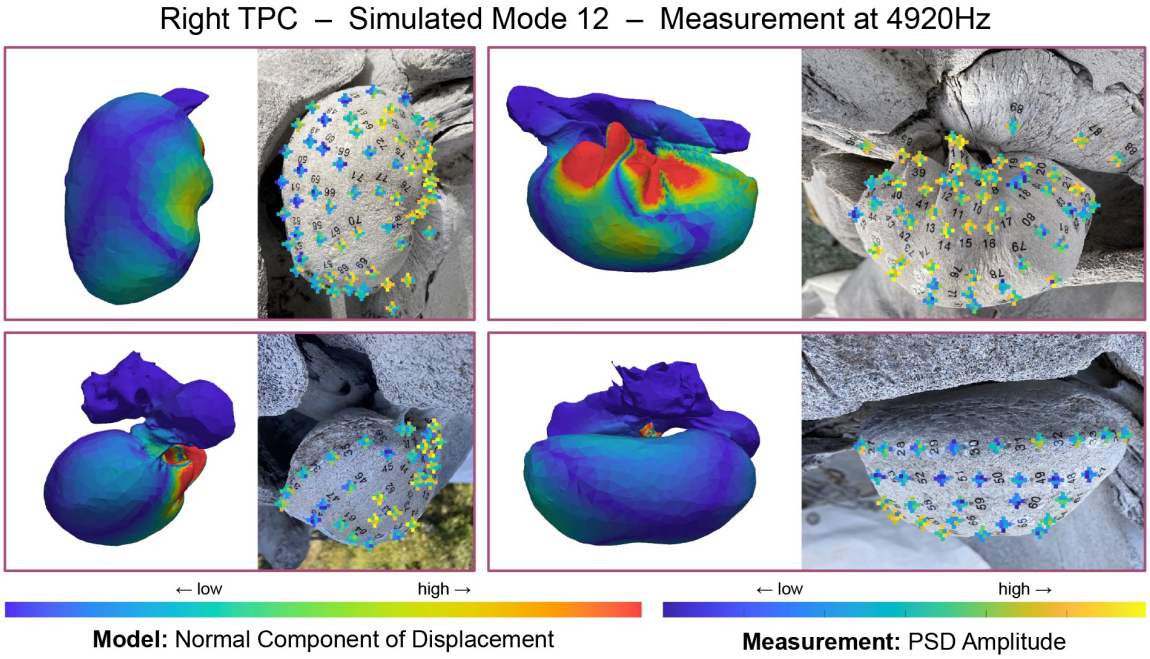

Figure 2.21. Comparison of simulated mode 12 with measurements of the right TPC at 4920Hz. Left on each panel shows the amplitude of the normal component of displacement for the simulated TPC mode (stiff bone: $\rho = 2400\text{kg/m}^3, E = 25\text{GPa}$, flexible bone: $\rho = 2000\text{kg/m}^3, E = 5\text{GPa}$). Right on each panel shows an image of the TPC with received amplitudes overlaid as color

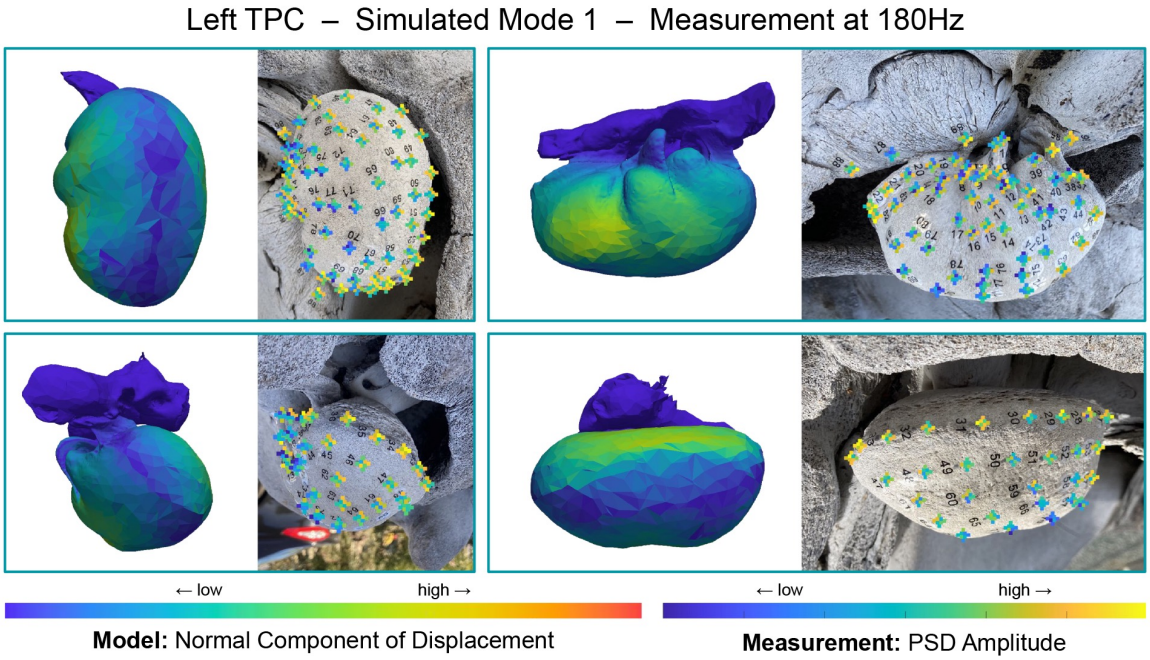

Figure 2.22. Comparison of simulated mode 1 with measurements of the left TPC at 180Hz. Left on each panel shows the amplitude of the normal component of displacement for the simulated TPC mode (stiff bone: $\rho = 2400\text{kg/m}^3, E = 25\text{GPa}$, flexible bone: $\rho = 2000\text{kg/m}^3, E = 5\text{GPa}$). Right on each panel shows an image of the TPC with received amplitudes overlaid as color

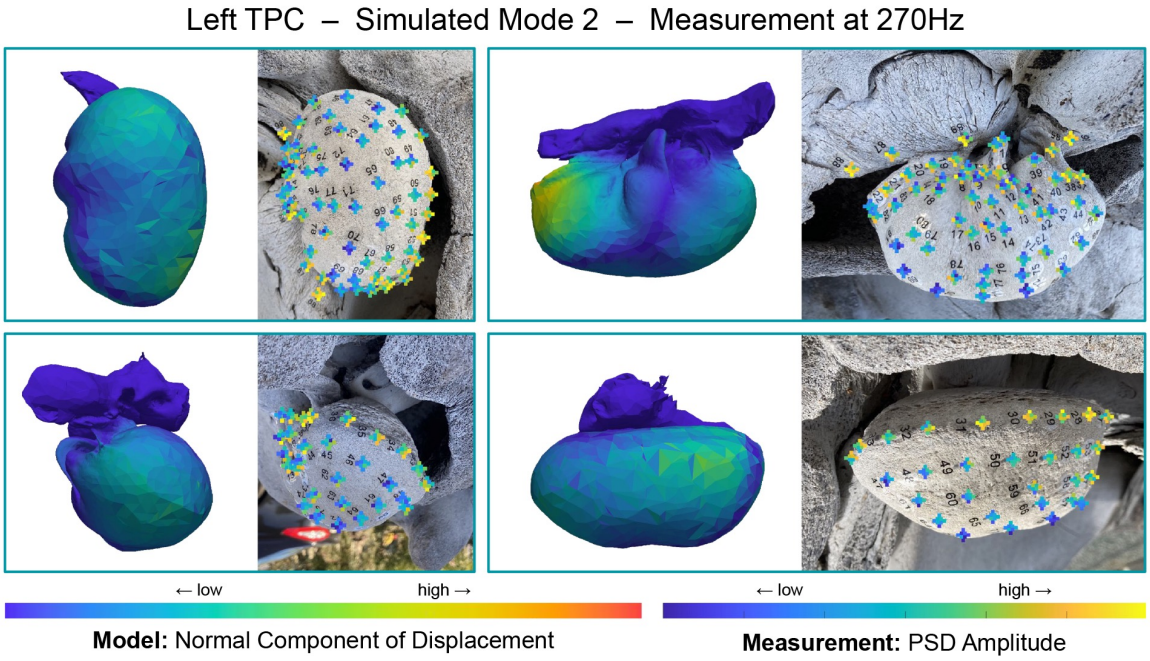

Figure 2.23. Comparison of simulated mode 2 with measurements of the left TPC at 270Hz. Left on each panel shows the amplitude of the normal component of displacement for the simulated TPC mode (stiff bone: $\rho = 2400\text{kg/m}^3, E = 25\text{GPa}$, flexible bone: $\rho = 2000\text{kg/m}^3, E = 5\text{GPa}$). Right on each panel shows an image of the TPC with received amplitudes overlaid as color

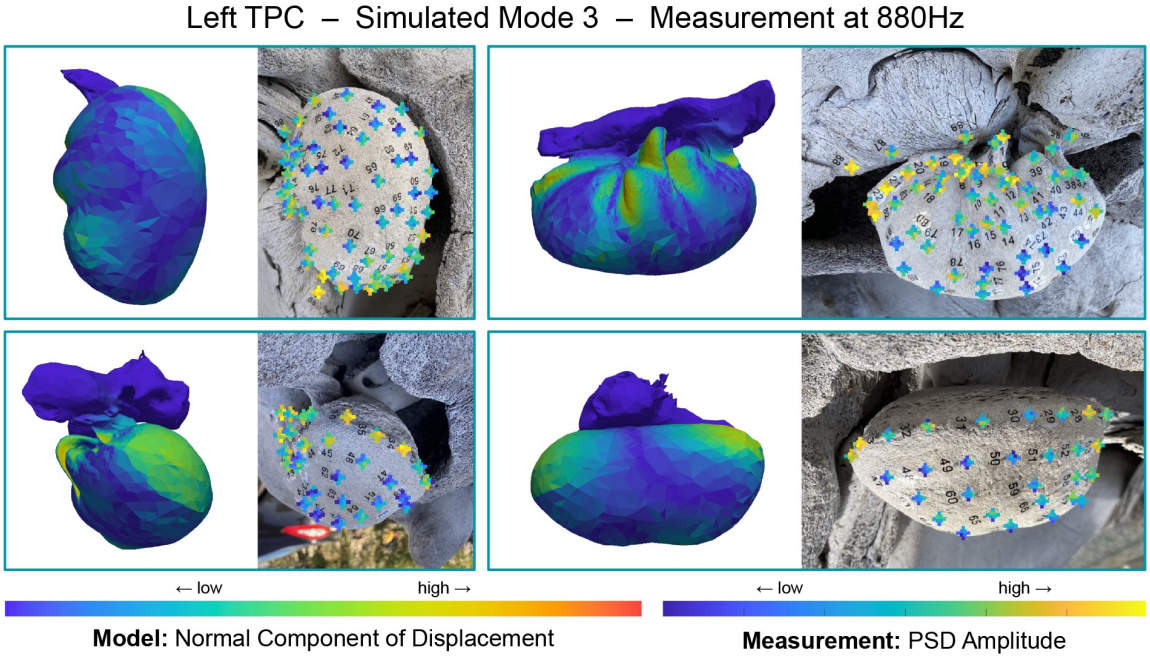

Figure 2.24. Comparison of simulated mode 3 with measurements of the left TPC at 880Hz. Left on each panel shows the amplitude of the normal component of displacement for the simulated TPC mode (stiff bone: $\rho = 2400\text{kg/m}^3, E = 25\text{GPa}$, flexible bone: $\rho = 2000\text{kg/m}^3, E = 5\text{GPa}$). Right on each panel shows an image of the TPC with received amplitudes overlaid as color

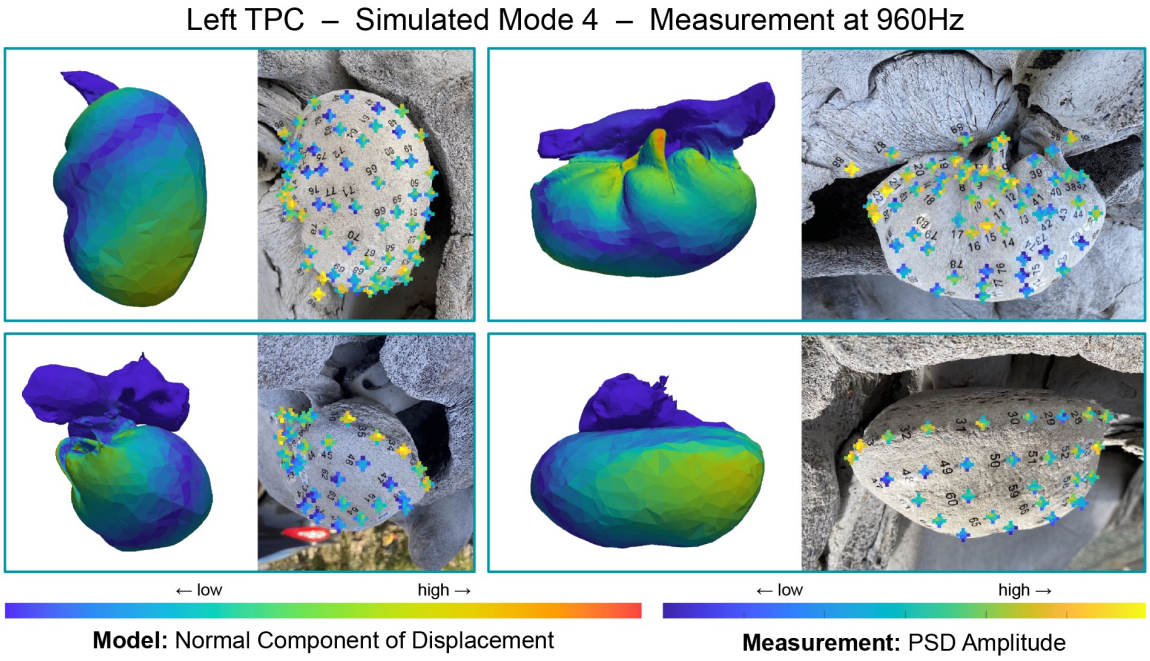

Figure 2.25. Comparison of simulated mode 4 with measurements of the left TPC at 960Hz. Left on each panel shows the amplitude of the normal component of displacement for the simulated TPC mode (stiff bone: $\rho = 2400\text{kg/m}^3, E = 25\text{GPa}$, flexible bone: $\rho = 2000\text{kg/m}^3, E = 5\text{GPa}$). Right on each panel shows an image of the TPC with received amplitudes overlaid as color

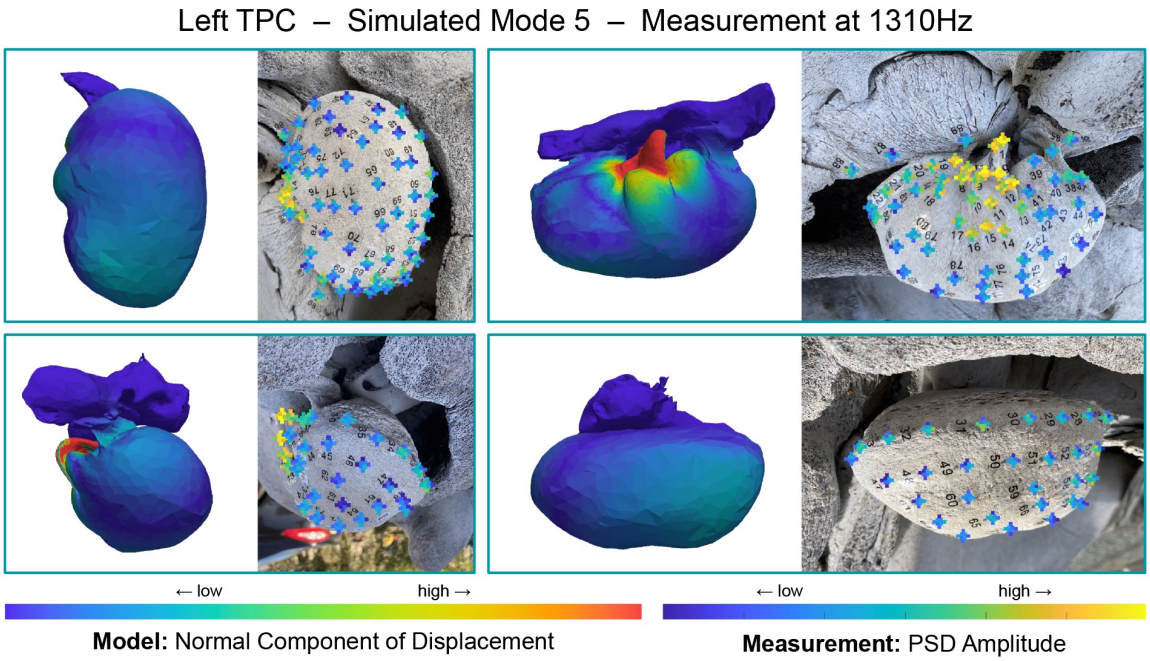

Figure 2.26. Comparison of simulated mode 5 with measurements of the left TPC at 1310Hz. Left on each panel shows the amplitude of the normal component of displacement for the simulated TPC mode (stiff bone: $\rho = 2400\text{kg/m}^3, E = 25\text{GPa}$, flexible bone: $\rho = 2000\text{kg/m}^3, E = 5\text{GPa}$). Right on each panel shows an image of the TPC with received amplitudes overlaid as color

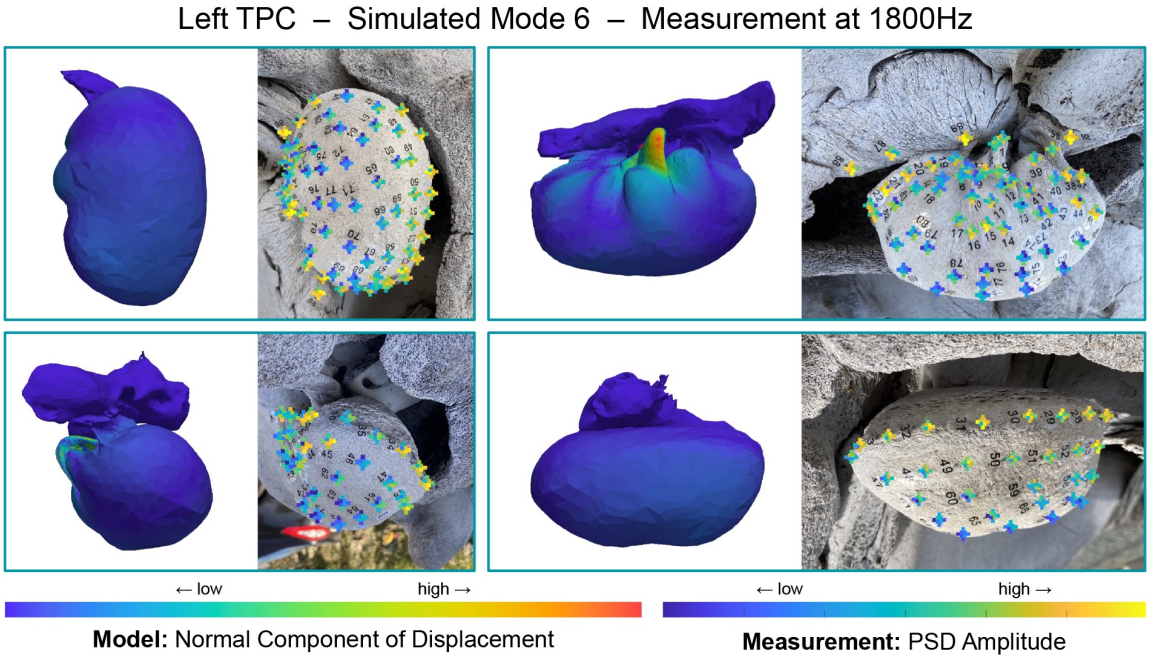

Figure 2.27. Comparison of simulated mode 6 with measurements of the left TPC at 1800Hz. Left on each panel shows the amplitude of the normal component of displacement for the simulated TPC mode (stiff bone: $\rho = 2400\text{kg/m}^3, E = 25\text{GPa}$, flexible bone: $\rho = 2000\text{kg/m}^3, E = 5\text{GPa}$). Right on each panel shows an image of the TPC with received amplitudes overlaid as color

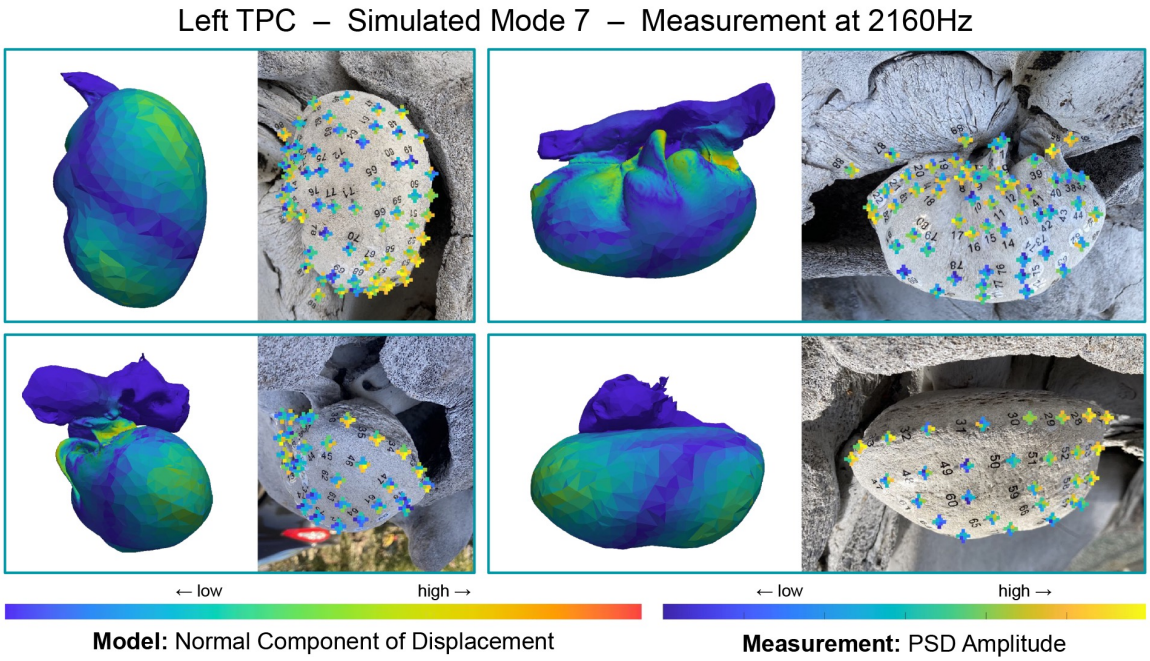

Figure 2.28. Comparison of simulated mode 7 with measurements of the left TPC at 2160Hz. Left on each panel shows the amplitude of the normal component of displacement for the simulated TPC mode (stiff bone: $\rho = 2400\text{kg/m}^3, E = 25\text{GPa}$, flexible bone: $\rho = 2000\text{kg/m}^3, E = 5\text{GPa}$). Right on each panel shows an image of the TPC with received amplitudes overlaid as color

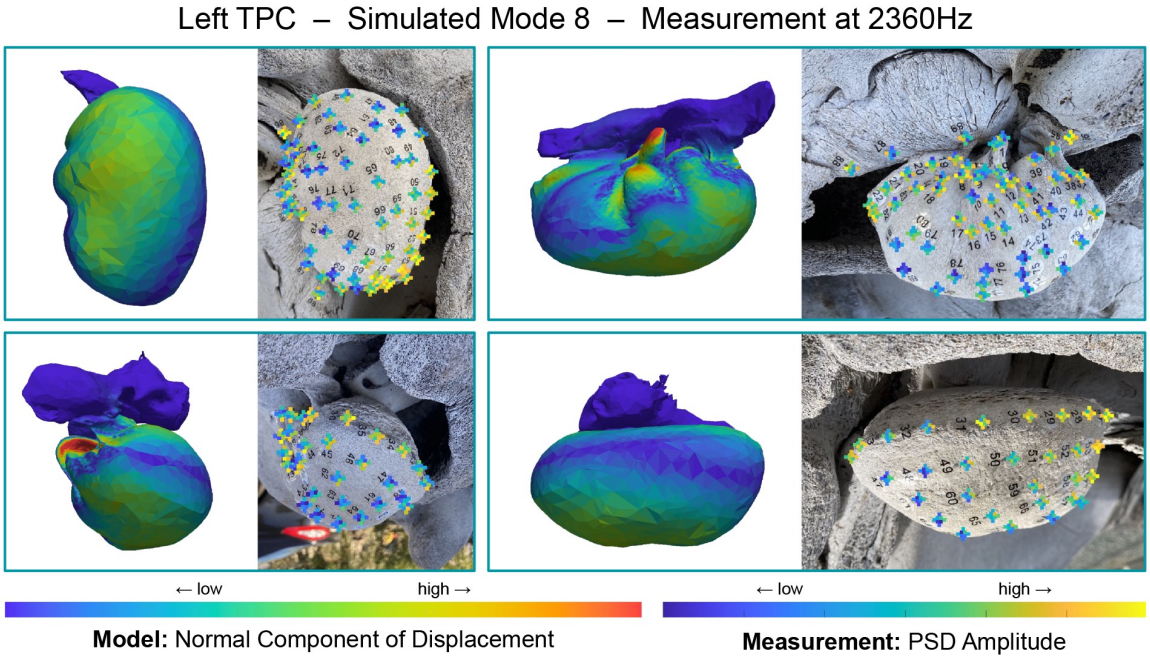

Figure 2.29. Comparison of simulated mode 8 with measurements of the left TPC at 2360Hz. Left on each panel shows the amplitude of the normal component of displacement for the simulated TPC mode (stiff bone: $\rho = 2400\text{kg/m}^3, E = 25\text{GPa}$, flexible bone: $\rho = 2000\text{kg/m}^3, E = 5\text{GPa}$). Right on each panel shows an image of the TPC with received amplitudes overlaid as color

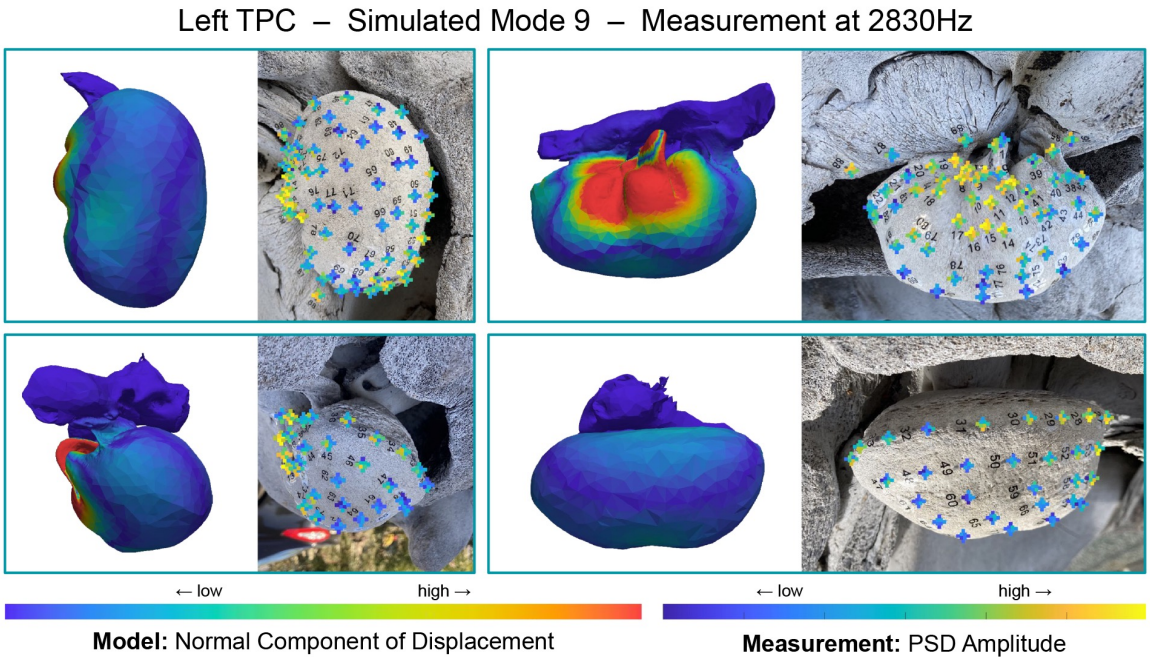

Figure 2.30. Comparison of simulated mode 9 with measurements of the left TPC at 2830Hz. Left on each panel shows the amplitude of the normal component of displacement for the simulated TPC mode (stiff bone: $\rho = 2400\text{kg/m}^3, E = 25\text{GPa}$, flexible bone: $\rho = 2000\text{kg/m}^3, E = 5\text{GPa}$). Right on each panel shows an image of the TPC with received amplitudes overlaid as color

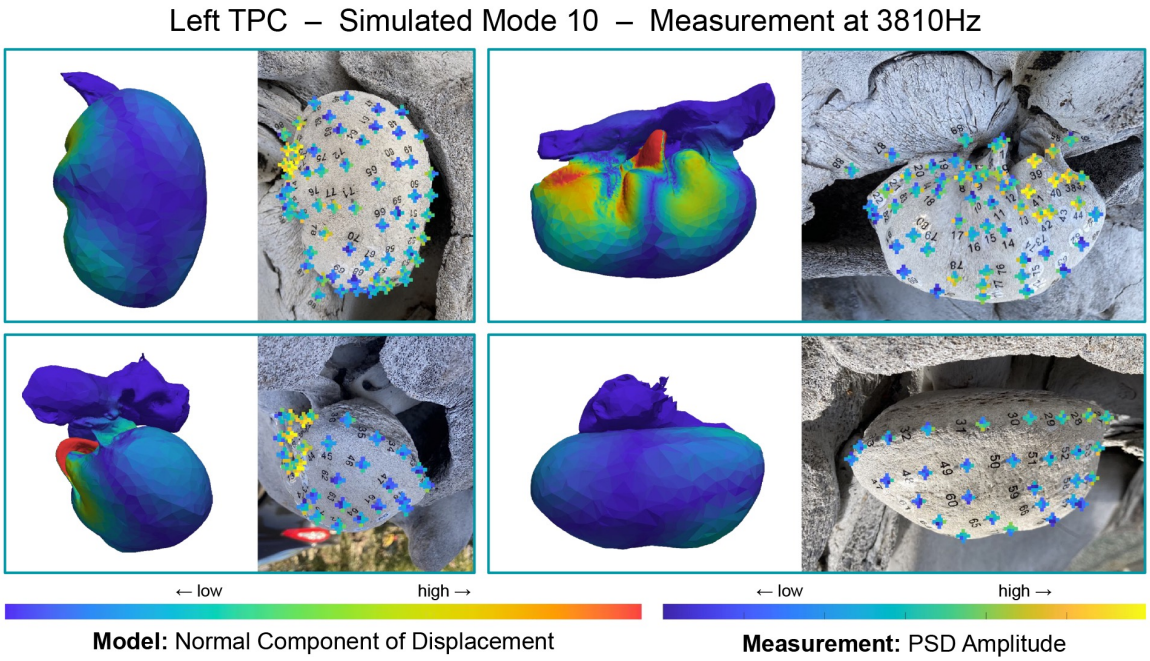

Figure 2.31. Comparison of simulated mode 10 with measurements of the left TPC at 3810Hz. Left on each panel shows the amplitude of the normal component of displacement for the simulated TPC mode (stiff bone: $\rho = 2400\text{kg/m}^3, E = 25\text{GPa}$, flexible bone: $\rho = 2000\text{kg/m}^3, E = 5\text{GPa}$). Right on each panel shows an image of the TPC with received amplitudes overlaid as color

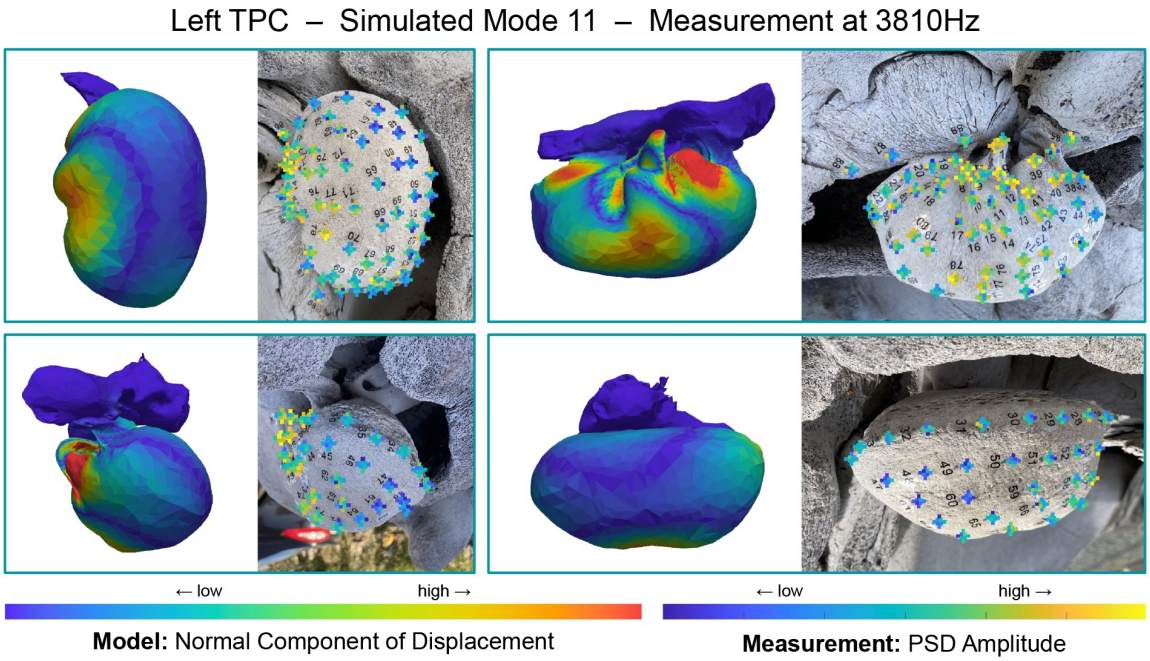

Figure 2.32. Comparison of simulated mode 11 with measurements of the left TPC at 3810Hz. Left on each panel shows the amplitude of the normal component of displacement for the simulated TPC mode (stiff bone: $\rho = 2400\text{kg/m}^3, E = 25\text{GPa}$, flexible bone: $\rho = 2000\text{kg/m}^3, E = 5\text{GPa}$). Right on each panel shows an image of the TPC with received amplitudes overlaid as color

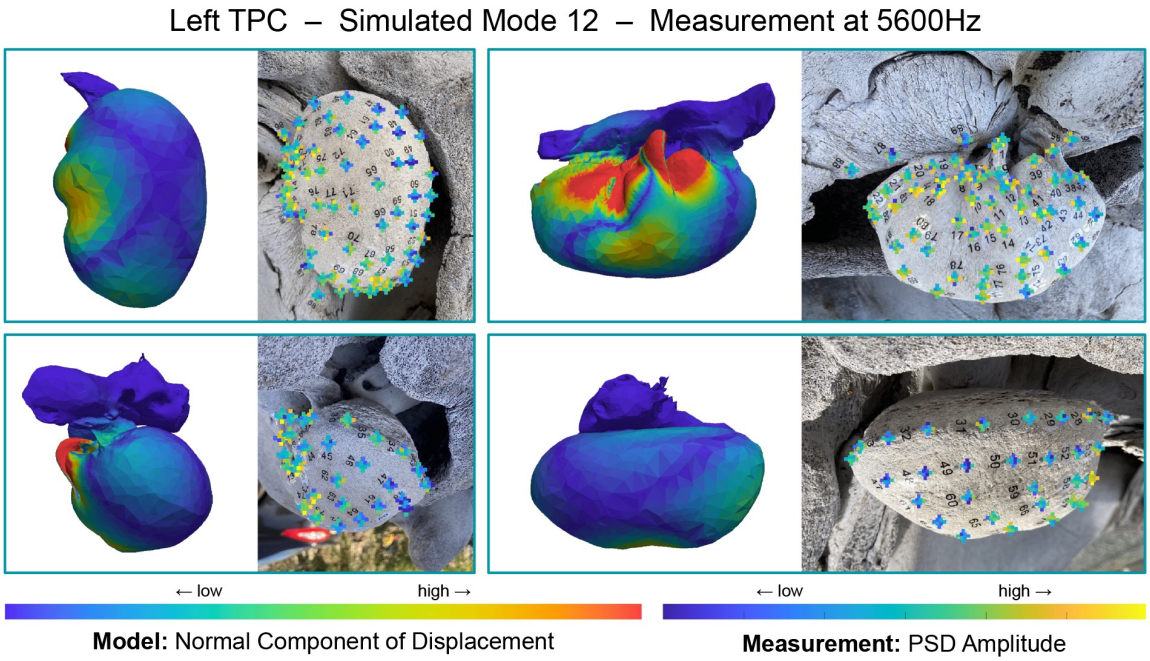

Figure 2.33. Comparison of simulated mode 12 with measurements of the left TPC at 5600Hz. Left on each panel shows the amplitude of the normal component of displacement for the simulated TPC mode (stiff bone: $\rho = 2400\text{kg/m}^3, E = 25\text{GPa}$, flexible bone: $\rho = 2000\text{kg/m}^3, E = 5\text{GPa}$). Right on each panel shows an image of the TPC with received amplitudes overlaid as color

Supporting information

Mode1_RightTPC_Animation.mp4

Simulated Mode 1 of the right TPC. Animation of simulated TPC mode colored by the normal component of displacement (stiff bone: $\rho = 2400\text{kg/m}^3, E = 25\text{GPa}$, flexible bone: $\rho = 2000\text{kg/m}^3, E = 5\text{GPa}$).

Mode1_LeftTPC_Animation.mp4

Simulated Mode 1 of the left TPC. Animation of simulated TPC mode colored by the normal component of displacement (stiff bone: $\rho = 2400\text{kg/m}^3, E = 25\text{GPa}$, flexible bone: $\rho = 2000\text{kg/m}^3, E = 5\text{GPa}$).

Mode3_RightTPC_Animation.mp4

Simulated Mode 3 of the right TPC. Animation of simulated TPC mode colored by the normal component of displacement (stiff bone: $\rho = 2400\text{kg/m}^3, E = 25\text{GPa}$, flexible bone: $\rho = 2000\text{kg/m}^3, E = 5\text{GPa}$).

Mode3_LeftTPC_Animation.mp4

Simulated Mode 3 of the left TPC. Animation of simulated TPC mode colored by the normal component of displacement (stiff bone: $\rho = 2400\text{kg/m}^3, E = 25\text{GPa}$, flexible bone: $\rho = 2000\text{kg/m}^3, E = 5\text{GPa}$).

Mode3_RightTPC_Animation.mp4

Simulated Mode 9 of the right TPC. Animation of simulated TPC mode colored by the normal component of displacement (stiff bone: $\rho = 2400\text{kg/m}^3, E = 25\text{GPa}$, flexible bone: $\rho = 2000\text{kg/m}^3, E = 5\text{GPa}$).

Mode9_LeftTPC_Animation.mp4

Simulated Mode 9 of the left TPC. Animation of simulated TPC mode colored by the normal component of displacement (stiff bone: $\rho = 2400\text{kg/m}^3, E = 25\text{GPa}$, flexible bone: $\rho = 2000\text{kg/m}^3, E = 5\text{GPa}$).

Mode11_RightTPC_Animation.mp4

Simulated Mode 11 of the right TPC. Animation of simulated TPC mode colored by the normal component of displacement (stiff bone: $\rho = 2400\text{kg/m}^3, E = 25\text{GPa}$, flexible bone: $\rho = 2000\text{kg/m}^3, E = 5\text{GPa}$).

Mode11_LeftTPC_Animation.mp4

Simulated Mode 11 of the left TPC. Animation of simulated TPC mode colored by the normal component of displacement (stiff bone: $\rho = 2400\text{kg/m}^3, E = 25\text{GPa}$, flexible bone: $\rho = 2000\text{kg/m}^3, E = 5\text{GPa}$).

2.6 Acknowledgements

We thank the UC San Diego, Scripps Graduate Department for support of MAM. In addition we acknowledge support from the Office of Naval Research Marine Mammal Research Program under the guidance of Dr. Michael J. Weise (Award Number: N00014-19-1-2682).

Chapter 2, in full, has been submitted for publication of the material as it may appear in Resonance of the tympanoperiotic complex of fin whales with implications for their low frequency hearing 2023. Morris, Margaret; Krysl, Petr; Hildebrand, John; Cranford, Ted, PLOS ONE, 2023. The dissertation author was the primary investigator and author of this paper.

Chapter 3

Mapping the San Dieguito Paleochannel and Younger Dryas Landscape

Abstract

More studies on the continental shelf of southern California are needed to expand our baseline knowledge of the local environment throughout the late Pleistocene and Holocene when humans migrated along the Pacific Coast. Human presence was established on the southern California's Channel Islands by the Younger Dryas period, a thousand-year period when eustatic sea level rise abruptly slowed and the global climate's warming trend temporarily reversed, but no archaeological sites been found on the nearby continental shelf from that time. River margins are a promising starting feature for systematic exploration of the continental shelf for evidence of human occupation. We investigate a now-submerged channel offshore the present-day San Dieguito Lagoon in Del Mar, California, focusing on the landscape during the Younger Dryas period. To image the subsurface, we use sub-bottom profiling, allowing us to identify the paleoshoreline that existed during the Younger Dryas, now located at between 57-60 m depth, about 3km out from the current coastline. We map paleochannel margins which remain beneath the modern sediment and observe a deep channel along the northern side of the paleovalley. Using the identified paleoshoreline, we were able to delineate what portion of the landscape was subaerial during the Younger Dryas and to constrain sea level during that time. Additionally, We analyzed three sediment cores from the paleovalley, the deepest of which contains a beach-like

deposit and terrestrial sediments dating to the Younger Dryas. Based on our findings, we support further work in the offshore channel, especially coring in areas where the sub-bottom data suggest preserved paleosurfaces that date to the Younger Dryas or earlier.

3.1 Introduction

The drowned Pacific coast of North America holds key information to understanding how humans from Beringia first travelled and lived on the new continent [Watts et al., 2011, Braje et al., 2019a, Gusick et al., 2021, McLaren et al., 2020]. The precise timing of the initial migration remains unknown, but radiocarbon dates point to a coastal human presence in southern California, on the Channel Islands, by 13 ky BP (years Before Present, where the 'present' is considered 1950) [Erlandson et al., 1996, Erlandson et al., 2011]. At the peak of the last glacial maximum, about 20,000 years ago, sea level was over 125 m lower than it is today, making tens of thousands of square kilometers of the submerged continental shelf available for human traversal and occupation in the millennia since [Lambeck et al., 2014]. Coastal people would have lived with a continually changing landscape and near-constant sea level rise, moving the coast landward. However, they would experience relative stability during the Younger Dryas, a thousand-year period when sea level rise abruptly slowed and the global climate's warming trend temporarily reversed. Inferring how the Younger Dryas affected the local environment is complicated because data related to the southern California climate during the Younger Dryas is limited and its effect may have varied along small spatial scales [Reeder et al., 2011, McLaren et al., 2020]. Reeder 2011 puts forth the possibility that populations along the Pacific Coast of North America during the Younger Dryas were sparse and concentrated in the most productive coastal habitats. The most-studied coastal areas around southern California are the Northern Channel Islands and Isla Cedros off Baja California [Watts et al., 2011, Gusick and Davis, 2019, Gusick et al., 2021, Braje et al., 2019b], which could have had high densities of productive environments. However, little work has been done on the mainland's submerged shelf, and findings from the islands may

not translate directly to the mainland.

In this study we investigate a now-submerged channel offshore the present-day San Dieguito Lagoon in Del Mar, California, focusing on the Younger Dryas. The goals of this project are broadly to add to our understanding of the Younger Dryas along the southern California coast, to investigate the potential attractiveness of the San Dieguito River landscape when humans may have encountered the area, and to determine whether archaeological materials could have survived inundation. Specifically, we locate the Younger Dryas paleoshoreline, map the extent of the San Dieguito paleochannel to the edge of the continental shelf, and collect, analyze, and date materials from sediment cores within the paleovalley. While this is primarily an environmental study, the results could enable future archaeological research [Benjamin, 2010, Westerdahl, 2011, Braje et al., 2019b]. We focus on the submerged portion of the former San Dieguito River as a potentially attractive habitat because rivers supply fresh water and typically support productive and biodiverse habitats when they meet the sea. Furthermore, associated sediment deposits could have survived inundation, potentially preserving artifacts and paleoclimate markers. Human activity further upstream was established by 9,000 years ago at the C W Harris site [Warren and Ore, 2011]; however, an earlier coastal presence may not be directly related to the same people that occupied the inland portion of the river valley. The C W Harris site included preserved materials located in fluvial sediments ([Rogers, 1966, Warren, 1967]), which demonstrates the potential for preservation in paleoriver valleys. Protected by fluvial sediments, archaeological materials could feasibly survive inundation.

The San Dieguito submerged paleochannel was outlined up to $\sim$ 30m water depth as part of an offshore sand dredging project aimed at beach replenishment [Hildebrand and York, 2022]. Interpretations of sub-bottom and core data shed light on the paleolandscape through the 8.2 BP cold event, another period of relatively stable sea level. This work provided a foundation for focusing on the Younger Dryas by working further offshore. The Younger Dryas is marked by a sudden decrease in the rate of eustatic sea level rise about 60m below modern sea level. The relatively stable sea level would have lead to erosion and formation of a paleoshoreline

angle. However, sediment deposited during or after inundation can obscure paleoshorelines and build up the seafloor placing the true paleoshoreline closer to the coast than bathymetry alone may suggest [Laws et al., 2020]. The preserved Younger Dryas paleoshoreline angle is visible with sub-bottom sonar and appears as a wave-cut notch along parts of the shoreline. We have, with moderate confidence, located the Younger Dryas paleoshoreline offshore the San Dieguito lagoon about 3 km out from the current coastline. We use sub-bottom profiles to image the subsurface and map paleochannel margins that remain beneath the modern sediment. We use the identified paleoshoreline to delineate what portion of the landscape was subaerial during the Younger Dryas and to constrain local sea level during that time. We examine three sediment cores from the paleovalley, the deepest of which contains a beach-like deposit below terrestrial runoff, both dating to the Younger Dryas. Sub-bottom and coring results are combined to broadly reconstruct the environment around San Dieguito lagoon at the time of the Younger Dryas.

Combining the sub-bottom profiles and sediment core analyses, we have identified promising locations for potential paleosurfaces within the channel. We suggest further work in the channel, especially work that incorporates coring where the sub-bottom data shows potential Younger Dryas paleosols, which would be instrumental for a detailed landscape reconstruction [Gusick et al., 2022]. We also encourage exploration of other southern California paleochannels, potentially those evaluated in Hildebrand and York 2022 [Hildebrand and York, 2022]. While river margins may not be the only place for human occupation, they are a promising starting feature for systematic exploration of the continental shelf. More studies on the shelf are needed to expand our baseline knowledge of the local environment throughout the late Pleistocene and Holocene when humans may have entered and when the global climate underwent drastic change that we have yet to fully characterize.

3.2 Methods

Sub-bottom profiles and sediment cores were collected in January 2023 aboard the *R/V Sally Ride* as part of cruise SR2301. Cores were analyzed and archived at the Scripps Institution of Oceanography.

3.2.1 Geophysical Survey

Sub-bottom profiles were collected using the *Sally Ride's* hull-mounted Kongsberg SBP29 sub-bottom profiler. The SBP29 used a 9-2 kHz linear chirp pulse with a 30 ms pulse length and 1 ms ping interval. Source power was set to 208 dB (-12 dB from the SBP29 maximum source power) to reduce potential hazards for marine mammals. The SBP29 shares the EM712 multibeam array, and was set to use a wide half array for the transmitted beam and the full array for the received beam, with received beam spacing set to 3 degrees. We acquired 5 beams, but use the direct-downward (0 deg) beam in this study. Vessel speed was kept to about 4 kts. Survey lines were arranged primarily in a shore-parallel and shore-orthogonal grid (fig. 3.1). Seafloor depth ranged from 35 m to the edge of the continental shelf ($\sim$100 m). North-south profiles were collected with 100-500m spacing, and east-west profiles were collected with $<$1 km spacing.

The profiles were processed using the Kongsberg SBP29 acquisition and processing software (SBP/Topas OS Version 1.9.4, 2022.02.22) using a matched filter and uniform gain correction. While raw data was collected, we use instantaneous amplitude (envelope data) throughout this study. Processed profiles were visualized in *MATLAB* for interpretation. *SeisLab 3.02* was used to read in the profiles, and we used *MATLAB* plotting functions to visualize and trace the data. Tide corrections were applied to each sonar ping using harmonic tide predictions from NOAA's La Jolla station (Station ID: 9410230). All profiles displayed assume a constant sound speed of 1500 m/s, but reported depths beneath the seafloor are calculated assuming sound speeds of 1500 m/s in water and 1600 m/s in sediment [Wang et al., 2021].

We used previously collected multibeam data from the Seafloor Mapping Lab (grid

SoCal_H11877) for both cruise planning and post-cruise interpretation. EM712 Multibeam data was collected simultaneously with the SBP29 during the January cruise, but was not used in the current study.

3.2.2 Sediment Core Acquisition and Archival

Cores were collected with a Rossfelder P-5 vibracore system in clear butyrate liners fitted in a 4" diameter steel tube. Core locations were chosen at intersections of the sub-bottom profiles. Nine vibracores total were attempted. Two had minimal recovery (1VC is 39cm and 2VC is 48cm), and four came up bent (3VC, 4VC, 5VC, and 7VC). We analyzed the remaining three (6VC, 8VC, and 9VC) which had 116cm, 141cm, and 174cm recovery respectively (6VC = 6th Vibracore (VC) attempted). Locations of the analyzed cores are shown in fig. 3.1. While the bent cores could indicate something about the seafloor surface, they more likely resulted from too much tension held on the vibrating motor's power cable, which led to tilted vibracore penetration into the seafloor and bending during core extraction. Cores 8VC and 9VC were successful after slackening the power cable. Unfortunately, coring operations were ended early, after 9VC, due to a malfunction in the power box of the vibracorer.

All of the cores are stored, refrigerated at 4°C, at the Scripps Institution of Oceanography core repository in La Jolla, California. Short cores 1VC and 2VC are stored unsplit, and bent cores remain in the bent steel pipes at the time this is being written. The three cores used in this analysis were split and separated into working and archive halves. The archive half was subject to imaging and XRF scanning, and the working half was sampled for dating, loss on ignition, and grain size analyses.

3.2.3 Sediment Analysis

Imaging and XRF

Cores 6VC, 8VC, and 9VC were subject to visual description and imaging with a Line Scan camera immediately after splitting. The archive half was later scanned with an Avaatech

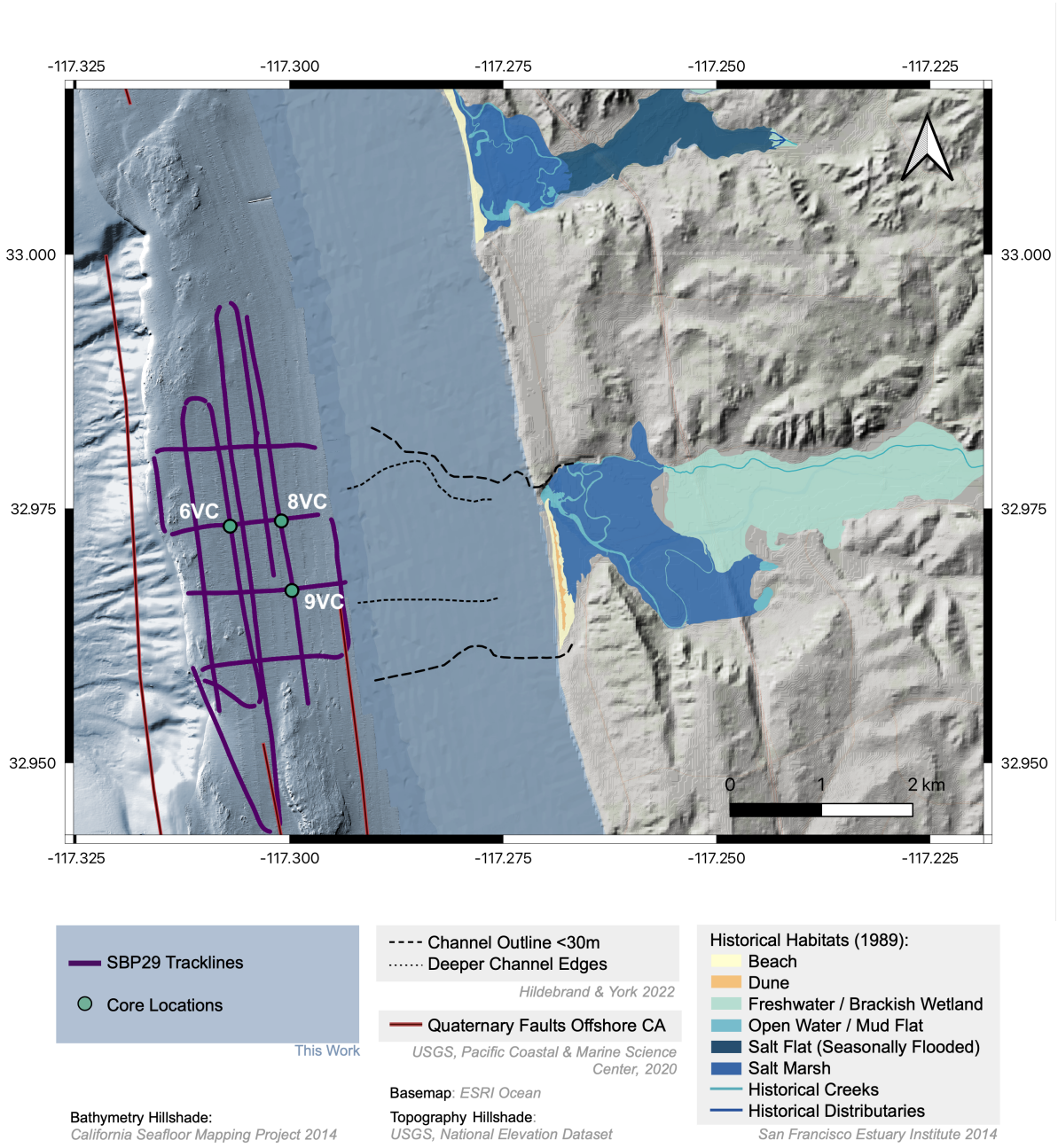

Figure 3.1. Sonar tracks and core locations in relation to the previously mapped extent of the San Dieguito paleovalley. Thick purple lines indicate sub-bottom tracks of the present study. Green dots indicate sediment cores with $>$ 1 m retrieval, labeled 6VC, 8VC, and 9VC. Black dotted and dashed lines represent the offshore extent of the San Dieguito channel at $<$30m depth [Hildebrand and York, 2022]. Onshore historical habitats from 1989 (pre-development) are shaded for present-day San Dieguito and San Elijo Lagoons [Beller et al., 2014, (SFEI), 2014]. Bathymetry $>$30 m is the bathymetry hillshade from the Seafloor Mapping Lab, grid SoCal_H11877. Topography is from the USGS National Elevation Dataset. Bathymetry $<$30 m is ESRI Ocean basemap. Mapped quaternary faults are in red [Walton et al., 2020].

X-Ray Fluorescence (XRF) core-scanner. Each core was scanned twice - with excitation energy 10 eV followed by 30 eV. Higher excitation energies were omitted to reduce scanning time. Measurements were made every 2cm down the core to balance resolution with scanning time.

Dating

Dated samples were picked from bulk samples taken from the cores in 2cm depth segments. Each bulk sample was washed with DI water through a series of sieves (1mm, 500 μm, 250 μm, 125 μm, and 60 μm) and dried over filter paper in a drying oven at 39.5 °C. The dry sample was separated through a series of dry sieves (500 μm, 250 μm, 125 μm) and each fraction was examined under a microscope for materials. Plants and charcoal were preferentially chosen over mollusks to reduce potential dating error from the marine reservoir effect. A total of 14 samples were sent: 6 from VC6, 3 from VC8, and 5 from VC9 (table 3.1). All samples were comprised of mixed plant materials and charcoal, shown in figures 3.2, 3.3, and 3.4.

Radiocarbon dating was conducted at UC Irvine's W.M Keck Carbon Cycle Accelerator Mass Spectrometer. Samples were treated with acid-base-acid (1N HCl and 1N NaOH, 75°C) prior to combustion. Radiocarbon concentrations are given as fractions of the Modern standard (relative to PDB), Δ14C, and conventional radiocarbon age, following the conventions of Stuiver and Polach, 1977 [Stuvier and A., 1977]. Sample preparation backgrounds have been subtracted, based on measurements of 14C-free wood. All results have been corrected for isotopic fractionation according to the conventions of Stuiver and Polach [Stuvier and A., 1977], with δ13C values measured on prepared graphite using the AMS spectrometer. These can differ from δ13C of the original material, and are not given.

On first attempt, all samples failed to graphitize, likely due to sulfur present in the samples. After further pre-processing by the UC Irvine group, 10 of the 14 samples were successfully dated by 14C, though 4 samples contained less than 0.5 mg. The 14C dates were calibrated using the *OxCal 4.4* online software. Calibrated dates will be presented throughout the paper as cal BP. Sample depth-in-core and age measurements are shown in table 3.1.

Table 3.1. Samples prepared for carbon dating at UC Irvine's W.M Keck Carbon Cycle Accelerator Mass Spectrometer. Sample ID begins with the core ID. Samples were comprised of plant material and charcoal. The calibrated age is shown as the 95.4% convidence interval. Samples that failed to graphitize for dating are denoted by †, and samples with * had less than 0.25 mgC dated material.

Sample ID	Depth in Core [cm]	14C Age [ky BP]	Calibrated Age [ky cal BP]
6VC-5	49-51	10165 ± 20	11935 - 11737
6VC-6	54-56	10570 ± 25	12685 - 12490
6VC-8*	78-80	8660 ± 80	9904 - 9488
6VC-10	98-100	10875 ± 25	12832 - 12747
6VC-11	105-107	10945 ± 25	12901 - 12763
6VC-12†	112-114	-	-
8VC-1*	10-12	1680 ± 20	1689 - 1531
8VC-7	66-68	10450 ± 30	12612 - 12105
8VC-11*	106-108	9695 ± 25	11204 - 10888
9VC-5*	50-52	1905 ± 50	1942 - 1710
9VC-8†	83-85	-	-
9VC-9†	93-95	-	-
9VC-11	115-117	9325 ± 25	10647 - 10492
9VC-12†	125-127	-	-

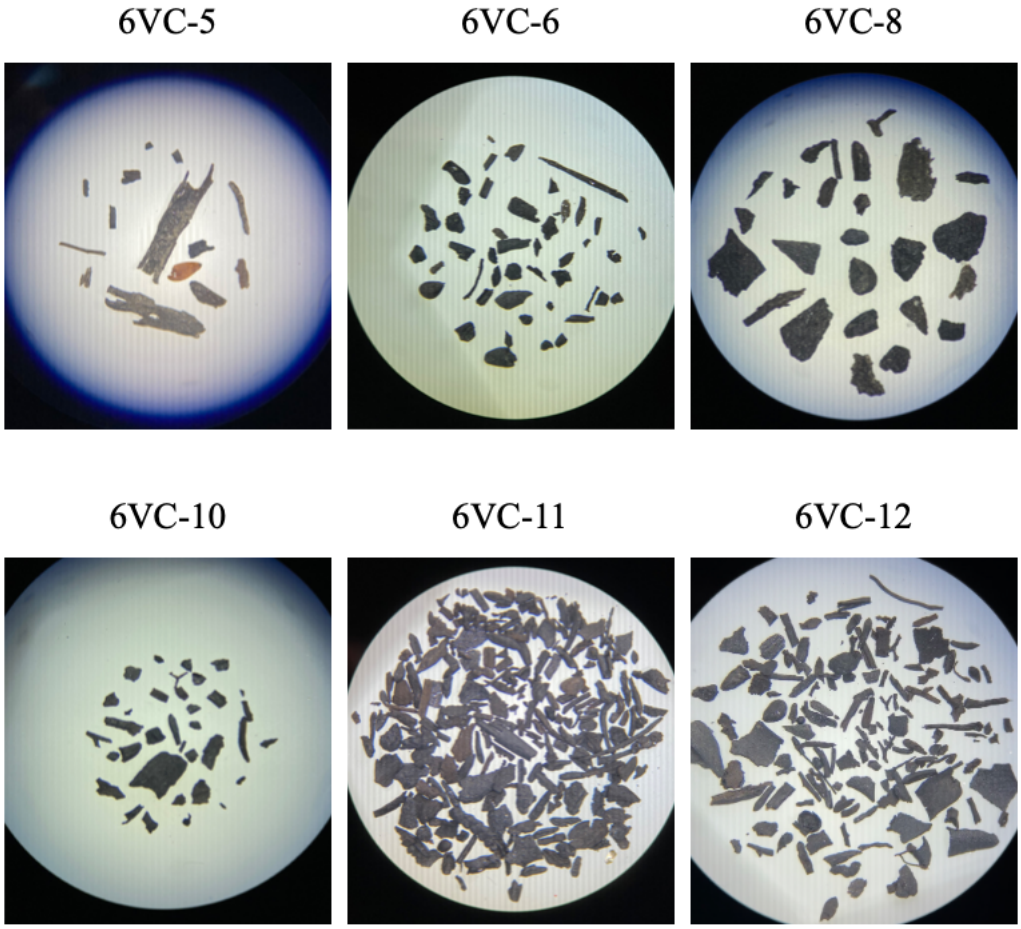

Figure 3.2. Microscope image of samples prepared for carbon dating from core 6VC. Images were taken through a Leica EZ4 microscope with LED illumination. Sample picks range in size from 500 μm to a few mm. Sample 6VC-12 ultimately failed to graphitize and was not dated. Sample 6VC-8 produced a date measurement, but the dated sample was small (0.052 mgC). Images are not all to the same scale.

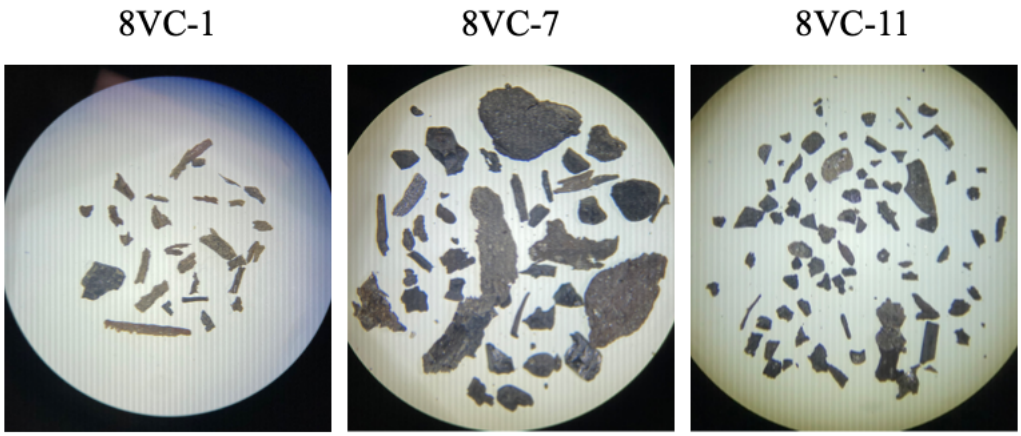

Figure 3.3. Microscope image of samples prepared for carbon dating from core 8VC. Images were taken through a Leica EZ4 microscope with LED illumination. Sample picks range in size from 500 μm to a few mm. Samples 8VC-1 and 8VC-11 produced date measurements, but the dated samples were small (0.24mgC and 0.21mgC respectively). Images are not all to the same scale.

Loss On Ignition

Loss on ignition (LOI) measurements were taken to determine %mass of organic material in discrete samples along the core. LOI samples were taken from bulk samples taken from the cores in 2cm depth segments. Each bulk sample was left in a drying oven at 39.5°C until dry (until the mass difference was < 0.01g between measurements at least 1 day apart). Each sample was gently crushed to break up the sediment, and 5 g was placed in a dry crucible (heated to 375°C for 90 minutes then placed in a desiccating rack until use), then heated to 550°C for 90 minutes. After cooling in the oven, the sample was weighed to 0.001g precision, and the mass difference before and after was taken to be organic material lost on ignition.

Grain Size Analysis

Grain size distribution was measured with a Fritsch laser particle analyzer. Grain size samples were taken from the same bulk samples used for LOI measurements, but did not include sediments that had been crushed prior to the LOI procedure. For each sample, 0.2-2g of sediment was mixed with water, sieved to remove pieces $>$ 1cm (primarily shell fragments), and mixed

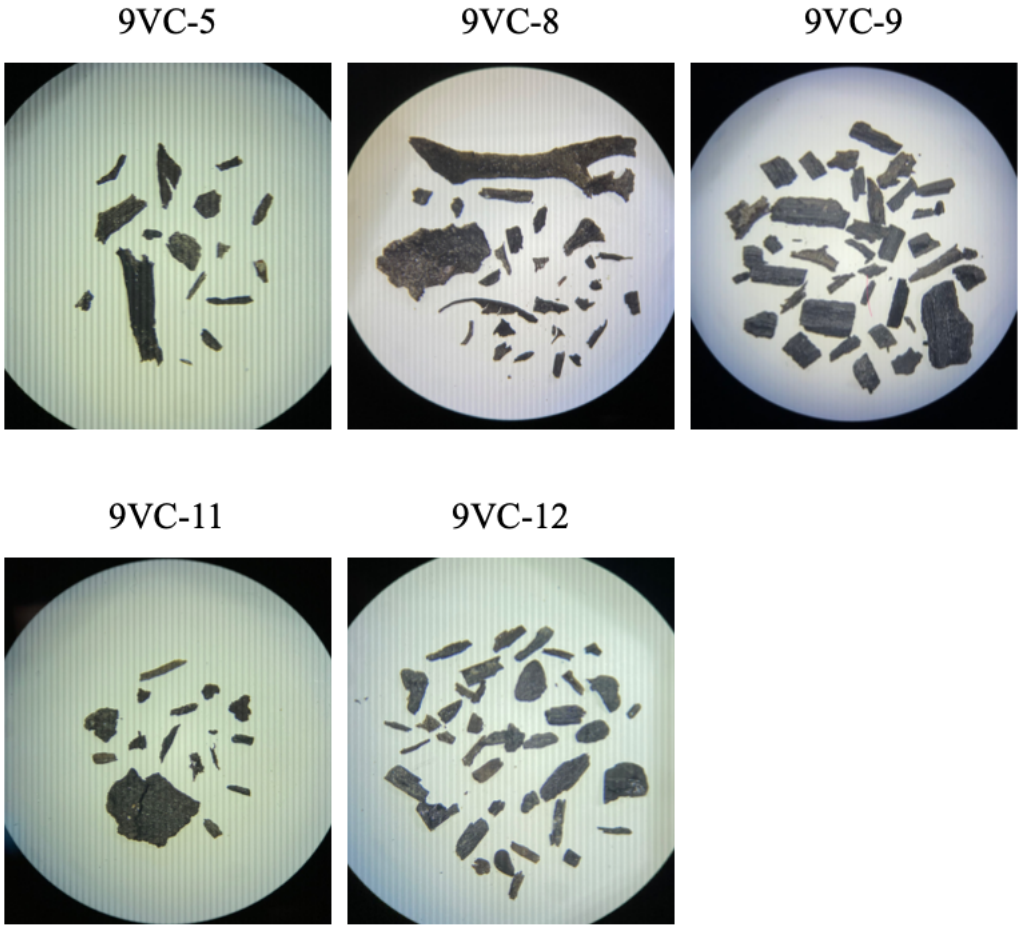

Figure 3.4. Microscope image of samples prepared for carbon dating from core 9VC. Images were taken through a Leica EZ4 microscope with LED illumination. Sample picks range in size from 500 μm to a few mm. Samples 9VC-8, 9VC-9, and 9VC-12 ultimately failed to graphitize and were not dated. Sample 9VC-5 produced a date measurement, but the dated sample was small (0.060 mgC). Images are not all to the same scale.

with 20ml Calgon to break up the remaining particles. The wet sample was added to the particle analyzer where it was agitated for 1-2 minutes, then analyzed three times by the machine. Results presented here are the average of these measurements. In cases where the measurements were inconsistent, a new sample was run through the process, and all resulting analyses were averaged. Inconsistent measurements may have resulted from the presence of irregularly-shaped shell material in the sample; most variability between samples appeared in the large particle fractions.

3.3 Results

3.3.1 Paleoshoreline and Channel Mapping

We identified 3 potential paleoshoreline angles in each of the east-west profiles (figs. 3.6, 3.7, 3.8, 3.9, 3.10). We identify as a paleoshoreline angle only notches that we can see in all east-west profiles at a close range of depths. While there is some variation in depth, we note that depth of a paleoshoreline can change even on small spatial scales. We label the paleoshoreline between 56.6-59.7m depth as the Younger Dryas shoreline, because the picked notches show the characteristic sedimentation pattern of a paleoshoreline, in which transgressive deposits create a layer starting above the paleoshoreline angle and extending over the abrasion platform [Laws et al., 2020]. We identified two additional potential shorelines, labelled B and C at 52.9-55.4 m and 49.9-51.7 m depth respectively. Both of those potential shorelines are covered by only one acoustic unit in the southern two east-west survey lines: in fig. 3.8, where they appear most clearly, and in fig. 3.9, where they are barely perceptible. Shoreline pick B is covered by two acoustic units of sediment in the northern two east-west profiles, which run on either side of the deep northern channel.

We outlined the offshore extent of the San Dieguito river valley based on sediment thickness from the sub-bottom profiles combined with rocky features that appear in the bathymetry (fig. 3.5). The deeper portion along the northern edge of the channel outlined in Hildebrand and York 2022 continues as a deep channel in our survey, veering northward near the edge of the shelf

(blue arrow in fig. 3.11). Increased sediment thickness near the southern extent of the survey area points toward a drainage path to the south as well (figs. 3.5). The sub-bottom profiles from the deep northern channel reveal 3-4 acoustic units at seafloor depths greater than the picked Younger Dryas shoreline, while shallower portions of the channel contain just 2 units (fig. 3.11). Multiple acoustic layers of sediment appear on either side of this deep northern channel.

The rocky features and raised portions of the acoustic basement visible in the bathymetry and sub-bottom profiles may have resulted from a combination of local tectonics and differential erosion of the bedrock. A large raised feature, visible in the bathymetry along the southern edge of the channel, appears to have continued north beneath the sediment in the channel valley. The profiles reveal only one acoustic unit north of the raised feature, west of the continued raised feature visible in the sub-bottom profiles, and east of the identified Younger Dryas paleoshoreline in this area (orange region in fig. 3.11).

3.3.2 Sediment Analysis

Visual descriptions and images of cores 6VC, 8VC, and 9VC are shown with dating, loss on ignition, grain size analysis, and XRF results in figures 3.12, 3.13, and 3.14. Core 6VC is the most variable with depth and contains a coarser sand section between two layers of higher organic content, all dated to the Younger Dryas. The sand layer section between 70-80 cm core depth displays possible bedding, and the XRF data shows raised levels of Si/Ca and Pb/Rb. The top 50cm of the core is composed of Holocene sediment, which has an organic content comparable to the tops of cores 8VC and 9VC and contains a mix of silty sand and sand.

Core 8VC has a potential Younger Dryas date at 66-68cm, but also has an earlier, Holocene date at 106-108 cm. This could be a true date inversion in the stratigraphy, indicating that the older sediment was deposited after the younger. Alternatively, the younger date in the deepest sample from 8VC may be less reliable, as it contained only a small amount (0.21 mgC) of datable material. The out-of-sequence date in the middle of 6VC was also more recent than expected, but used a much smaller amount (0.052 mgC) of material. The other small (< 0.25

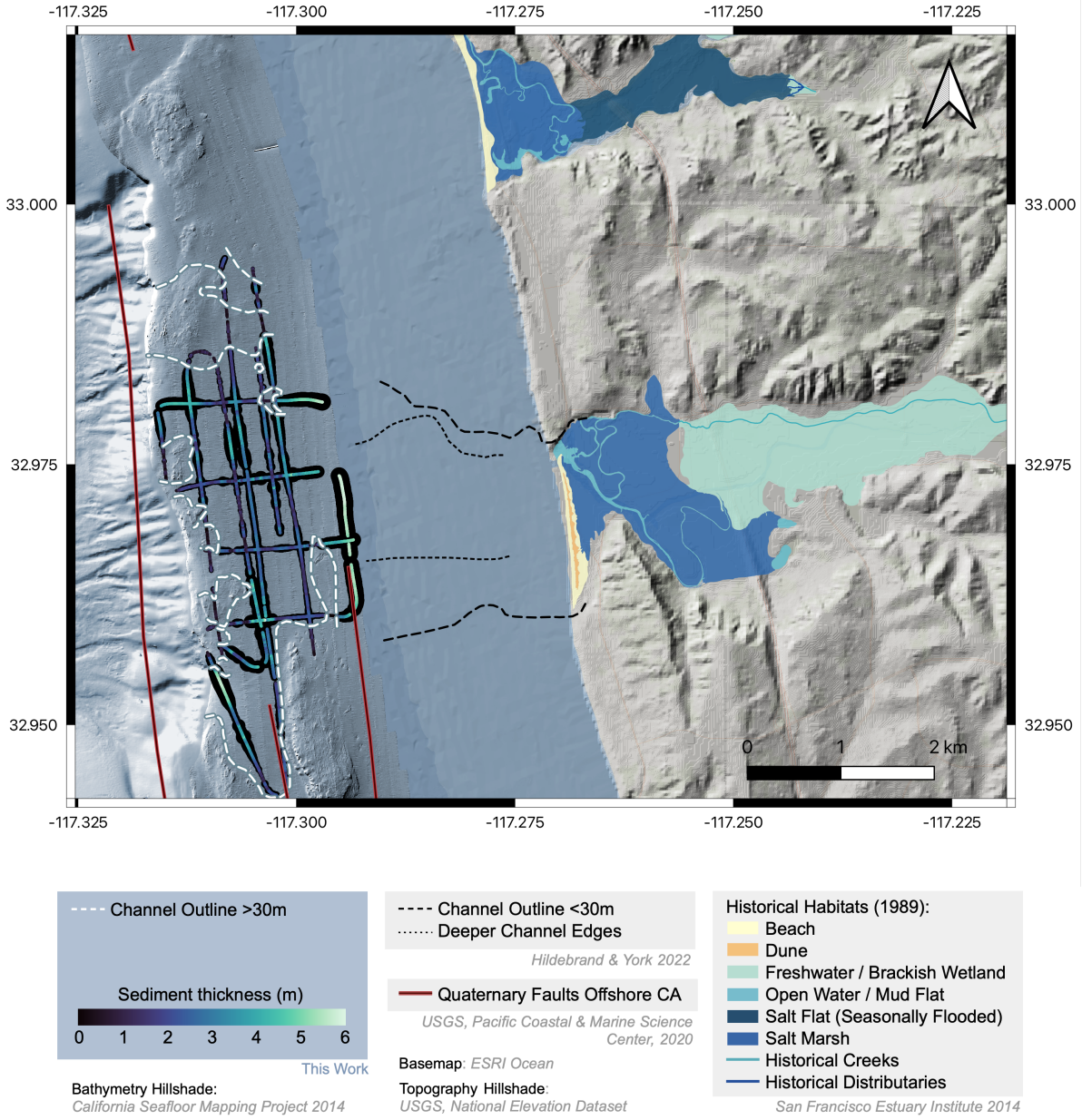

Figure 3.5. Mapped extension of the San Dieguito paleochannel to the edge of the continental shelf. SR2301 sub-bottom survey lines are colored to show sediment thickness (depth of acoustic basement beneath seafloor); colored lines are backed by black shading with width proportional to the same values. White dotted lines outline the channel from 30 m depth to the shelf edge. Black dotted and dashed lines indicate the offshore extent of the San Dieguito channel at ¡30 m depth [Hildebrand and York, 2022]. Onshore historical habitats from 1989 (pre-development) are shaded for present-day San Dieguito and San Elijo Lagoons [Beller et al., 2014, (SFEI), 2014]. Bathymetry >30 m is the bathymetry hillshade from the Seafloor Mapping Lab, grid SoCal_H11877. Topography is from the USGS National Elevation Dataset. Bathymetry <30 m is ESRI Ocean basemap. Mapped quaternary faults are in red [Walton et al., 2020].

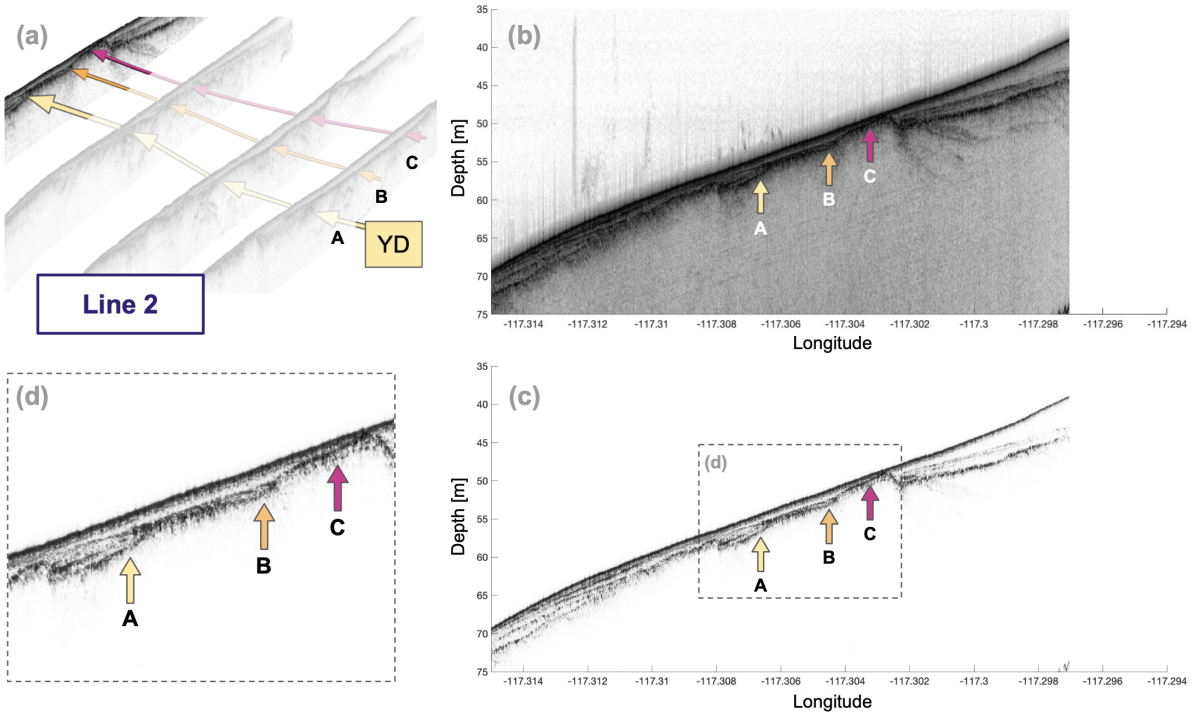

Figure 3.6. East-west SBP29 track, line 2, with 3 picked paleoshorelines. (a): The four E-W profiles are shown with the picked paleoshoreline angles, labeled A, B, and C, linked together by colored arrows. Each profile is shown twice with log scale shading (b) and linear shading (c). The three shoreline angle picks are labelled A, B, and C; the deepest of these, A, was identified as the Younger Dryas. (d): zoomed-in view of the three picks.

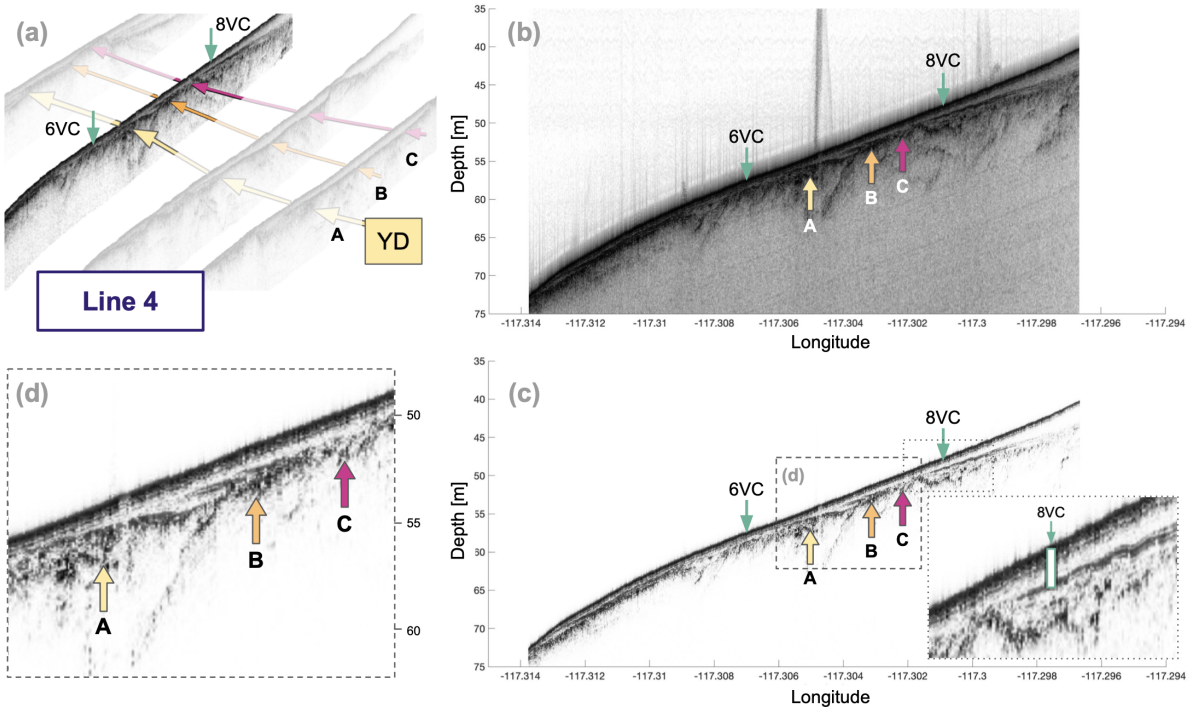

Figure 3.7. East-west SBP29 track, line 4, with 3 picked paleoshorelines. (a): The four E-W profiles are shown with the picked paleoshoreline angles, labeled A, B, and C, linked together by colored arrows. Each profile is shown twice with log scale shading (b) and linear shading (c). The locations of cores 6VC and 8VC are each indicated by a green arrow. Core 6VC contains Younger Dryas sediments. Core 8VC does not extend to the acoustic basement (c inset). The three shoreline angle picks are labelled A, B, and C; the deepest of these, A, was identified as the Younger Dryas. (d): zoomed-in view of the three picks.

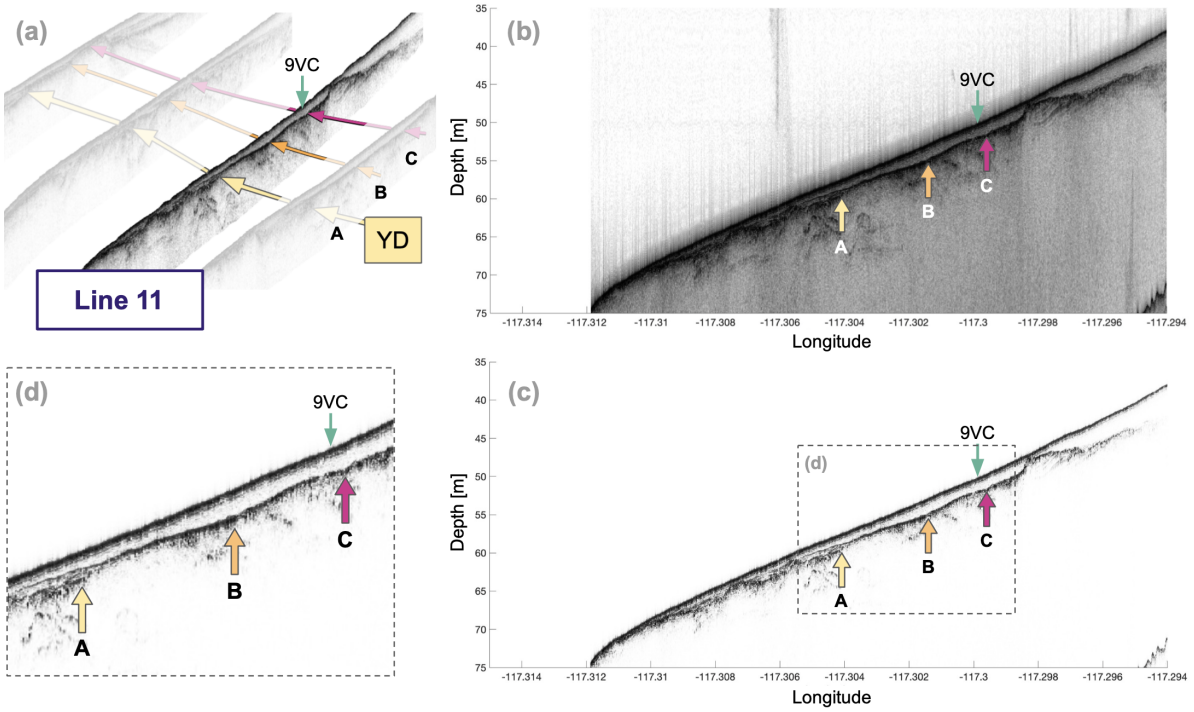

Figure 3.8. East-west SBP29 track, line 11, with 3 picked paleoshorelines. (a): The four E-W profiles are shown with the picked paleoshoreline angles, labeled A, B, and C, linked together by colored arrows. Each profile is shown twice with log scale shading (b) and linear shading (c). The location of core 9VC is indicated by a green arrow. The three shoreline angle picks are labelled A, B, and C; the deepest of these, A, was identified as the Younger Dryas. (d): zoomed-in view of the three picks. Core 9VC contained all Holocene sediment, indicating that all of the sediment above potential shoreline angles B and C was from the Holocene. This could happen under arid, windy conditions; if the Younger Dryas shoreline is pick A, then strong winds could blow away sediment onshore, leaving the bedrock exposed. Subsequent sea level rise and Holocene sediment deposit would then directly cover the bedrock.

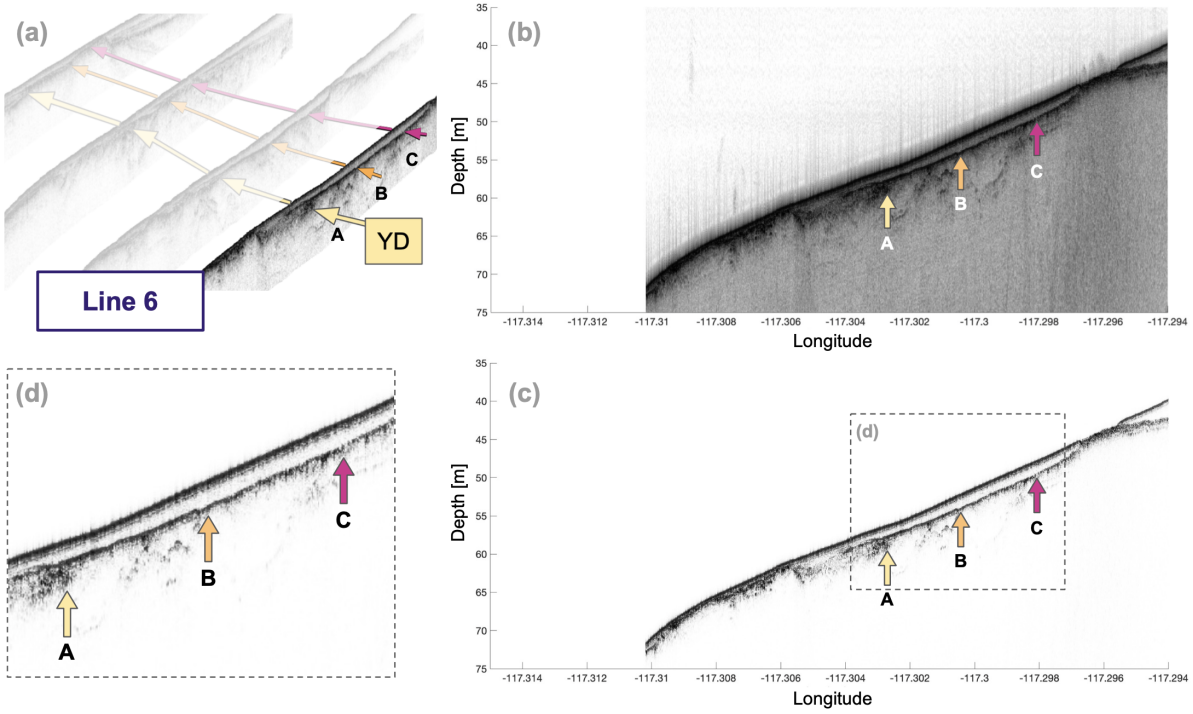

Figure 3.9. East-west SBP29 track, line 6, with 3 picked paleoshorelines. (a): The four E-W profiles are shown with the picked paleoshoreline angles, labeled A, B, and C, linked together by colored arrows. Each profile is shown twice with log scale shading (b) and linear shading (c). The three shoreline angle picks are labelled A, B, and C; the deepest of these, A, was identified as the Younger Dryas. (d): zoomed-in view of the three picks. Note that potential shoreline angles B and C here are slight, much less noticeable than in the other E-W profiles.

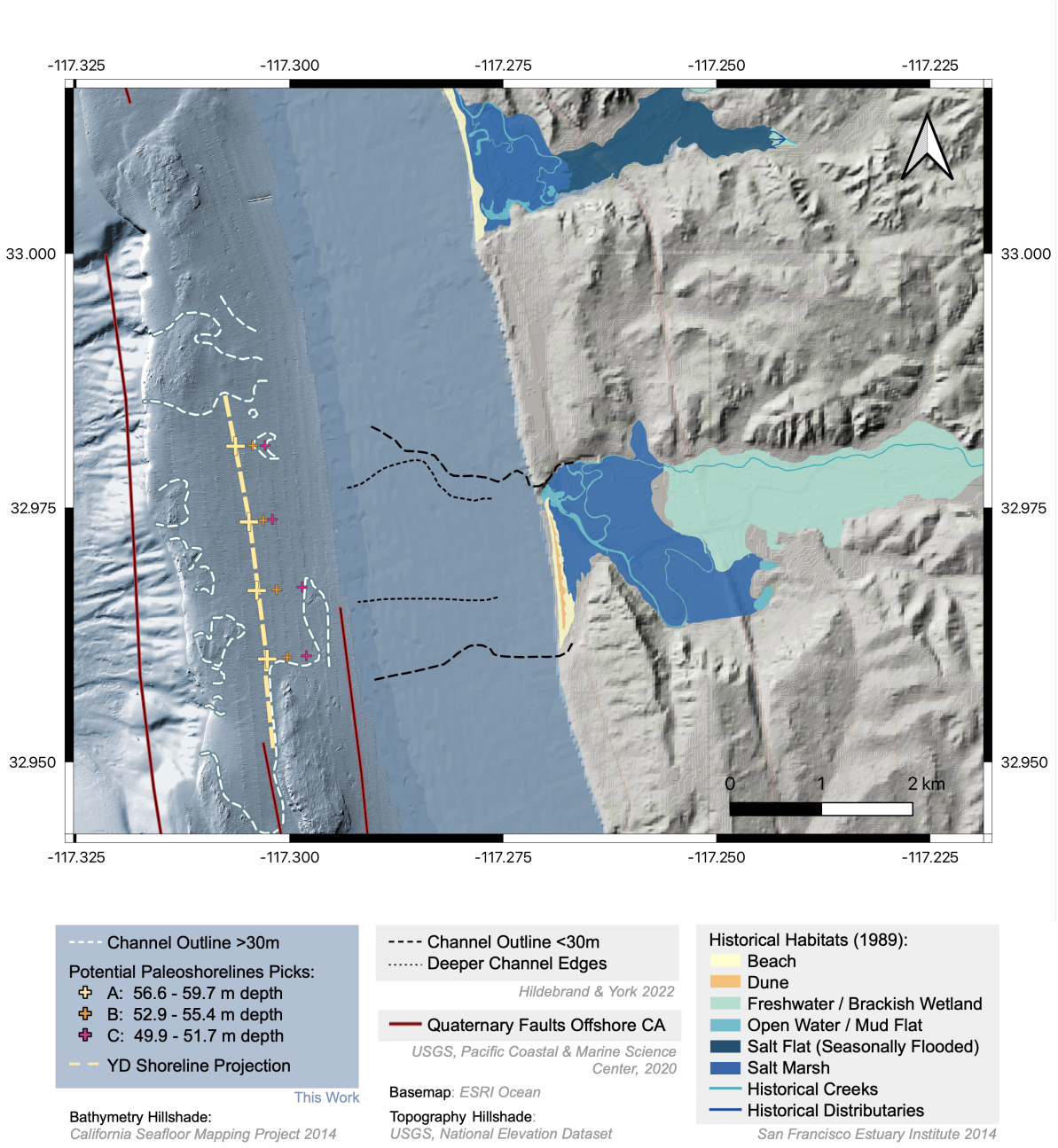

Figure 3.10. Potential paleoshorelines within mapped extent of the San Dieguito paleovalley. Potential paleoshorelines A, B, and C correspond to picked paleoshoreline angles from figures 3.6, 3.7, 3.8, 3.9. White dotted lines outline the channel from 30m depth to the edge of the shelf. Black dotted and dashed lines indicate the offshore extent of the San Dieguito channel at $<$ 30m depth [Hildebrand and York, 2022]. Onshore historical habitats from 1989 (pre-development) are shaded for present-day San Dieguito and San Elijo Lagoons [Beller et al., 2014, (SFEI), 2014]. Bathymetry $>$30 m is the bathymetry hillshade from the Seafloor Mapping Lab, grid SoCal_H11877. Topography is from the USGS National Elevation Dataset. Bathymetry $<$30 m is ESRI Ocean basemap. Mapped quaternary faults are in red [Walton et al., 2020].

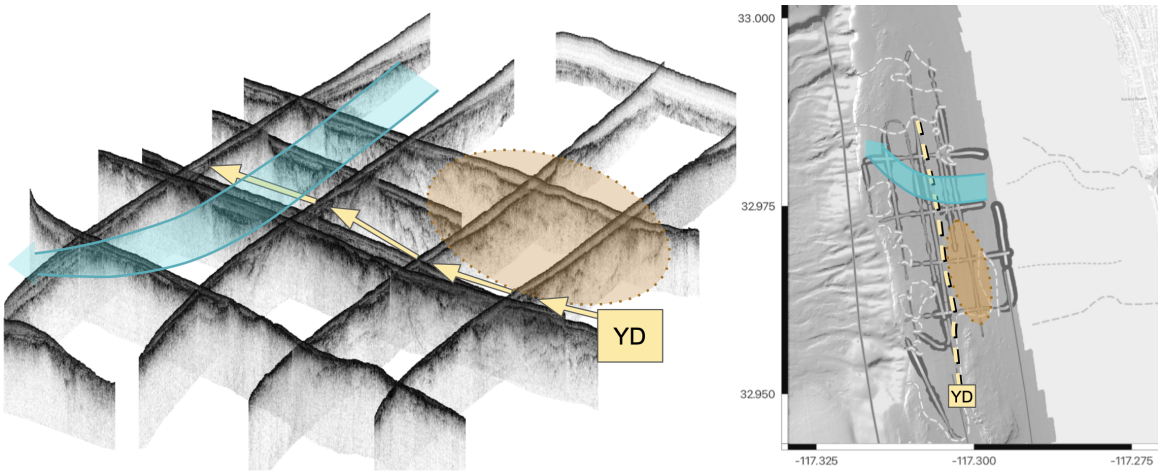

Figure 3.11. Left: Fence diagram of truncated beach parallel and beach orthogonal SBP29 tracklines. The Younger Dryas shoreline is indicated by a yellow dash. A relatively deep channel is signaled on the north side of the river valley margin by a blue arrow. The orange oval points to an area which appears to contain only Holocene sediment cover. Right: Top view of the survey area with the same annotations.

mgC) samples were the shallowest in cores 8VC and 9VC, so we cannot easily tell if they fit the trend because there is no shallower material to compare them to. Additionally, samples from 104-106cm show signs of reworking or bioturbation, which may have increased chances of date contamination.

Core 8VC has fairly uniform grain size except in the silt lenses at 102-105 cm depth and again at 110-112 cm, where the sample is almost entirely silt instead of silty-sand as it is in the rest of the core. These lenses contain relatively high amounts of organic material (LOI is the highest for these samples across all cores). The XRF ratios show peaks in Fe/Ca and Ti/Ca ratios indicating terrestrial origin, along with a dip in Pb/Rb. The XRF data also shows clear trends between 50-92 cm with decreased Fe/Ca and Ti/Ca, steadily increasing Si/Ca, and raised Pb/Rb counts. The organic content and grain size stay fairly constant throughout this portion of the core.

Core 9VC appears to have made it through the sediment layer since the bottom contains what we identified as glauconite. A date near bottom is early Holocene, and there are no obvious changes in the LOI, grain size, or XRF measurements, indicating that it is all Holocene sediment

above the bedrock.

3.4 Discussion

The most obvious feature in the sub-bottom data is the deep channel in the north of the river valley that bends northward before reaching the edge of the continental shelf (3.11). We outlined the offshore extent of the San Dieguito river valley based on sediment thickness from the sub-bottom profiles combined with rocky features that appear in the bathymetry (fig. 3.5). Combining results from Hildebrand and York 2022 with our survey shows the deepest channel of the river valley in the north, from its present location to the edge of the shelf. However, we do see other potential water paths which may have been active at different points in time. Increased sediment thickness near the southern extent of the survey area could indicate a drainage path to the south as well (figs. 3.5).

Separating paleoshoreline angles from channel edges is non-trivial. We identified 3 potential paleoshorelines, but we may not have picked out all that exist. Some notch-like features at depths greater than 60m were not clearly identifiable in all four east-west profiles. These features may have been paleoshorelines that are not equally preserved in all portions of the survey area, but could also represent paleochannel edges. Additionally, paleoshoreline-like features may have been created due to faulting and folding which is known to exist in the vicinity of San Dieguito's offshore extent as part of the Rose Canyon Fault Zone.

The Younger Dryas paleoshoreline we identified appears between 56.6-59.7m depth in all four east-west sub-bottom profiles. This shoreline exhibits the characteristic sediment cover of paleoshorelines that underwent inundation [Laws et al., 2020]. The Younger Dryas shoreline angle is shallower to the north, but the notch in the southernmost profile is the largest, filled with the greatest sediment thickness. This could mean that the bedrock on the southern edge of the channel is softer and more susceptible to erosion. This could also be due to wetlands around the channel that took on much of the water at high tide, preventing formation of a large cliff.

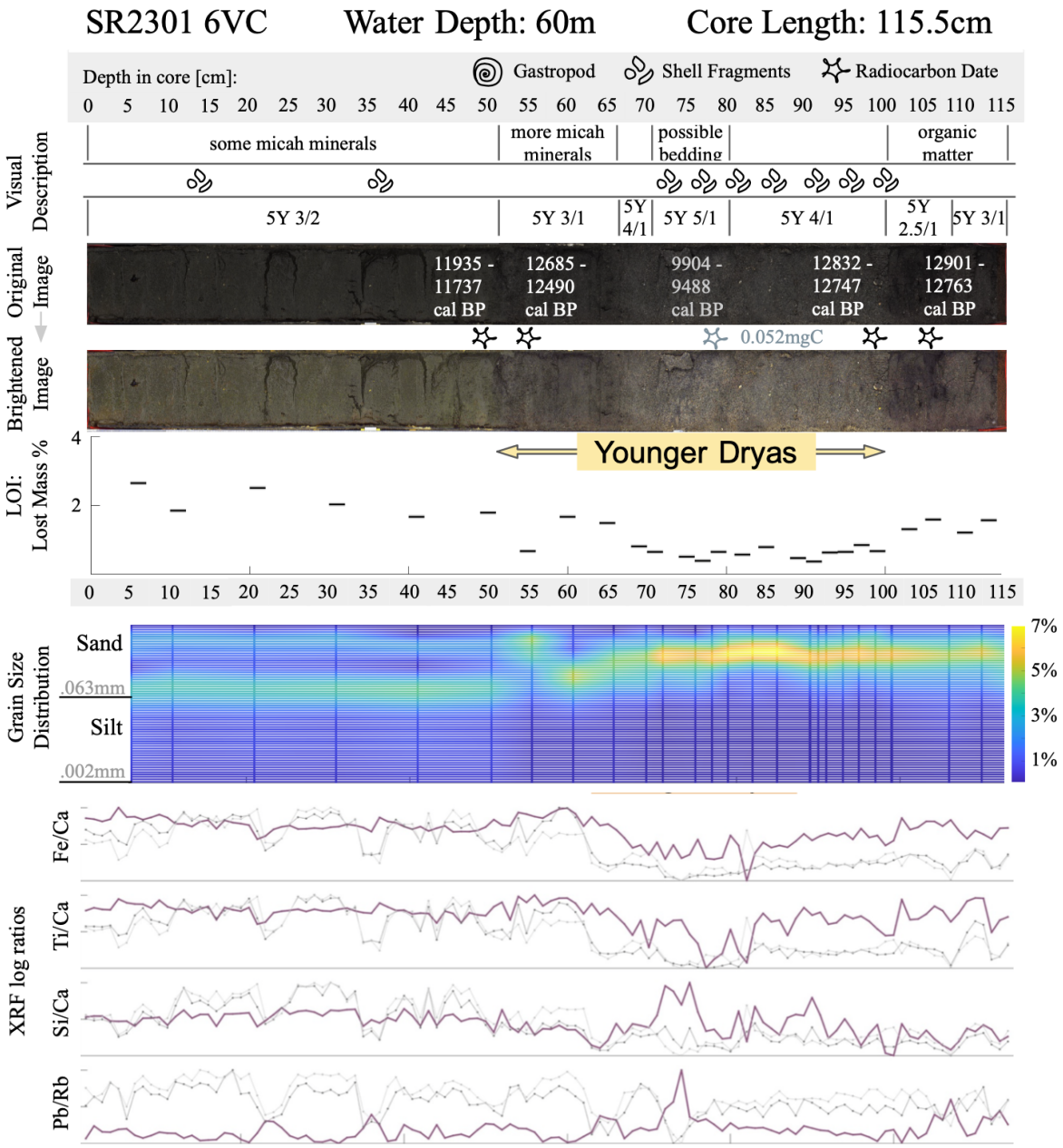

Figure 3.12. Description of core 6VC. The core was taken at 60 m water depth and is 115.5 cm long. Depth in the core increases from left to right. The visual description is shown along with colors from the Munsell color chart. The original image is shown above a 'brightened' image in which the image exposure, saturation, and sharpness were set to maximum. Radiocarbon-dated sample intervals are shown between the two images. Below the images are the loss on ignition and grain size results. Loss on ignition is displayed as the percent of mass loss for each sample. Grain size plots show the percentage of sample measured at each grain size for sample core depth. Solid lines denote measured grain size distributions, which are interpolated to shade the full plot range. At bottom are the Fe/Ca, Ti/Ca, Si/Ca, and Pb/Rb count ratios obtained from the XRF scan.

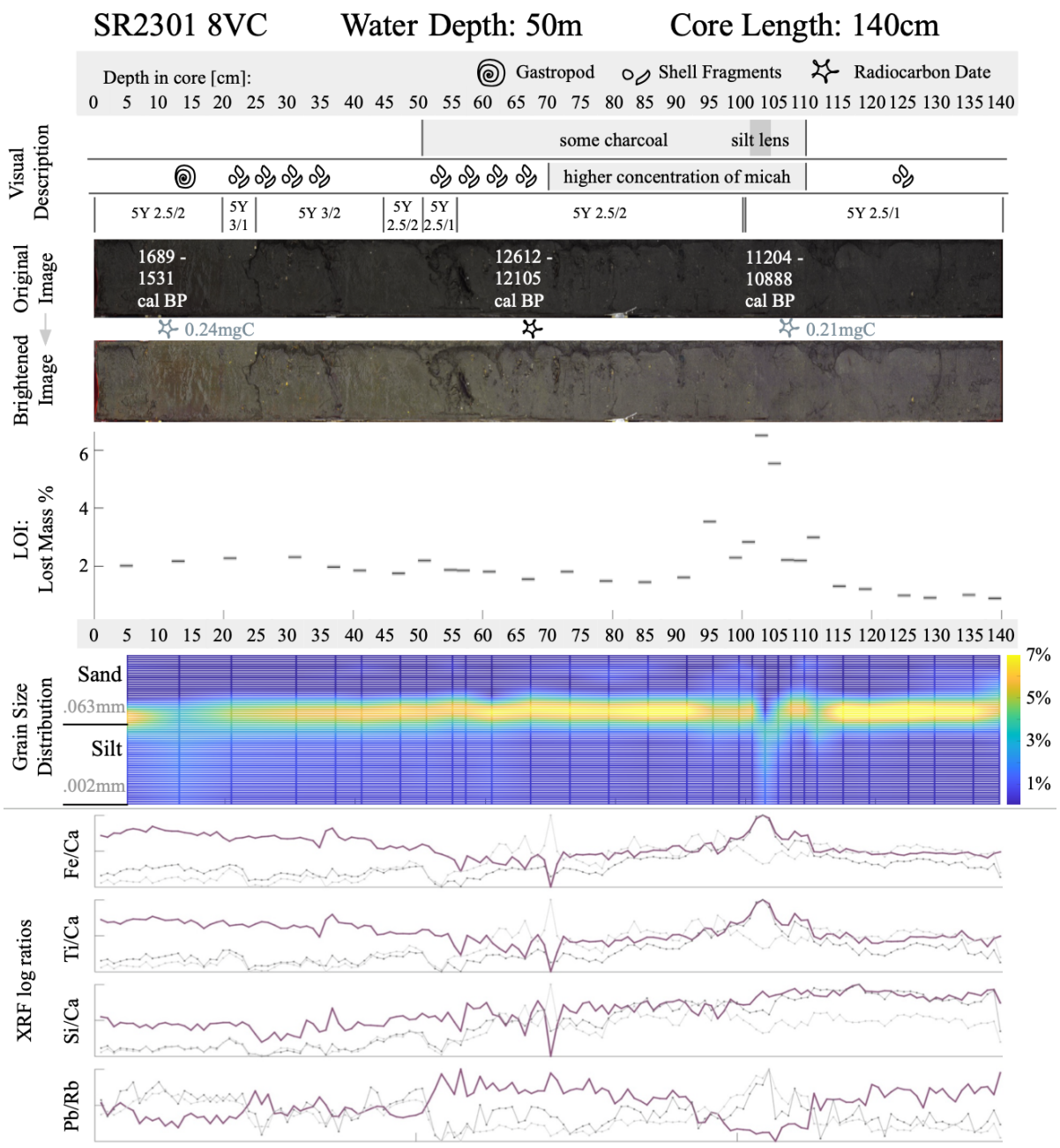

Figure 3.13. Description of core 8VC. The core was taken at 50 m water depth and is 140 cm long. Depth in the core increases from left to right. The visual description is shown along with colors from the Munsell color chart. The original image is shown above a 'brightened' image in which the image exposure, saturation, and sharpness were set to maximum. Radiocarbon-dated sample intervals are shown between the two images. Below the images are the loss on ignition and grain size results. Loss on ignition is displayed as the percent of mass loss for each sample. Grain size plots show the percentage of sample measured at each grain size for sample core depth. Solid lines denote measured grain size distributions, which are interpolated to shade the full plot range. At bottom are the Fe/Ca, Ti/Ca, Si/Ca, and Pb/Rb count ratios obtained from the XRF scan.

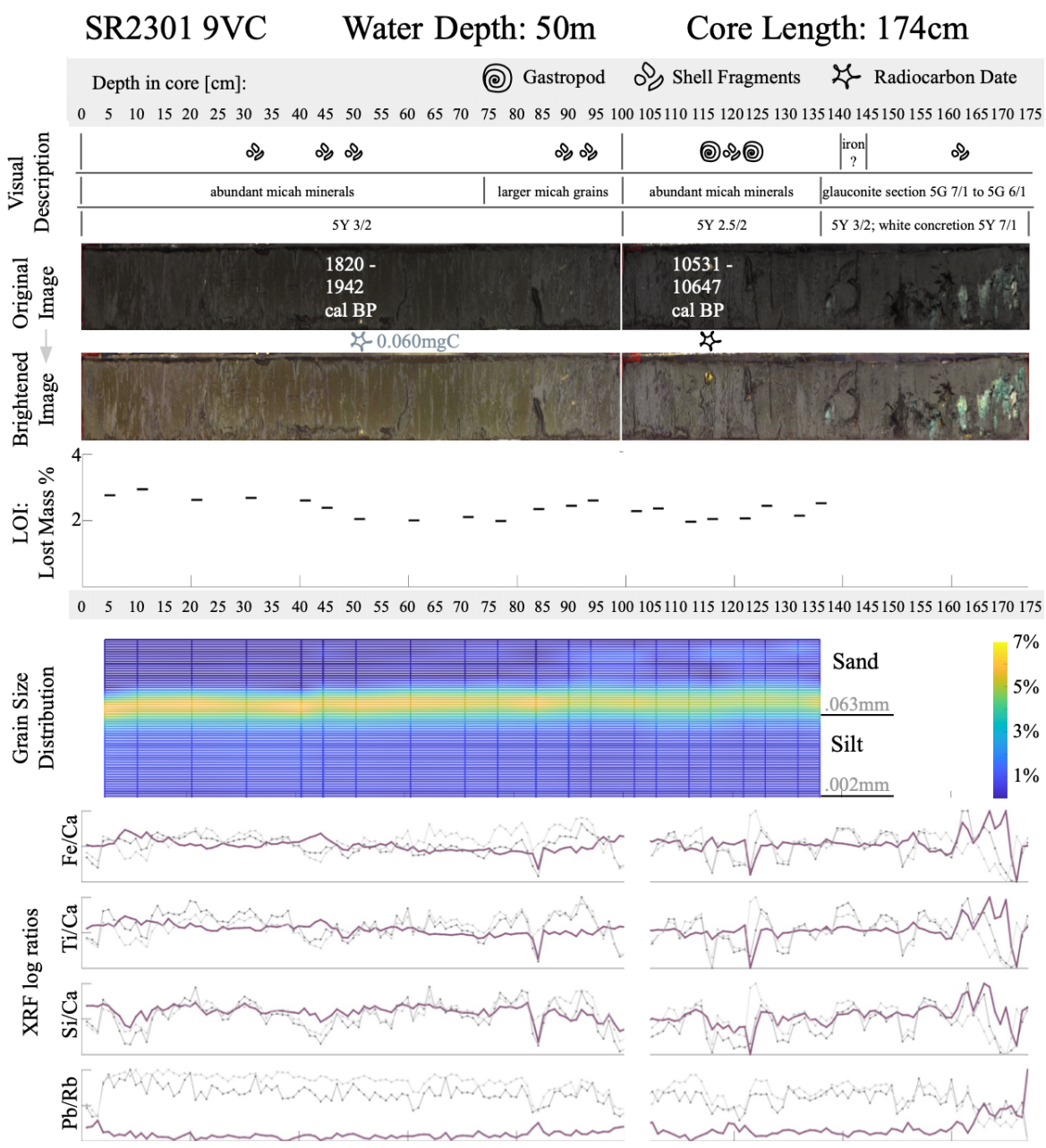

Figure 3.14. Description of core 9VC. The core was taken at 50m water depth and is 174 cm long. Depth in the core increases from left to right. The core was split into two sections: section 1 is 0-100 cm and section 2 is 100-174 cm. The visual description is shown along with colors from the Munsell color chart. The original image is shown above a 'brightened' image in which the image exposure, saturation, and sharpness were set to maximum. Radiocarbon-dated sample intervals are shown between the two images. Below the images are the loss on ignition and grain size results. Loss on ignition is displayed as the percent of mass loss for each sample. Grain size plots show the percentage of sample measured at each grain size for sample core depth. Solid lines denote measured grain size distributions, which are interpolated to shade the full plot range. At bottom are the Fe/Ca, Ti/Ca, Si/Ca, and Pb/Rb count ratios obtained from the XRF scan.

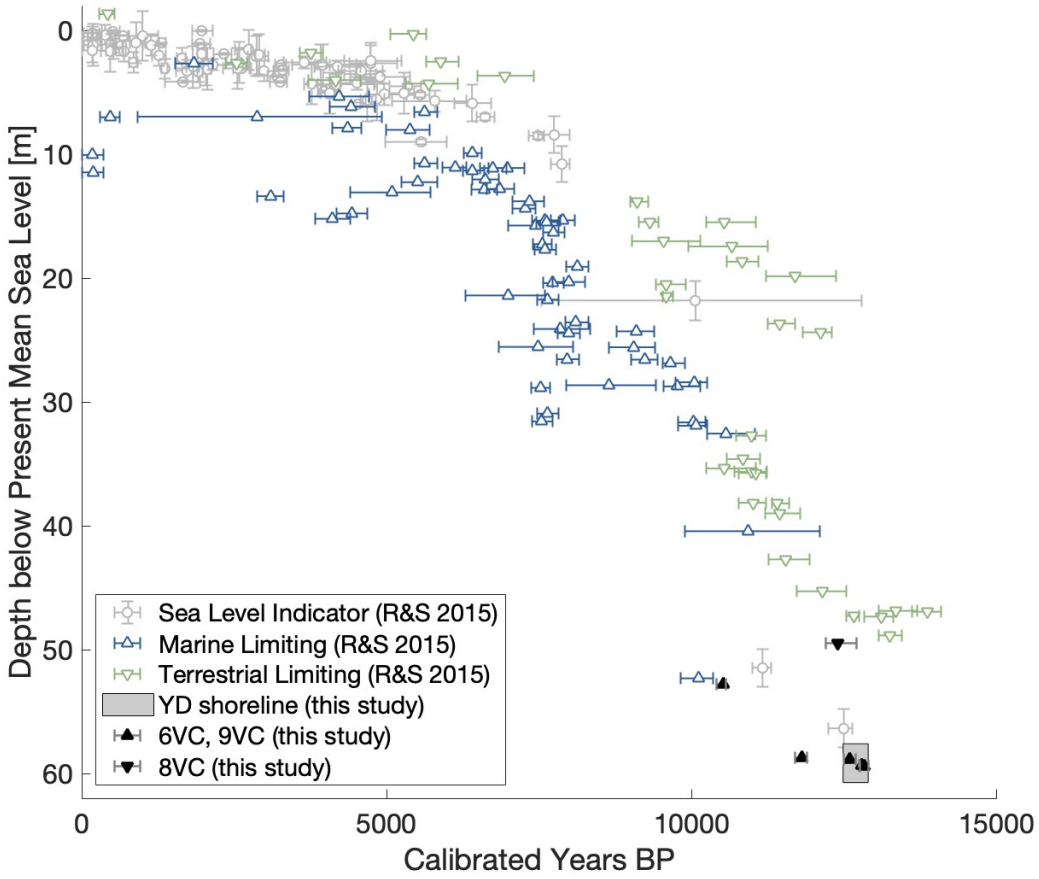

Figure 3.15. Mean sea level vs calibrated years before present using data points compiled by [Reynolds and Simms, 2015]. Error bar colors and marker shapes indicate whether the point is terrestrial limiting (upper bound for sea level, meaning this point was on land at this time), marine limiting (lower bound for sea level, meaning this point was underwater at this time), or a true sea level indicator. Many of the Reynolds and Simms 2015 Younger Dryas dates are from the Los Angeles Outer Harbor, Huntington Beach, and the Santa Monica Shelf. Cores dates from this study were added in black. The gray shaded square indicates the Younger Dryas estimate from our study, where depth is the range of Younger Dryas paleoshoreline angle depths and the date range is from core 6VC samples 6VC-6 and 6VC-10. We omitted dates that used $<$25 mgC. We consider the date from 8VC to be terrestrial limiting and dates from 6VC and 9VC to be marine limiting. The Younger Dryas shoreline is the closest to true depth. We added long term tectonic uplift at a rate of 0.08 mm/year to our depths to make them comparable to the Reynolds and Simms 2015 data, which used this rate in the San Diego region.

Core 6VC produces evidence of a wetland transforming to sandy beach just south of the deepest portion of the channel. Multiple acoustic layers on either side of the channel, appearing beneath the modern sediment cover, could potentially be indicative of wetlands or alternate channels. The sub-bottom profiles from the north deep channel reveal 3-4 acoustic units at seafloor depths greater than the picked Younger Dryas shoreline, while shallower portions of the channel contain just 2 units (fig. 3.11). The extra sediment layering increases our confidence that the Younger Dryas shoreline is in the location we designate. Tracing the shoreline picks on a map shows the Younger Dryas shore out about 3km seaward from its present location leaving about 1km of the continental shelf before a steep drop in the bathymmetry (fig. 3.10).

The two additional potential-shoreline picks, B and C, are covered in one acoustic unit in the two southern east-west profiles. Core 9VC indicates that they are covered entirely in Holocene sediment (see section 3.3.2), indicating that they may correspond to earlier sea level stands. It is possible that in the south of the river valley, erosion by waves was stronger, which could account for the lack of pre-inundation sediment cover and for the near-absence of the shoreline angles. However, it is also possible that some or all picks identified as shorelines B and C are not paleoshorelines at all, but are rather bending associated with the fault zone. The rocky features visible in the bathymetry and raised portions of the acoustic basement visible in the sub-bottom profiles may have also resulted from local tectonics and differential erosion of the bedrock. The same Holocene-only cover over picks B and C in the southern profiles covers an area north of a raised feature visible in the bathymetry, west of potentially-related raised features visible in the sub-bottom profiles, and east of the identified Younger Dryas paleoshoreline (fig. 3.11). While any sediment atop this region may have been washed away by waves during inundation, it it also possible that the bedrock was exposed during the Younger Dryas. Arid conditions and strong winds, for instance, could have blown away sediment leaving bare bedrock just onshore. High Ti/Fe and Si/Ca ratios, which have been used as proxies for aeolian dust flux and wind strength [**?**], are elevated in core 6VC between about 70-75 cm depth in the core. This occurs at the top of sandy beach-like sediments, just below an organic-rich sediment layer.

This could indicate high winds preceded, and were possibly associated with, this transition. High winds could have taken sediment from the subaerial zone in the south of the river valley, exposing the bedrock. More data could help us determine whether wind and aridity or erosion by high-energy waves during inundation led to the present holocene-only sediment cover conditions.

The transition from potential wetland to beach in core 6VC takes place early in the Younger Dryas, and the beach lasts for up to a few hundred years before sediments get gradually more silty, terrestrial, and organic, still during the Younger Dryas. This could be due to a change in weathering conditions, like high winds, or in sediment accumulation and transport paths. With only one core containing these sediments, the cause of the sediment transition is difficult to pinpoint with certainty. After slightly elevated terrestrial levels of sediment deposition, we observe an abrupt transition to Holocene sediments beginning by 11935-11737 cal BP. While these dates are earlier than the global Younger Dryas end date that is commonly put forth, this timing is in line with other evidence from the tropical pacific [Cheng et al., 2020].

Silt layers in core 8VC could be due to storms or inundation events where organic-rich silt was trapped behind the rock in sub-bottom line 4 (fig. 3.7). These sediments date to 11204-10888 cal BP, and a shallower part of the core dates to 12612-12015 cal BP, showing a date inversion. If the silt lens dates are correct, the lenses may have been storm sediments or inundation events, trapped behind the rock, that were covered during subsequent inundation or deposition events carrying older sediments. High Ti/Ca and Fe/Ca ratios indicate that the silt layers are from terrestrial origin, pointing toward storm runoff. Dating of the large and smaller silt lenses is could be uncertain however due to small dating sample mass. The Younger Dryas date obtained higher up in the core could mean that the silt lenses were deposited during the Younger Dryas or before. A subtle increase in Fe/Ca and Ti/Ca around 52cm depth in the core proceeded by elevated levels of Pb/Rb and Si/Ca may mark a transition to Holocene sediment with high winds as they could in core 6VC, but more dates would be needed to support that idea. If the silt lenses are indeed from the Younger Dryas, they are again more likely from storms than inundation events, as core 8VC was taken from higher ground than the Younger Dryas shore. Unless core

8VC is missing a significant portion of the surface, it looks from the seismic profiles like 8VC did not penetrate to the lowest acoustic unit, so older sediments that could help to complete the picture likely exist below the silt lenses.

Little relative sea level data from southern California exists [Reynolds and Simms, 2015], and data older than 10ky BP is scattered. A regional sea level curve could help delineate the local timing of the Younger Dryas. It is also important for understanding site-specific uplift and subsidence rates. We take measurements in a fault zone, so our data may not be appropriate for composing a general RSL curve, but it could tell us something about the tectonics in the area if there were an appropriate local RSL curve. Combining paleoshoreline depths with a regional sea level curve is a way to see how the ground moved since the creation of the paleoshoreline. The Younger Dryas shoreline we identified is deeper than most contemporary data points compiled by Reynolds and Simms 2015 [Reynolds and Simms, 2015], but many of those dates are from further north, namely Los Angeles Outer Harbor, Huntington Beach, and the Santa Monica Shelf, which may have experienced more uplift than the San Diego area (fig. 3.15). Due to the depth scatter among the older dates, more Younger Dryas data is needed to draw reliable conclusions about local tectonic activity.

3.5 Conclusion

The Younger Dryas was a time of stable sea level followed by rapid sea level rise, similar to predictions of present and near-future conditions. Understanding how the coast has responded to past sea level rise and climate changes can inform policy decisions and promote effective human adaptations as sea level rises again. This study has yielded new information to constrain local Younger Dryas conditions, timing, and sea level. The San Dieguito lagoon used to be a wide river valley with an active channel along the north edge that remains preserved to some extent. Just south of the deep channel, we see evidence of a wetland transforming to sandy beach early in the Younger Dryas. There the beach lasts for up to a few hundred years before sediments get

gradually more silty, terrestrial, and organic. After slightly elevated levels of terrestrial sediment deposition, we observe an abrupt transition to Holocene sediments beginning by 11935-11737 cal BP, timing that agrees with other data from the tropical pacific [Cheng et al., 2020].

The San Dieguito study area demonstrates preservation of material that can reveal local Younger Dryas climate conditions, so it is worth revisiting. Potentially pre-Holocene sediments appear preserved in the deep channel and on its margins. Pre-Holocene sediment is absent above the Younger Dryas shoreline in the south side of the river margin, which could point towards arid, windy conditions during the Younger Dryas or highly erosive wave action during inundation. Additional sediment coring in the valley could support models of sediment transport and landscape change during post-Younger Dryas sea level rise. The Holocene sediment layer thins above the largest Younger Dryas paleoshoreline angle identified in the south of the river valley, making the potentially pre-Holocene sediments accessible below. Thick sediments containing multiple acoustic units also exist west of the exposed rock that borders the south of the channel. More survey lines in this area could help relate this sediment to the rest of the valley.

The southern California coast contains numerous channels with varied morphology. While the San Dieguito valley is worth revisiting, results here must be combined with other locations for a holistic picture of the Younger Dryas in southern California. More studies elsewhere on the shelf are needed to expand our baseline knowledge of the local environment throughout the late Pleistocene and Holocene when humans may have entered and when the global climate underwent drastic change that we have yet to fully characterize.

3.6 Acknowledgements

The cruise on which the SBP29 data and vibracores were collected was funded by UC Ship Funds. We thank Bruce Applegate and the captain and crew of the *RV Sally Ride*, as well as the resident technicians and volunteers who make the trip possible and worthwhile. Special thanks to Jillian Maloney for lending us her vibracorer and expertise while at sea. Thanks also to

Katrina Cantu and Alex Hangsterfer for their training and instruction on vibracore analysis.

Data used in this study were acquired, processed, archived, and distributed by the Seafloor Mapping Lab of California State University Monterey Bay.

Chapter 3, in part is currently being prepared for submission for publication of the material. Morris, Margaret; Rivera-Collazo, Isabel; Hildebrand, John. The dissertation author was the primary investigator and author of this material.

Bibliography

[Abawi, 2017] Abawi, A. T. (2017). Finite Element Modeling of Scattering from Underwater Proud and Buried Military Munitions. Technical report, Strategic Environmental Research and Development Program, Alexandria, VA.

[Abawi and Krysl, 2017] Abawi, A. T. and Krysl, P. (2017). Coupled finite element/boundary element formulation for scattering from axially-symmetric objects in three dimensions. *The Journal of the Acoustical Society of America*, 142(6):3637–3648.

[Aliyu et al., 2017] Aliyu, M. M., Murphy, W., Lawrence, J. A., and Collier, R. (2017). Engineering geological characterization of flints. *Quarterly Journal of Engineering Geology and Hydrogeology*, 50(2):133–147.

[Astrup et al., 2019] Astrup, P. M., Skriver, C., Benjamin, J., Stankiewicz, F., Ward, I., McCarthy, J., Ross, P., Baggaley, P., Ulm, S., and Bailey, G. (2019). Underwater Shell Middens: Excavation and Remote Sensing of a Submerged Mesolithic site at Hjarnø, Denmark. *The Journal of Island and Coastal Archaeology*, pages 1–20.

[Au and Moore, 1984] Au, W. W. and Moore, P. W. (1984). Receiving beam patterns and directivity indices of the Atlanti bottlenose dolphin Tursiops truncatus. *Journal of the Acoustical Society of America*, 75(1):255–262.

[Bailey and Flemming, 2008] Bailey, G. N. and Flemming, N. C. (2008). Archaeology of the continental shelf: Marine resources, submerged landscapes and underwater archaeology. *Quaternary Science Reviews*, 27:2153–2165.

[Bailey and King, 2011] Bailey, G. N. and King, G. C. (2011). Dynamic landscapes and human dispersal patterns: Tectonics, coastlines, and the reconstruction of human habitats. *Quaternary Science Reviews*, 30(11-12):1533–1553.

[Beller et al., 2014] Beller, E., Baumgarten, S., Grossinger, R., Longcore, T., Stein, E., Dark, S., and Dusterhoff, S. (2014). Northern San Diego County Lagoons Historical Ecology Investigation. *San Francisco Estuary Institute Publication*.

[Benjamin, 2010] Benjamin, J. (2010). Submerged prehistoric landscapes and underwater site discovery: Reevaluating the 'Danish Model' for international practice. *Journal of Island and Coastal Archaeology*, 5(2):253–270.

[Bezanson et al., 2017] Bezanson, J., Edelman, A., Karpinski, S., and Shah, V. B. (2017). Julia: A fresh approach to numerical computing. *SIAM Review*, 59(1):65–98.

[Blake and Cross, 2008] Blake, E. C. and Cross, I. (2008). Flint Tools as Portable Sound-Producing Objects in the Upper Palaeolithic Context: An Experimental Study. In Cunningham, P., Heeb, J., and Paardekooper, R., editors, *Experiencing Archaeology by Experiment*, pages 1–19. Oxbow Books, Oxford.

[Blevins, 2016] Blevins, R. D. (2016). *Formulas for Dynamics, Acoustics, and Vibration*. John Wiley & Sons, Ltd.

[Braje et al., 2019a] Braje, T. J., Erlandson, J. M., Rick, T. C., Davis, L., Dillehay, T., Fedje, D. W., Froese, D., Gusick, A., Mackie, Q., McLaren, D., Pitblado, B., Raff, J., Reeder-Myers, L., and Waters, M. R. (2019a). Fladmark + 40: What Have We Learned about a Potential Pacific Coast Peopling of the Americas? *American Antiquity*, 85(1):1–21.

[Braje et al., 2019b] Braje, T. J., Maloney, J. M., Gusick, A. E., Erlandson, J. M., Nyers, A., Davis, L., Gill, K. M., Reeder-Myers, L., and Ball, D. (2019b). Working from the known to the unknown: Linking the subaerial archaeology and the submerged landscapes of santarosae island, Alta California, USA. *Open Quaternary*, 5(1):1–15.

[Centre et al., 2020] Centre, D. G. f. M. A., Fisheries, and the Joint Research (2020). *The EU Blue Economy Report 2020*. Publications Office of the European Union, Luxembourg.

[Cheng et al., 2020] Cheng, H., Zhang, H., Spötl, C., Baker, J., Sinha, A., Li, H., Bartolomé, M., Moreno, A., Kathayat, G., Zhao, J., Dong, X., Li, Y., Ning, Y., Jia, X., Zong, B., Brahim, Y. A., Pérez-Mejiás, C., Cai, Y., Novello, V. F., Cruz, F. W., Severinghaus, J. P., An, Z., and Edwards, R. L. (2020). Timing and structure of the Younger Dryas event and its underlying climate dynamics. *Proceedings of the National Academy of Sciences of the United States of America*, 117(38):23408–23417.

[Cranford and Krysl, 2015] Cranford, T. W. and Krysl, P. (2015). Fin whale sound reception mechanisms: Skull vibration enables low-frequency hearing. *PLoS ONE*, 10(1):1–17.

[Cranford et al., 2010] Cranford, T. W., Krysl, P., and Amundin, M. (2010). A new acoustic portal into the odontocete ear and vibrational analysis of the tympanoperiotic complex. *PLoS ONE*, 5(8).

[Cranford et al., 2013] Cranford, T. W., Trijoulet, V., Smith, C. R., and Krysl, P. (2013). Validation of a vibroacoustic finite element model using bottlenose dolphin simulations: The dolphin biosonar beam is focused in stages.

[Erlandson, 2001] Erlandson, J. M. (2001). The Archaeology of aquatic adaptations: Paradigms for a new millennium. *Journal of Archaeological Research*, 9(4):287–350.

[Erlandson et al., 1996] Erlandson, J. M., Kennett, D. J., Ingram, B. L., Guthrie, D. A., Morris, D. P., Tveskov, M. A., West, G. J., and Walker, P. L. (1996). An archaeological and

paleontological chronology for Daisy Cave (CA-SMI-261), San Miguel Island, California. *Radiocarbon*, 38(2):355–373.

[Erlandson et al., 2011] Erlandson, J. M., Rick, T. C., Braje, T. J., Casperson, M., Culleton, B., Fulfrost, B., Garcia, T., Guthrie, D. A., Jew, N., Kennett, D. J., Moss, M. L., Reeder, L., Skinner, C., Watts, J., and Willis, L. (2011). Paleoindian Seafaring, Maritime Technology, and Coastal Foraging on California's Channel Islands. *Science*, 331(March):1181–1186.

[Fairbanks, 1989] Fairbanks, R. G. (1989). A 17,000-year glacio-eustatic sea level record: influence of glacial melting rates on the Younger Dryas event and deep-ocean circulation. *Nature*, 342(6250):637–642.

[Flemming, 2020] Flemming, N. C. (2020). Global experience in locating submerged prehistoric sites and their relevance to research on the american continental shelves. *Journal of Island and Coastal Archaeology*, 0(0):1–24.

[Flemming et al., 2014] Flemming, N. C., Çağatay, M. N., Chiocci, F. L., Galanidou, N., Lericolais, G., Jöns, H., Missiaen, T., Moore, F., Rosentau, A., Sakellariou, D., Skar, B., Stevenson, A., and Weerts, H. (2014). *Land Beneath the Waves Submerged landscapes and sea level change*. Position Paper 21 of the European Marine Board, Ostend, Belgium.

[Flemming et al., 2017] Flemming, N. C., Harff, J., Moura, D., Burgess, A., and Bailey, G. N. (2017). Introduction : Prehistoric Remains on the Continental Shelf — Why do Sites and Landscapes Survive Inundation? In Flemming, N. C., Harff, J., Moura, D., Burgess, A., and Bailey, G. N., editors, *Submerged Landscapes ofthe European Continental Shelf: Quaternary Paleoenvironments*, chapter Chapter 1, pages 1–10. John Wiley & Sons Ltd., 1 edition.

[Grøn et al., 2018a] Grøn, O., Boldreel, L. O., Hermand, J. P., Rasmussen, H., Dell'anno, A., Cvikel, D., Galili, E., Madsen, B., and Normark, E. (2018a). Status for the development of acoustic mapping of submerged stone age sites. *2017 IEEE/OES Acoustics in Underwater Geosciences Symposium, RIO Acoustics 2017*, 2018-Janua:1–5.

[Grøn et al., 2018b] Grøn, O., Boldreel, L. O., Hermand, J. P., Rasmussen, H., Dell'anno, A., Cvikel, D., Galili, E., Madsen, B., and Nørmark, E. (2018b). Detecting human-knapped flint with marine high-resolution reflection seismics: A preliminary study of new possibilities for subsea mapping of submerged stone age sites. *Underwater Technology*, 35(2):35–49.

[Grøn et al., 2021] Grøn, O., Boldreel, L. O., Smith, M. F., Joy, S., Boumda, R. T., and Mäder, A. (2021). Acoustic Mapping of Submerged Stone Age Sites — A HALD Approach. *MDPI Remote Sensing*, 13(3):445.

[Gusick et al., 2021] Gusick, A. E., Braje, T. J., Erlandson, J. M., Maloney, J., and Ball, D. (2021). Above and Below the Waves:. *The Archaeology of Island Colonization*, pages 105–131.

[Gusick and Davis, 2019] Gusick, A. E. and Davis, L. G. (2019). Exploring Baja California ' s Submerged Landscapes. *Journal of California and Great Basin Anthropology*, 30(1):35–49.

[Gusick et al., 2022] Gusick, A. E., Maloney, J., Braje, T. J., Retallack, G. J., Johnson, L., Klotsko, S., Ainis, A., and Erlandson, J. M. (2022). Soils and terrestrial sediments on the seafloor: Refining archaeological paleoshoreline estimates and paleoenvironmental reconstruction off the California coast. *Frontiers in Earth Science*, 10(September):1–18.

[Hermand et al., 2011] Hermand, J.-P., Grøn, O., Asch, M., and Ren, Q. (2011). Modelling flint acoustics for detection of submerged Stone Age sites. *OCEANS 2011 MTS/IEEE KONA*, pages 1–9.

[Hermand and Tayong, 2013] Hermand, J.-P. and Tayong, R. (2013). Geoacoustic characterization of Stone Age cultural layers: Preliminary FE modelling. *IEEE*.

[Hildebrand, 2009] Hildebrand, J. A. (2009). Anthropogenic and natural sources of ambient noise in the ocean. *Marine Ecology Progress Series*, 395:5–20.

[Hildebrand and York, 2022] Hildebrand, J. A. and York, A. L. (2022). Modeling and monitoring submerged prehistoric sites during offshore sand dredging and implications for the study of Early Holocene Coastal Occupation of Southern California. *Geoarchaeology*, 37(5):768–782.

[Joy, 2020] Joy, S. (2020). Coastally-adapted: A developing model for coastal Paleoindian sites on the North American eastern continental shelf. *Journal of Island and Coastal Archaeology*, 16(1):150–169.

[Klein and Carmichael, 2021] Klein, C. and Carmichael, R. S. (2021). Rock.

[Knudsen and Konishi, 1979] Knudsen, E. I. and Konishi, M. (1979). Mechanisms of sound localization in the barn owl (Tyto alba). *Journal of Comparative Physiology A*, 133(1):13–21.

[Krysl, 2021] Krysl, P. (2021). FinEtools.jl: Finite Element Tools in Julia.

[Krysl, 2023] Krysl, P. (2023). FinEtools.jl: Finite Element Tools in Julia - Github Repository.

[Lambeck et al., 2014] Lambeck, K., Rouby, H., Purcell, A., Sun, Y., and Sambridge, M. (2014). Sea level and global ice volumes from the Last Glacial Maximum to the Holocene. *Proceedings of the National Academy of Sciences of the United States of America*, 111(43):15296–15303.

[Lancaster et al., 2015] Lancaster, W. C., Ary, W. J., Krysl, P., and Cranford, T. W. (2015). Precocial development within the tympanoperiotic complex in cetaceans. *Marine Mammal Science*, 31(1):369–375.

[Laws et al., 2020] Laws, A. W., Maloney, J. M., Klotsko, S., Gusick, A. E., Braje, T. J., and Ball, D. (2020). Submerged paleoshoreline mapping using high-resolution Chirp sub-bottom data, Northern Channel Islands platform, California, USA. *Quaternary Research (United States)*, 93(1):1–22.

[Lees et al., 1996] Lees, S., Hanson, D. B., and Page, E. A. (1996). Some acoustical properties of the otic bones of a fin whale. *The Journal of the Acoustical Society of America*, 99(4):2421–2427.

[Lógó and Vásárhelyi, 2019] Lógó, B. A. and Vásárhelyi, B. (2019). Estimation of the poisson's rate of the intact rock in the function of the rigidity. *Periodica Polytechnica Civil Engineering*, 63(4):1030–1037.

[McCarthy et al., 2019] McCarthy, J. K., Benjamin, J., Winton, T., and van Duivenvoorde, W. (2019). *3D Recording and Interpretation for Maritime Archaeology*, volume 31. Springer International Publishing, 1 edition.

[McLaren et al., 2020] McLaren, D., Fedje, D., Mackie, Q., Davis, L. G., Erlandson, J., Gauvreau, A., and Vogelaar, C. (2020). Late Pleistocene Archaeological Discovery Models on the Pacific Coast of North America. *PaleoAmerica*, 6(1):43–63.

[Mead and Fordyce, 2009] Mead, J. G. and Fordyce, R. E. (2009). The therian skull : a lexicon with emphasis on the odontocetes. *Smithsonian Contributions to Zoology*, 627:1–249.

[Plets et al., 2013] Plets, R., Dix, J., and Bates, R. (2013). Marine Geophysics Data Acquisition, Processing and Interpretation. Guidance notes. *English Heritage*, pages 1–92.

[Quiralte and Dell, 2013] Quiralte, B. and Dell, R. (2013). Enhanced Sonar Sensitivity Incorporating the Structural Aspects of Whale Ears. *Engineering*, Master's D:110.

[Reeder et al., 2011] Reeder, L. A., Erlandson, J. M., and Rick, T. C. (2011). Younger Dryas environments and human adaptations on the West Coast of the United States and Baja California. *Quaternary International*, 242(2):463–478.

[Reeder-Myers et al., 2015] Reeder-Myers, L., Erlandson, J. M., Muhs, D. R., and Rick, T. C. (2015). Sea level, paleogeography, and archeology on California's Northern Channel Islands. *Quaternary Research (United States)*, 83(2):263–272.

[Reynolds and Simms, 2015] Reynolds, L. C. and Simms, A. R. (2015). Late Quaternary relative sea level in Southern California and Monterey Bay. *Quaternary Science Reviews*, 126:57–66.

[Rogers, 1966] Rogers, M. J. M. J. (1966). *Ancient hunters of the Far West*. Copley book. Union-Tribune Pub. Co., San Diego, Calif, special ed edition.

[Römer, 2020] Römer, H. (2020). Directional hearing in insects: biophysical, physiological and ecological challenges. *Journal of Experimental Biology*, 223(14).

[Ryabov, 2023] Ryabov, V. A. (2023). The Role of Asymmetry of the Left and Right External Ear of Bottlenose Dolphin (Tursiops truncatus) in the Spatial Localization of Sound. *Acoustical Physics*, 69(1):119–131.

[Schillberg et al., 2020] Schillberg, P., Brill, S., Nikolay, P., Ferger, R., Gerhard, M., Führ, H., and Wagner, H. (2020). Sound localization in barn owls studied with manipulated head-related transfer functions: beyond broadband interaural time and level differences. *Journal of Comparative Physiology A: Neuroethology, Sensory, Neural, and Behavioral Physiology*, 206(4):477–498.

[Sedlin, 1965] Sedlin, E. D. (1965). A rheologic model for cortical bone. A study of the physical properties of human femoral samples. *Acta orthopaedica Scandinavica. Supplementum*, 6470.

[(SFEI), 2014] (SFEI), S. F. E. I. (2014). Northern San Diego County Lagoons Historical Ecology GIS data.

[Sivapuram and Krysl, 2019] Sivapuram, R. and Krysl, P. (2019). On the energy-sampling stabilization of Nodally Integrated Continuum Elements for dynamic analyses. *Finite Elements in Analysis and Design*, 167:1–53.

[Southall et al., 2019] Southall, E. B. L., Finneran, J. J., Reichmuth, C., Nachtigall, P. E., Ketten, D. R., Bowles, A. E., Ellison, W. T., Nowacek, D. P., and Tyack, P. L. (2019). Marine mammal noise exposure criteria: Updated scientific recommendations for residual hearing effects. *Aquatic Mammals*, 45(2):125–232.

[Sturt et al., 2018] Sturt, F., Flemming, N. C., Carabias, D., Jöns, H., and Adams, J. (2018). The next frontiers in research on submerged prehistoric sites and landscapes on the continental shelf. *Proceedings of the Geologists' Association*, 129(5):654–683.

[Stuvier and A., 1977] Stuvier, M. and A., P. H. (1977). Reporting of 14C Data. *Radiocarbon*, 19(3):355–363.

[Tsukrov et al., 2009] Tsukrov, I., DeCew, J. C., Baldwin, K., Campbell-Malone, R., and Moore, M. J. (2009). Mechanics of the right whale mandible: Full scale testing and finite element analysis. *Journal of Experimental Marine Biology and Ecology*, 374(2):93–103.

[Tubelli et al., 2014] Tubelli, A. A., Zosuls, A., Ketten, D. R., and Mountain, D. C. (2014). Elastic modulus of cetacean auditory ossicles. *Anatomical Record*, 297(5):892–900.

[Tubelli et al., 2018] Tubelli, A. A., Zosuls, A., Ketten, D. R., and Mountain, D. C. (2018). A model and experimental approach to the middle ear transfer function related to hearing in the humpback whale (Megaptera novaeangliae) . *The Journal of the Acoustical Society of America*, 144(2):525–535.

[UNESCO, 2001] UNESCO (2001). Official Texts of the United Nations Educational, Scientific and Cultural Organization.

[Walton et al., 2020] Walton, M. A., Papesh, A. G., Johnson, S. Y., Conrad, J. E., and Brothers, D. S. (2020). Quaternary faults offshore of California: data release. Technical report, U.S. Geological Survey, Pacific Coastal and Marine Science Center, Santa Cruz, CA.

[Wang et al., 2021] Wang, F., Ding, J., Tao, C., and Lin, X. (2021). Sound velocity characteristics of unconsolidated sediment based on high-resolution sub-bottom profiles in Jinzhou Bay, Bohai Sea of China. *Continental Shelf Research*, 217(February).

[Warren, 1967] Warren, C. N. (1967). The San Dieguito Complex : A Review and Hypothesis. *American Antiquity*, 32(2):168–185.

[Warren and Ore, 2011] Warren, C. N. and Ore, H. T. (2011). The Age of the San Dieguito Artifact Assemblage at the C. W. Harris Site. *Journal of California and Great Basin Anthropology*, 31(1):81–97.

[Watts et al., 2011] Watts, J., Fulfrost, B., and Erlandson, J. (2011). Searching for Santarosae: Surveying Submerged Landscapes for Evidence of Paleocoastal Habitation Off California's Northern Channel Islands Jack. In Ford, B., editor, *The Archaeology of Maritime Landscapes, When the Land Meets the Sea*, volume 2, chapter 1, pages 11–26. Springer Science+Business Media, LLC.

[Westerdahl, 2011] Westerdahl, C. (2011). *When the Land Meets the Sea: Archaeology of maritime landscapes*.

[Westley et al., 2011] Westley, K., Quinn, R., Forsythe, W., Plets, R., Bell, T., Benetti, S., McGrath, F., and Robinson, R. (2011). Mapping Submerged Landscapes Using Multibeam Bathymetric Data: A case study from the north coast of Ireland. *International Journal of Nautical Archaeology*, 40(1):99–112.

[Zhang and Gan, 2011] Zhang, X. and Gan, R. Z. (2011). Experimental measurement and modeling analysis on mechanical properties of incudostapedial joint. *Biomechanics and Modeling in Mechanobiology*, 10(5):713–726.